

---

# National Laser Users' Facility and External Users' Programs

Under the facility governance plan that was implemented in FY08 to formalize the scheduling of the Omega Laser Facility as an National Nuclear Security Administration (NNSA) User Facility, Omega Facility shots are allocated by campaign. The majority (67.6%) of the FY12 target shots were allocated to the National Ignition Campaign (NIC) conducted by integrated teams from the national laboratories and LLE and to the high-energy-density campaigns conducted by teams led by scientists from the national laboratories.

Nearly 29% of the facility shots in FY12 were allocated to basic science experiments. Half of these were dedicated to university basic science under the National Laser Users' Facility (NLUF) Program, and the remaining shots were allotted to the Laboratory Basic Science (LBS) Program, comprising peer-reviewed basic science experiments conducted by the national laboratories and by LLE including the Fusion Science Center (FSC).

The Omega Facility is also being used for several campaigns by teams from the Commissariat à l'Énergie Atomique (CEA) of France and the Atomic Weapons Establishment (AWE) of the United Kingdom. These programs are conducted at the facility on the basis of special agreements put in place by DOE/NNSA and participating institutions.

The facility users during this year included 11 collaborative teams participating in the NLUF Program; 12 teams led by Lawrence Livermore National Laboratory (LLNL) and LLE scientists participating in the LBS Program; many collaborative teams from the national laboratories conducting experiments for the NIC; investigators from LLNL and Los Alamos National Laboratory (LANL) conducting experiments for high-energy-density-physics programs; and scientists and engineers from CEA, AWE, and the Center for Radiative Shock Hydrodynamics (CRASH) of the University of Michigan.

In this section, we briefly review all the external user activity on OMEGA during FY12.

## FY12 NLUF Program

In FY12, the Department of Energy (DOE) issued a solicitation for NLUF grants for the period FY13–FY14. A record of 23 proposals were submitted to DOE for the NLUF FY13–FY14 program. An independent DOE Technical Evaluation Panel reviewed the proposals on 11 July 2012 and recommended that 11 proposals receive DOE funding and 28 days of shot time on OMEGA in each of FY13 and FY14. Table 132.VII lists the successful NLUF proposals for FY13–FY14.

FY12 was the second of a two-year period of performance for the NLUF projects approved for the FY11–FY12 funding and OMEGA shots. Eleven NLUF projects were allotted Omega Laser Facility shot time and conducted a total of 277 target shots at the facility. This work is summarized in this section.

### *Systematic Study of Fast-Electron Transport in Imploded Plasmas*

Principal Investigators: F. N. Beg (University of California, San Diego) and M. S. Wei (General Atomics)

Co-investigators: R. B. Stephens (General Atomics);

H. Sawada, C. McGuffey, and B. Qiao (UCSD); A. A.

Solodov, W. Theobald, C. Stoeckl, J. A. Delettrez, and

R. Betti (LLE); M. H. Key, P. Patel, and H. McLean (LLNL); and T. Yabuuchi and H. Habara (Osaka University)

Lead Graduate Student: L. C. Jarrott (UCSD)

Understanding fast-electron generation inside the cone and its subsequent transport into hot dense plasmas is crucial to the success of the cone-guided fast-ignition (FI) scheme of inertial confinement fusion. The goal of the University of California, San Diego (UCSD) NLUF project is to investigate the coupling efficiency and spatial energy deposition of fast electrons into an imploded CH/CD shell attached to a re-entrant gold cone target in joint OMEGA and OMEGA EP experiments. The Au cone has a 34° opening angle, 10- $\mu\text{m}$  inner tip diameter, 15- $\mu\text{m}$  cone-tip thickness, with 44- $\mu\text{m}$  offset distance from the tip to the shell center, while the CH/CD shell has an 870- $\mu\text{m}$  outer

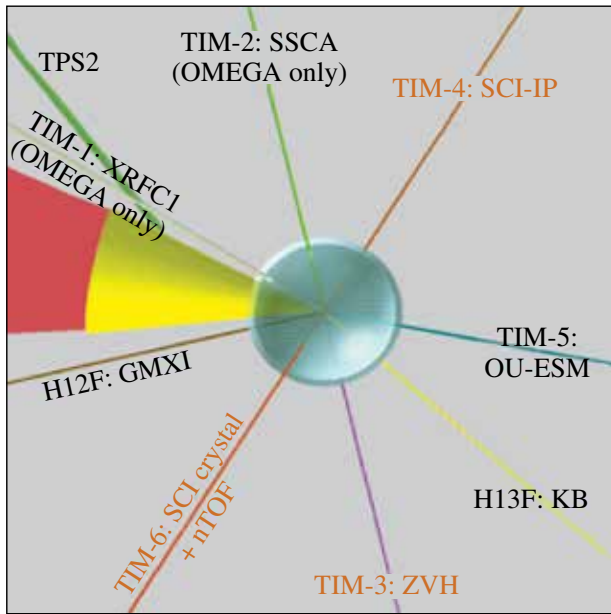
Table 132.VII: NLUF proposals approved for shots at the Omega Laser Facility for FY13–FY14.

Principal Investigator	Institution	Project Title
F. N. Beg	University of California, San Diego	Systematic Study of Fast-Electron Energy Deposition in Imploded Plasmas with Enhanced OMEGA EP Laser Contrast and Intensity
R. P. Drake	University of Michigan	Experimental Astrophysics on the OMEGA Laser
T. Duffy	Princeton University	Dynamic Compression of Earth and Planetary Materials Using OMEGA
W. Fox	University of New Hampshire	Dynamics and Instabilities of Magnetic Reconnection Current Sheets in High-Energy-Density Plasmas
P. Hartigan	Rice University	Astrophysical Dynamics in the Laboratory: Mach Stems and Magnetized Shocks
R. Jeanloz	University of California, Berkeley	Journey to the Center of Jupiter, Recreating Jupiter's Core on OMEGA
H. Ji	Princeton University	Study of Particle Acceleration and Fine-Scale Structures of Collisionless Magnetic Reconnection Driven by High-Energy Petawatt Lasers
B. Qiao	University of California, San Diego	Dynamics of High-Energy Proton Beam Focusing and Transition into Solid Targets of Different Materials
R. D. Petrasso	Massachusetts Institute of Technology	Studies of Laboratory Astrophysics, Inertial Confinement Fusion, and High-Energy-Density Physics with Nuclear Diagnostics
A. Spitkovsky	Princeton University	Generation of Collisionless Shocks in Laser-Produced Plasmas
R. B. Stephens	General Atomics	Investigation of the Dependence of Fast-Electron Generation and Transport on Laser Pulse Length and Plasma Materials

diameter consisting of a 15- $\mu\text{m}$ -thick outer CH ablator and a 23- $\mu\text{m}$ -thick inner CD layer. A Cu dopant (at  $\sim 1\%$  atomic number density of CD) is added to the CD layer of the shell, which allows one to characterize the fast electrons' transport via their induced Cu K-shell fluorescence radiation. The CH ablator prevents direct heating of the CD layer by the OMEGA driver beam and also reduces the neutron background from the corona plasmas. In this experiment, 54 (with a total energy of  $\sim 18$  kJ) of the 60 OMEGA beams with a low-adiabat pulse shape [LA241701P with smoothing by spectral dispersion (SSD) off] were used to compress the shell. The 10-ps OMEGA EP backlighter beam (BL2) was tightly focused at the inner cone tip with various time delays relative to the OMEGA driver. The primary diagnostics were a monochromatic spherical crystal imager (SCI) (centered at 8048 eV with 6-eV bandwidth) to image the Cu  $K_{\alpha}$  emission and a zinc Von Hamos (ZVH) x-ray spectrometer tuned to measure the Cu K-shell and ionic line emission spectrum. Several other diagnostics including broadband x-ray imaging diagnostics such as pinhole cameras and Kirkpatrick–Baez (KB) microscopes, neutron time-of-flight detectors, and a multichannel magnetic electron spectrometer

were also employed. Figure 132.47 shows the target and diagnostic setup for the experiment.

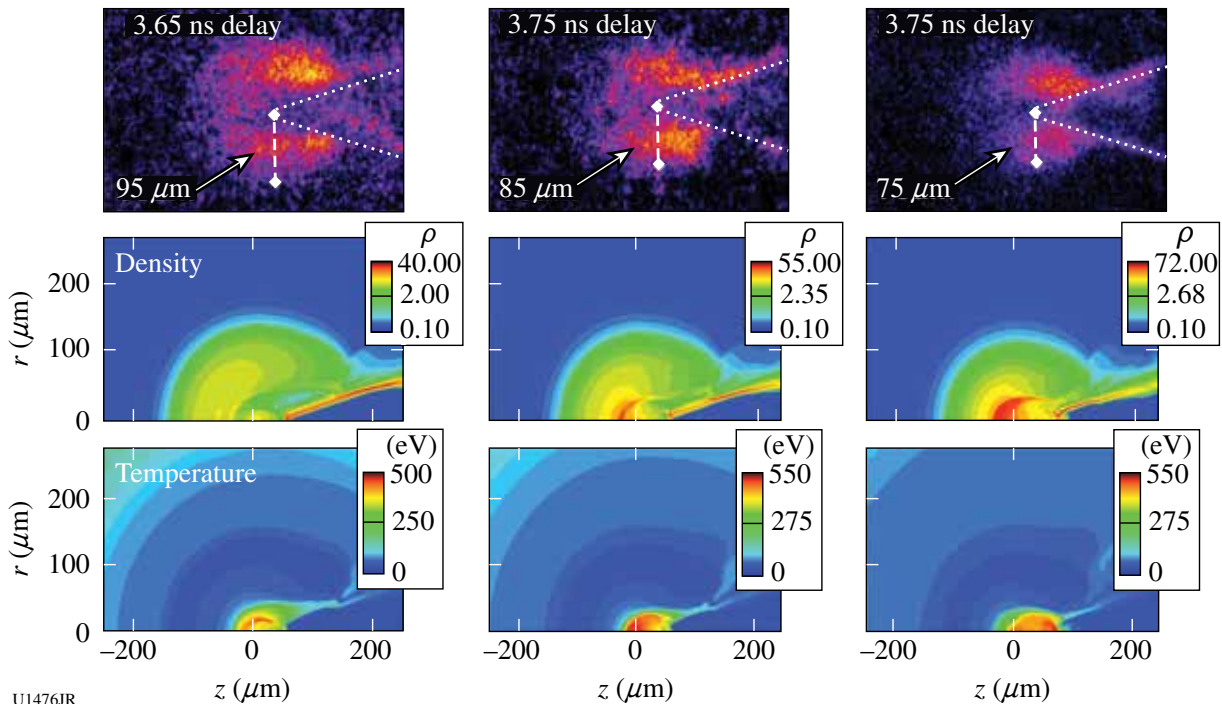
In this second-year (FY12) NLUF experiment, with the improvement made to the SCI diagnostic that was newly implemented on the OMEGA chamber in FY11 for the first-year NLUF experiment, we have obtained for the first time clear images of fast electrons' spatial energy deposition in the imploded plasmas. Figure 132.48 depicts the background-subtracted SCI images showing that the OMEGA EP beam produced fast-electron-induced Cu  $K_{\alpha}$  emission. The images show the imploded shell's center region from three joint shots with the OMEGA EP beam at  $\sim 500$ -J energy injected at three different time delays (i.e., 3.65 ns, 3.75 ns, and 3.85 ns) relative to the OMEGA driver. These SCI images clearly show that fast electrons penetrated through the cone (wall and tip) into the compressed shell, producing strong Cu  $K_{\alpha}$  emission from the region of the imploded high-density plasmas. The observed decreasing fluorescence emission spot size in the SCI images with increasing OMEGA EP time delay is consistent with the simulated density profiles of the imploded shell at the



U1475JR

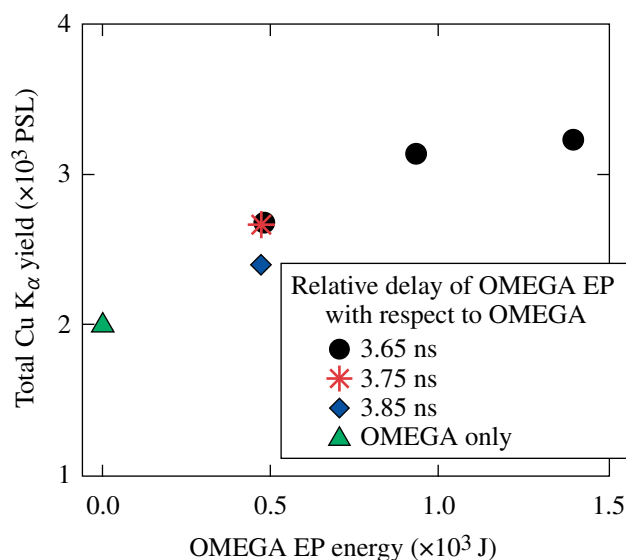
Figure 132.47  
VisRad view of the cone-in-shell target and diagnostics layout. Primary diagnostics for this experiment were the SCI and ZVH for Cu K-shell measurements, OU-ESM (multichannel magnetic spectrometer) for electron spectra, and nTOF (LaCave) for neutron measurement.

corresponding implosion time in the 2-D radiation–hydrodynamic modeling results (also shown in Fig. 132.48) using the *DRACO* code. It should be pointed out that the peak emission from the dense shell outside the side cone wall is  $\sim 100 \mu\text{m}$  farther away from the cone tip, which can be caused by the pre-plasma filling of the cone as a result of the intrinsic 3-ns-long prepulse with an energy of  $\sim 20 \text{ mJ}$  prior to the main pulse. It was also observed that the Cu  $K_{\alpha}$  emission was reduced in the hot region of the core in front of the cone tip, which can be explained by the reduced collection efficiency of the SCI due to the shifting and broadening of the Cu  $K_{\alpha}$  spectral line at plasma temperatures increasing above the order of 150 eV. The ZVH spectrometer provided spatially integrated Cu  $K_{\alpha}$ -yield measurements. As seen in Fig. 132.49, the total Cu  $K_{\alpha}$  yield (due to both OMEGA EP-produced MeV fast electrons and OMEGA driver-produced superthermal electrons with an energy of 20 to 30 keV) increased significantly (up to 60%) in the joint shots compared to the OMEGA-only implosion shots as a result of fast electrons propagating into the high-density plasma. Fast-electron energy coupling to the compressed core was found to increase with the OMEGA EP beam energy injected into the cone up to the time the cone tip broke out by the implosion-driven shocks. It is worth noting that at the latest delay, 3.85 ns, the yield decreased because the cone filled



U1476JR

Figure 132.48  
(Top) Cu  $K_{\alpha}$  images show the emission from the vicinity of the cone tip at various delays with the OMEGA EP beam energy at  $\sim 500 \text{ J}$ . The dotted lines are added to visualize the cone position, and the dashed lines show the estimated emission spot radius. The middle and bottom plots are the calculated mass density (in units of  $\text{g}/\text{cm}^3$ ) and temperature (eV) maps from the *DRACO* simulations above.



U1477JR

Figure 132.49

Total Cu K<sub>α</sub> yield from the joint shots and OMEGA-only shots showing increasing yield with increasing OMEGA EP energy. Also note the significant reduction in Cu K<sub>α</sub> yield at 3.85 ns for the OMEGA EP delay corresponding to after the cone-tip breakout by the implosion.

with plasma after the implosion-driven shock destroyed the cone tip—consistent with the *DRACO*-simulation prediction.

In summary, the FY12 UCSD-led NLUF fast-electron transport experiment with cone-in-shell (with Cu doping) targets has made the first direct measurements of the spatial energy deposition of fast electrons into an imploded high-density plasma core in the cone-guided FI configuration. The Cu fluorescence images show a clear signature of fast electrons heating the high-density plasma core and an increase in fast-electron energy coupling with OMEGA EP beam energy. Further work is in progress to combine these measurements with simulations to deconvolve the quantitative spatial information of fast-electron distribution, core plasma density, and temperature.

### Experimental Astrophysics on the OMEGA Laser

Principal Investigator: R. P. Drake (University of Michigan)

Co-investigators: B. Loupiaz and E. Falize (CEA);

J. Holloway, C. Kuranz, P. Keiter, and K. Powell (University of Michigan); T. R. Boehly and D. H. Froula (LLE); T. Plewa (Florida State University); and B. A. Remington, S. Ross, H.-S. Park, and S. H. Glenzer (LLNL)

Recreating aspects of astrophysical phenomena on OMEGA provides the ability to quantitatively test observations and models in an experimental setting and is a long-term goal of our

research there. The OMEGA laser makes this feasible due to the very high-energy-density (>10-MBar) conditions it can create in millimeter-scale areas. This project includes various experiments exploring either the contribution of hydrodynamic instabilities to the structure in astrophysical systems such as supernovae or the dynamics of radiative shock waves. Here we discuss a continuation of successful campaigns at LLE that investigate the contribution of radiative shock waves to the evolving dynamics of binary star-accretion disk systems in which they reside.

Radiative shock waves produce shocked matter so hot that it radiates away most of its thermal energy. This radiation causes variable structure to develop depending on the optical properties of the material on either side of the shock. In an attempt to control these properties and understand the shock-front emission, this experiment produces an accelerating plasma flow into vacuum that becomes strongly shocked when the flow is impeded. We study the three-dimensional shock structure and the developing dynamics around it using stereoscopic x-ray radiography.

The experiments on OMEGA employ a laser configuration of ten UV beams with a 1-ns square pulse. They are focused on the 10- $\mu$ m plastic ablator whose opposite face is coated with 5  $\mu$ m of Sn. The beams deposit a total energy of  $\sim 4.5$  kJ, giving an average irradiance of  $\sim 1.2 \times 10^{15}$  W/cm<sup>2</sup>. After an ablative shock breaks out of the rear of the foil, the Sn plasma will expand, cool, and accelerate down the evacuated target cylinder at an average velocity of the order of 150 km/s. About 4 mm from the laser drive surface, the Sn ejecta impact a 100- $\mu$ m-thick, cold Al foil. In response, a reverse shock develops in the flow. The traditional “upstream” velocity in the shocked system is defined by the Sn flow, which is fast enough that the reverse shock will reach temperatures of a few hundred eV. As it radiatively cools, a thin dense layer of Sn will form, showing compressions much above the adiabatic limit of about 4. Additional sets of four OMEGA laser beams each irradiate zinc foils on orthogonally placed backlit pinhole targets for 1 ns, creating the x-ray sources used to radiograph the reverse shock onto film and image plates. Figure 132.50 shows a pair of images from a single experimental target shot, taken  $\sim 34$  ns after the drive laser pulse was turned off.

### Ramp Compression for Studying Equations of State, Phase Transformations, and Kinetics on OMEGA

Principal Investigator: T. Duffy (Princeton)

Co-investigators: R. Smith, J. H. Eggert, J. Hawreliak, C. Bolme, and D. Braun (LLNL); and T. R. Boehly (LLE)

The aim of this campaign was to measure powder diffraction of MgO under ramp compression. We used the PXRDIIP diagnostic

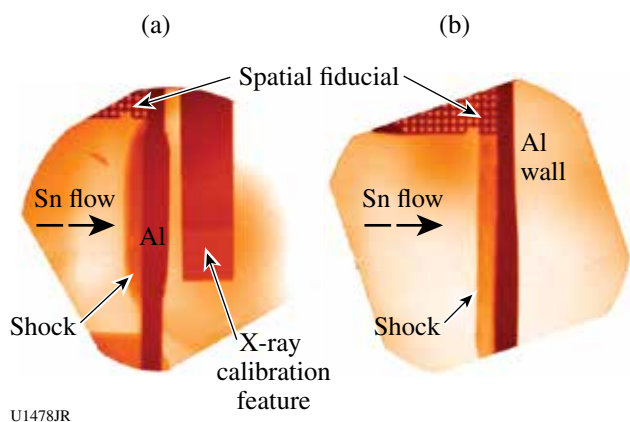


Figure 132.50

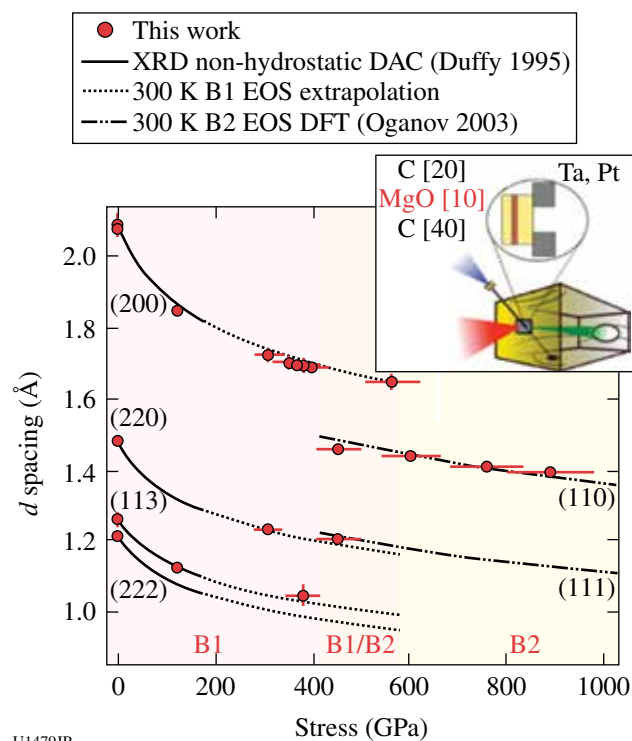
Orthogonal x-ray radiographs of a radiative reverse shock in a Sn plasma. The Al obstacle in the collision region of the experiment is  $1\text{ mm} \times 2\text{ mm} \times 100\text{ }\mu\text{m}$ . (a) The rebounding flow from the 1-mm side, in which we see the shock wave as well as the flow moving above and below it. (b) The orthogonal view along the 2-mm Al edge where it and the reverse shock span the field of view of the diagnostic. Both radiographs were taken at the same time.

reported in the inset of Fig. 132.51 to perform the experiments. Four OMEGA beams were focused on the main target (H7) to drive and compress the MgO powder (sandwiched between two diamonds) and up to ten beams were focused on a Fe or Cu backlighter (H2) to generate x-ray emission for diffraction measurements. We used a 3.5-ns ramp (rm3501) followed by a 1-ns square pulse (sg1018) to drive the main target and a 1-ns square pulse to drive the backlighter. The active shock breakout [velocity interferometer for any reflector (VISAR)] was used to estimate the pressure by measuring the free-surface velocity of the diamond.

MgO was ramp compressed to about 900 GPa and diffraction patterns were recorded. The measured  $d$  spacings are shown in Fig. 132.51 as a function of the applied stress. Below 400 GPa, our data (red dots) are in good agreement with static compression experiments (black line)<sup>1</sup> and their extrapolation to higher pressure (black dashed line). The clear discontinuity observed between 400 and 600 GPa is the first experimental evidence for the occurrence of a phase transition in solid MgO. Analysis of the diffraction data shows that the observed solid–solid transformation is consistent with the expected B1–B2 transition<sup>2</sup> (from the six-fold–coordinated NaCl structure to the eight-fold–coordinated CsCl structure).

**Detailed In-Situ Diagnostics of Higher-Z Shocks:  
Angularly Resolved Quasi-Elastic XRTS of Shocked  
Al Using 18-keV X Rays**

Principal Investigator: L. Fletcher (University of California, Berkeley)



U1479JR

Figure 132.51

Measured  $d$  spacing of ramp-compressed MgO. The red dots indicate our experimental data and the black curves indicate our data compared with data from the literature.<sup>1</sup> Below 400 GPa our data indicate that the B1 phase of MgO is the stable one. Above 600 GPa a new solid phase is observed and is consistent with the B2 phase.<sup>2</sup>

Co-investigators: T. Ma, A. Pak, H. J. Lee, T. Döppner, C. Fortmann, O. L. Landen, S. H. Glenzer, and R. Falcone (LLNL)

Molybdenum  $\text{He}_\alpha$  (18-keV) x rays have been used to probe Al foils that have been compressed using both single and double (counter-propagating) shocks in a forward, small-angle scattering platform with very high angular precision.

In this experiment two scattering platforms, demonstrated in Fig. 132.52, have been used. In one configuration [Fig. 132.52(a)], 125- $\mu\text{m}$ -thick Al targets were shock compressed up to  $3.5\times$  solid density using nine beams with a total energy of 4.5 kJ using stacked 1-ns pulses. In the second configuration [Fig. 132.52(b)], 200- $\mu\text{m}$ -thick Al targets were shock compressed, under a counter-propagating shock geometry, up to  $7\times$  solid density using 18 beams (nine stacked 1-ns pulses on each side), resulting in a total energy of 9 kJ delivered to the Al foil. Both experiments used SG4 distributed phase plates to achieve a smooth 800- $\mu\text{m}$  focal spot, yielding a total

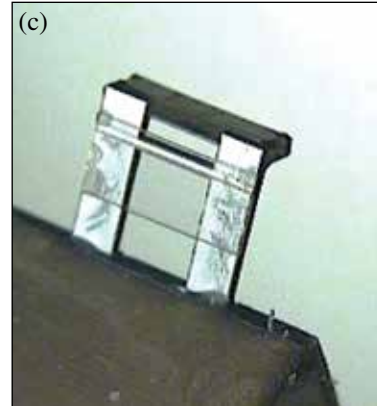
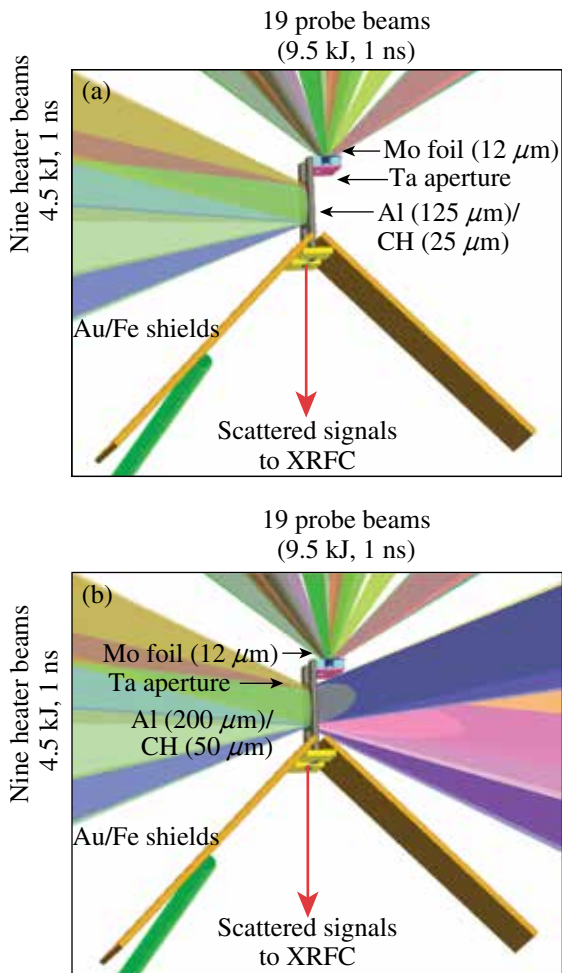
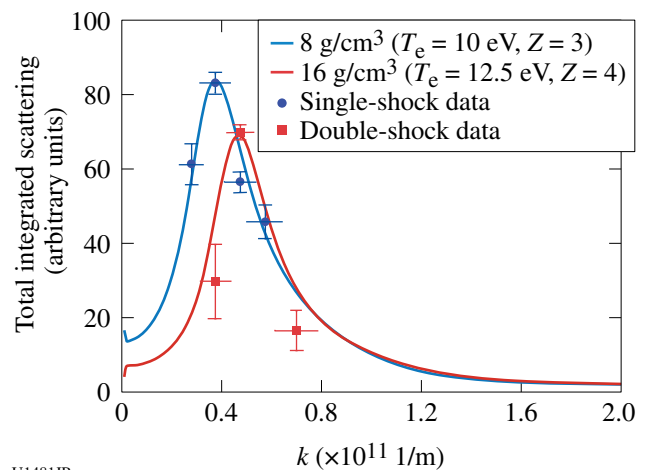


Figure 132.52 The experimental setup for HiZShk-12A. (a) A 125- $\mu\text{m}$ -thick Al target and beam configuration; (b) a 200- $\mu\text{m}$ -thick Al target and beam configuration; (c) a photo of the Al scattering target.

U1480JR

drive intensity of  $3 \times 10^{14} \text{ W/cm}^2$  on each irradiated surface. Nineteen beams were incident on a thin Mo foil to generate Mo  $\text{He}_\alpha$  x rays at 17.9 keV used to probe the compressed targets.

Figure 132.53 shows the predicted shift of the calculated elastic x-ray scattering amplitudes to higher wave numbers with increased density. Therefore, for higher densities, the mean separation between ions decreases while the wave number  $k$  increases, making it possible to observe the structure's peak shift. The width and shape of the angularly resolved scattering feature can provide additional information on temperature and the ionization state. By directly measuring the frequency-integrated, quasi-elastic contribution to the dynamic structure factor using angularly resolved x-ray Thomson scattering (XRTS), it is possible to infer the electron densities, electron temperatures, and ionization states of double- and single-shocked Al foils with one experimental platform. Our initial analysis of the scattered data demonstrates good agreement with the predicted quasi-elastic contribution.



U1481JR

Figure 132.53 Preliminary data analysis shows the total integrated signal of the scattering data as a function of  $k$ , following the trends predicted by the SOCP or OCP models using the frequency-integrated, quasi-elastic contribution to the dynamic structure factor of single-shocked ( $\rho = 8 \text{ g/cm}^3$ ) and double-shocked ( $\rho = 16 \text{ g/cm}^3$ ) aluminum.

**Measuring the Compression of Multishocked CH Ablators Using X-Ray Scattering**

Principal Investigator: L. Fletcher (University of California, Berkeley)

Co-investigators: A. Kritcher, A. Pak, T. Ma, T. Döppner, C. Fortmann, R. W. Lee, J. J. Lee, O. L. Landen, R. W. Falcone, and S. H. Glenzer (LLNL)

We have performed measurements of the electron densities, electron temperatures, and ionization states of spherically compressed multishocked CH capsules by using spectrally resolved x-ray Thomson scattering. Forty-five beams (13.5 kJ at 300 J/beam incident on a CH shell) compress the 70- $\mu\text{m}$ -thick CH shell above solid-mass density using a laser pulse shape comprised of three precisely timed coalescing shocks. Separately, a laser-produced, high-energy zinc He $\alpha$  x-ray source at 9 keV, delayed approximately 200 ps to 800 ps in time after maximum compression (full shock coalescence), is used to probe the plasma under a noncollective 135° scattering geometry.

Figure 132.54 shows a schematic of the experimental configuration and the target geometry. In addition, hydrodynamic simulations performed with Helios [Fig. 132.54(c)] demonstrate the possibility of compressing 70- $\mu\text{m}$ -thick CH

ablators up to 8.75 g/cm<sup>3</sup> using three co-propagating coalescing shocks. A mass density of approximately 8 $\times$  the initial solid density ( $\rho_{\text{CH}} = 1.1 \text{ g/cm}^3$ ) can be achieved using a pulse shape [Fig. 132.54(c)] with three timed steps of 1 ns, 1.5 ns, and 500 ps in duration along with precisely controlled amplitudes of 0.67 TW, 6.85 TW, and 15.5 TW, respectively. Figure 132.54(c) shows the measured radii of the CH shell superimposed on radiation-hydrodynamic simulations of the shell mass density as a function of time and shell radius. In the figure,  $t = 0 \text{ ns}$  indicates the start of the drive beams and  $t = 3 \text{ ns}$  indicates when the laser pulse has turned off. The simulations predict peak compression at the end of the 3-ns-long laser drive, at which time laser-produced x rays are used to probe the plasma by varying the delay between the drive laser beams (used to heat the CH capsule) and the probe laser beams incident on a Zn foil (used to produce high-energy zinc He $\alpha$  x rays).

The best fits to theoretical spectra shown in Fig. 132.55 allow one to infer the temperature, electron density, and ionization state of shock-compressed CH. The changing shape of the Compton feature with respect to time, as seen in Fig. 132.55, shows that the electron density and the electron temperature change with shock propagation. The Compton feature at each time of 3.4 ns, 3.5 ns, 3.6 ns, and 3.8 ns represents the response

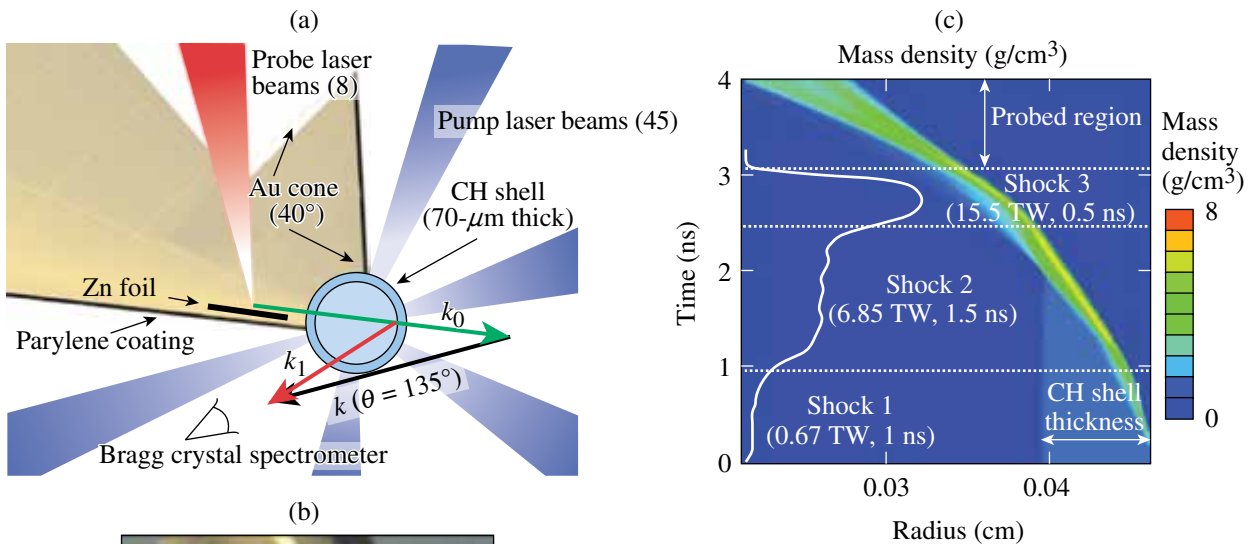
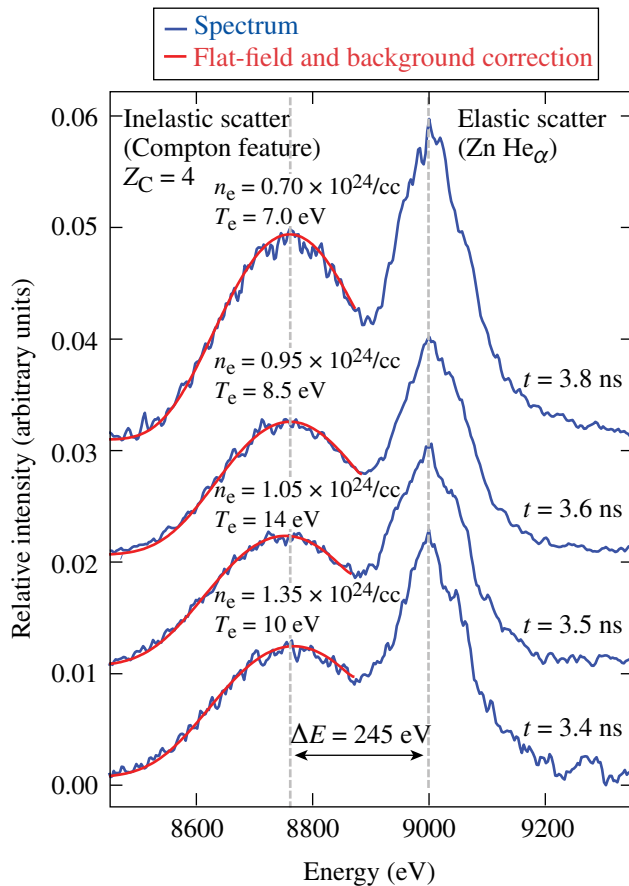


Figure 132.54

The experimental setup to study spherically convergent coalescing shocks in CH capsules. (a) A schematic diagram of the target geometry, laser-beam configuration, and  $k$  vectors. (b) A photograph of the CH cone-in-half-shell target. (c) Two-dimensional Helios simulation of the mass density as a function of CH shell radius and input-pulse shape parameters (power and time duration).

U1482JR



U1483JR

Figure 132.55  
Thomson-scattering curve fit analysis. Measured scattered spectra (blue) and best fit (red) to the Compton x-ray scatter features from multishocked CH ablators at  $t = 3.4$  ns,  $3.5$  ns,  $3.6$  ns, and  $3.8$  ns, yielding  $n_e$ ,  $T_e$ , and  $Z$ .

of the compressed state during shock coalescence. Our analysis, which provides a full characterization of the heating process, will enable us to completely describe the time-dependent hydrodynamic evolution of shock-compressed CH capsules. It can also be used as a platform to study current equation-of-state models of CH under similar extreme conditions.

### ***Clumpy Environments and Interacting Shock Waves: Realistic Laboratory Analogs of Astrophysical Flows***

Principal Investigator: P. Hartigan (Rice University)  
Co-investigators: J. Foster and P. Rosen (AWE); K. Yirak, B. Wilde, and M. Douglas (LANL); D. Martinez (LLNL); A. Frank (Rochester); and B. Blue (General Atomics)

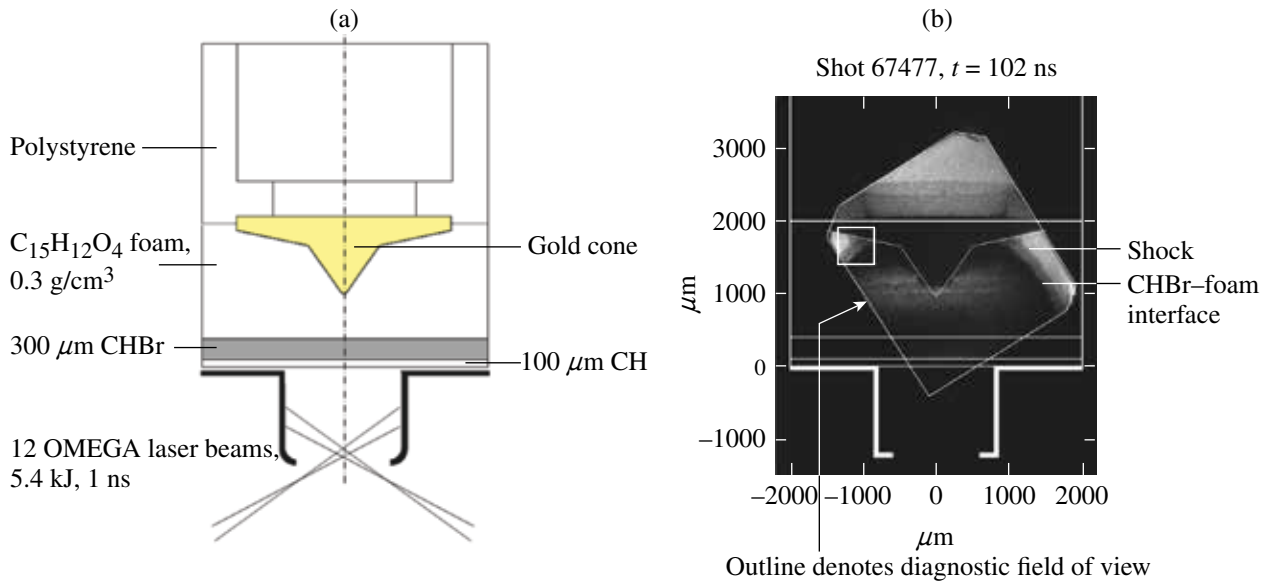
Motivated by recent astrophysical images from the Hubble Space Telescope (HST) that were taken as part of a previous NLUF program, our focus in the past year has been to recreate laboratory analogs of some of the shock structures present in

jets from young stars. Hot spots appear at the intersection points of overlapping shocks in the HST images, and it is possible that these represent transient normal shocks known as Mach stems. In the laboratory, one can study Mach stems when a strong shock wave moves along a surface. Mach stems may either grow, remain static, or vanish, depending on the intersection angle between the shock front and the surface. Our goals have been to quantify how easily Mach stems form and how fragile they are once formed.

In the last year we have been fielding a suite of experiments that control the angle of interaction between a shock wave and a reflecting surface. We do this by altering the shape of a cone embedded in foam into which we drive a strong shock front. One goal has been to study hysteresis, a phenomenon that allows a Mach stem, once formed, to persist even when the interaction angle decreases below the critical angle for formation. Another project has been to embed irregularities in the surface of the cone to determine how rough surfaces disrupt the growth and survival of Mach stems. We are also quantifying effects of preheating and ablation of the surface by radiation in the shock. A third goal has been to develop a second test bed that involves gas targets to study a system with a lower value (down to about 1.2) at gamma, the specific heat ratio. Theoretical work predicts that critical angles depend on gamma, and we will be testing that prediction. In the astrophysical case, the shock radiates and effectively lowers gamma, so it is important to understand how the system behaves when gamma deviates from the typical value of 5/3.

Examples of data from experiments fielded in the last year appear in Figs. 132.56–132.58. At the end of the campaign, we will have enough data taken at different delay times and with differently shaped cones to be able to measure growth rates for Mach stems under a variety of conditions and compare these results with predictions from simulations. These experiments are being designed using the LANL hydrocode *RAGE*. On the most-recent shot day we experimented with a design for the low-gamma gas targets that produced the expected behavior, but the image contrast was not sufficient to accurately measure Mach-stem sizes. After a modest redesign, we are ready to attempt this again with the next set of shots, where we will continue to fill out the parameter space of angles and delay times, as well as quantify the effects of preheating.

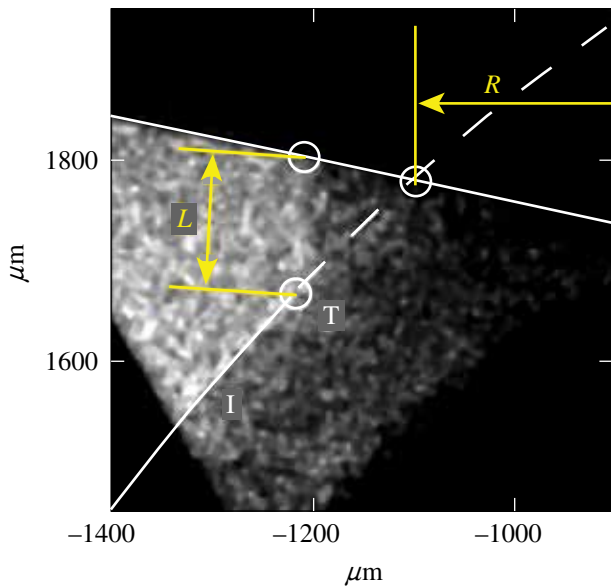
On the astrophysical side, we have discovered a way to image irradiated interfaces in regions of massive star formation. The technique involves taking narrowband images of fluoresced molecular hydrogen at near-infrared wavelengths



U1484JR

Figure 132.56

(a) Experiment to investigate hysteresis in the development of the Mach stem generated by reflection of a shock at the surface of a gold cone embedded in hydrocarbon foam. Radiation from a laser-heated hohlraum results in ablation of a CH and CHBr pusher that then drives a shock into foam containing the gold cone. (b) The experiment is diagnosed using point-projection backlighting radiography. The small,  $500\text{-}\mu\text{m}$ -sq region (surrounded by a white line) identifies the position of the Mach stem, shown in detail in Fig. 132.57. The profile of the gold cone is chosen to provide a specific trajectory of the angle of the incident shock at the cone's surface, as a function of time and radial position.



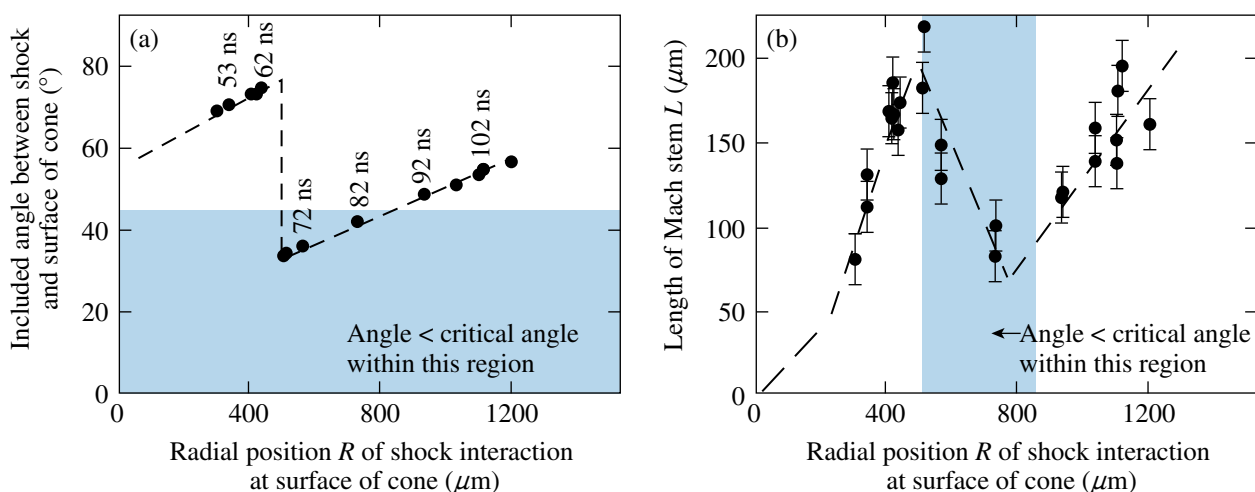
U1485JR

Figure 132.57

Detail taken from Fig. 132.56 showing the incident shock (I) and triple point (T). Metrics of the experiment are the length ( $L$ ) of the Mach stem, and the radial position ( $R$ ) at which the incident shock meets the surface of the cone. The  $30\text{-}\mu\text{m}$ -diam white circles identify the triple point and the points at which the Mach stem and the extrapolation of the incident shock meet the surface of the cone.

and subtracting off a suitable continuum image. The result shows where molecular clouds absorb ultraviolet radiation and allows us to observe any radiation-driven instability that may be present. It is impossible to do this observation directly at ultraviolet wavelengths because ambient dust causes the entire region to be opaque. An example of such an image, also used on the cover of the 2012 annual report of the NNSA Stewardship Science Academic Alliance program, appears in Fig. 132.59. Observations such as these provide a wonderful opportunity to study the physics of ablated interfaces, a subject of great interest in the laboratory as well.

Results from this work have appeared in several major journals, including High Energy Density Physics and the Astrophysical Journal. A status report on the Mach-stem work, including an analysis of the growth-rate information obtained thus far, was given by co-investigator K. Yirak at the most-recent HEDLA meeting, and a paper is in press to High Energy Density Physics. Additional papers on shock waves overrunning clumps (J. Foster *et al.*, in preparation) and irradiated interfaces (P. Hartigan *et al.*, High Energy Density Physics in press; P. Hartigan *et al.*, Astrophysical Journal in preparation) are forthcoming.



U1486JR

Figure 132.58

(a) Included angle between the incident shock and the surface of the cone and (b) length of Mach stem, both as functions of the radial position of the interaction of the incident shock with the reflecting surface. The growth, destruction, and later re-growth of the Mach stem are evident.



U1487JR

Figure 132.59

A color composite (red = H<sub>2</sub>, green = HI, blue = OIII) of a small portion of the Carina star formation region. The image reveals spectacular structures that arise when radiation from massive stars interacts with molecular globules that harbor newborn stars.

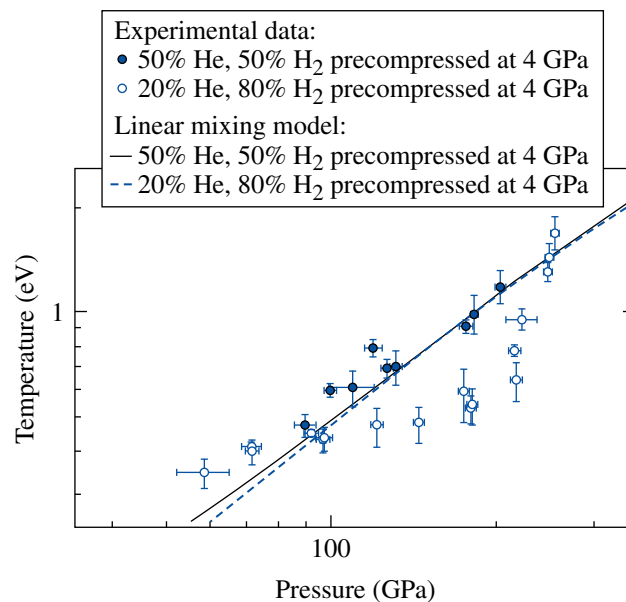
### Recreating Planetary Core Conditions on OMEGA

Principal Investigator: R. Jeanloz (University of California, Berkeley)

Co-investigators: P. Loubeyre (CEA); J. H. Eggert, D. G. Hicks, and G. W. Collins (LLNL); and T. R. Boehly (LLE)

We have extended the determination of the equation of state of dense fluid hydrogen by measuring the Hugoniot of D<sub>2</sub> precompressed in a diamond anvil cell to 6 GPa. We have also collected an extended pressure–density–temperature data set on hydro-

gen–helium mixtures precompressed to 4 GPa. Two He concentrations have been studied: 20 mol.% He and 50 mol.% He. A strong difference is observed between the shock temperature curves of these two concentrations. As illustrated in Fig. 132.60,



U1488JR

Figure 132.60

In FY12, the OMEGA laser was used to study hydrogen–helium mixtures at planet-core conditions. The H<sub>2</sub>, D<sub>2</sub>, and H<sub>2</sub>–He shock pressure and density were inferred by shock-velocity measurements impedance matched to a quartz standard. The temperature along the Hugoniot data for two different helium contents (20 mol.% He: open symbols; 50 mol.% He: solid symbols) provide evidence for demixing at 20 mol.% He by a drop of the temperature below the expected linear-mixing behavior that describes well the 50-mol.%-He mixture.

for a 20-mol.% He mixture, a strong *relative-cooling* effect is observed, whereas for 50 mol.%, the ideal mixing behavior is followed. We interpret this *relative-cooling* effect as the signature of the phase separation along the shock Hugoniot between 100 and 250 GPa. This result is important because it provides the first experimental evidence for a longstanding theoretical prediction that warm dense H–He fluid mixtures can undergo *unmixing*. This has direct astrophysical implications: a helium-rich phase may separate from hydrogen inside giant planets (so-called “helium rain”). This *differentiation* process releases gravitational energy that is thought to have greatly influenced the evolution of Saturn relative to Jupiter.

***Investigation of Hydrodynamic Stability and Shock Dynamics in OMEGA Direct-Drive Implosions Using Spectrally Resolved Imaging***

Principal Investigator: R. C. Mancini (University of Nevada, Reno) and R. Tommasini (LLNL)

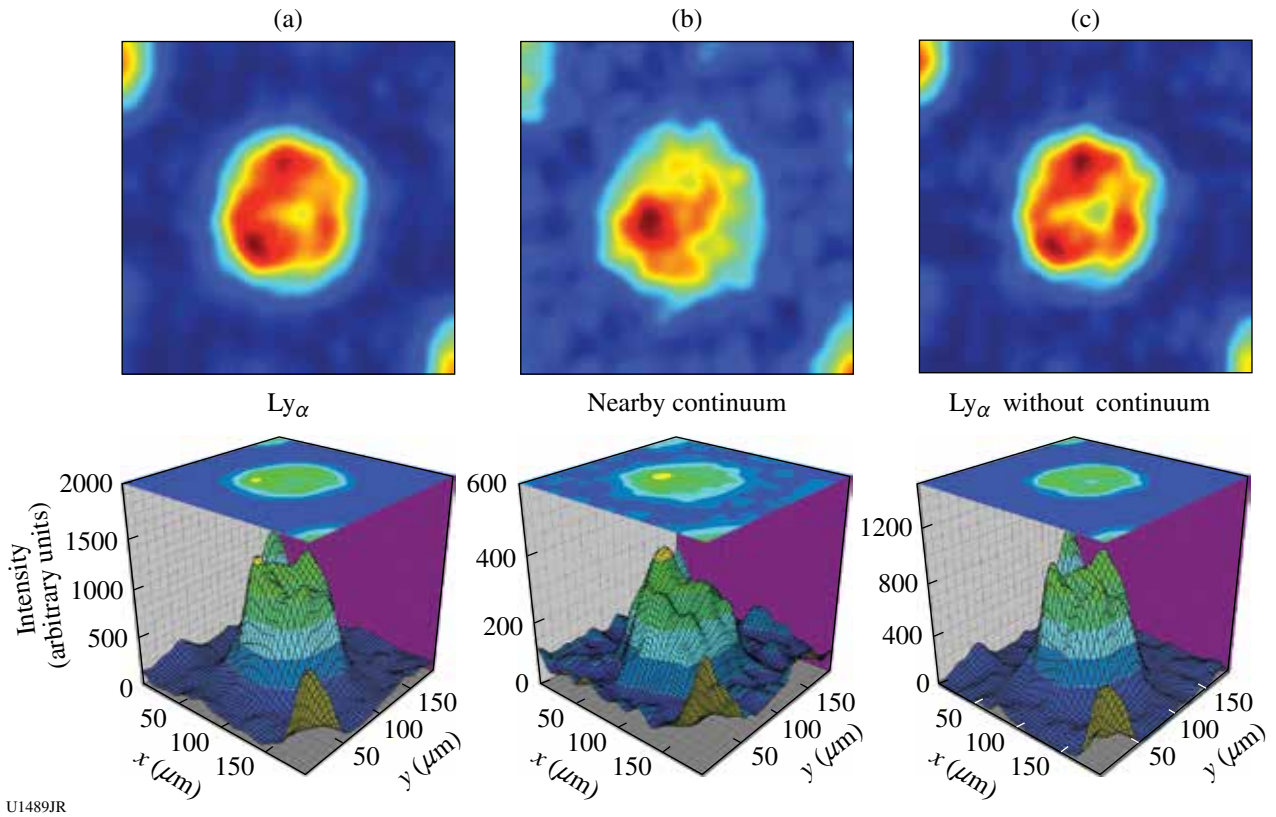
Co-investigators: J. A. Delettrez, S. P. Regan, and W. Theobald (LLE)

The multimonoenergetic (MMI) x-ray imager instrument records arrays of spectrally resolved images whose interpretation and analysis have created a new era for x-ray spectroscopy of inertial confinement fusion plasmas. The MMI data are based on spectrally, spatially, and time-resolved x-ray images because of the emission and/or absorption of radiation by a tracer element added to the plasma. The instrument combines pinhole-array imaging with the dispersion of a Bragg multilayer mirror and the time resolution provided by a framing (gated) camera detector. The MMI data are rich in information and its processing permits the extraction of narrow and broad images as well as space-integrated and space-resolved spectra.<sup>3</sup> The simultaneous and self-consistent analysis of sets of spatially resolved spectra observed along quasi-orthogonal directions has led to the demonstration of a new type of tomography, i.e., *polychromatic tomography*, which, unlike standard tomography, relies on data recorded along a limited number of lines-of-sight (LOS) but employs the information encoded in multiple wavelengths.<sup>4</sup> In this project, we apply spectrally resolved imaging to investigate the hydrodynamic stability and shock dynamics of low-adiabat, direct-drive implosions on OMEGA. In low-adiabat implosions, a nearly isentropic compression is launched by a shaped laser pulse drive that starts from a low intensity, gradually leading to a high intensity. By minimizing preheat, higher compressions are achieved in low-adiabat implosions compared to high-adiabat implosions, therefore making fundamental studies on the stability of low-

adiabat implosions relevant to high-energy-density-plasma hydrodynamics and, in particular, inertial confinement fusion. Furthermore, benchmarking of hydrodynamic codes with data from well-characterized implosions is important since these codes are also used to model and design low-adiabat cryogenic implosions and advanced ignition concepts.

The experiments on OMEGA consist of spherical implosions where the 60 OMEGA laser beams symmetrically illuminate a spherical shell filled with deuterium gas. The plastic shell has a 0.5- $\mu\text{m}$ -thick, plastic tracer layer doped with Ti at the 6% (atomic) level of concentration and initially located on the inner surface of the shell. Three identical MMI instruments fielded on TIM-3, TIM-4, and TIM-5 of the OMEGA chamber are used to record the x-ray signal of this spectroscopic tracer. Figures 132.61–132.63 illustrate some of the data processing and analysis results.

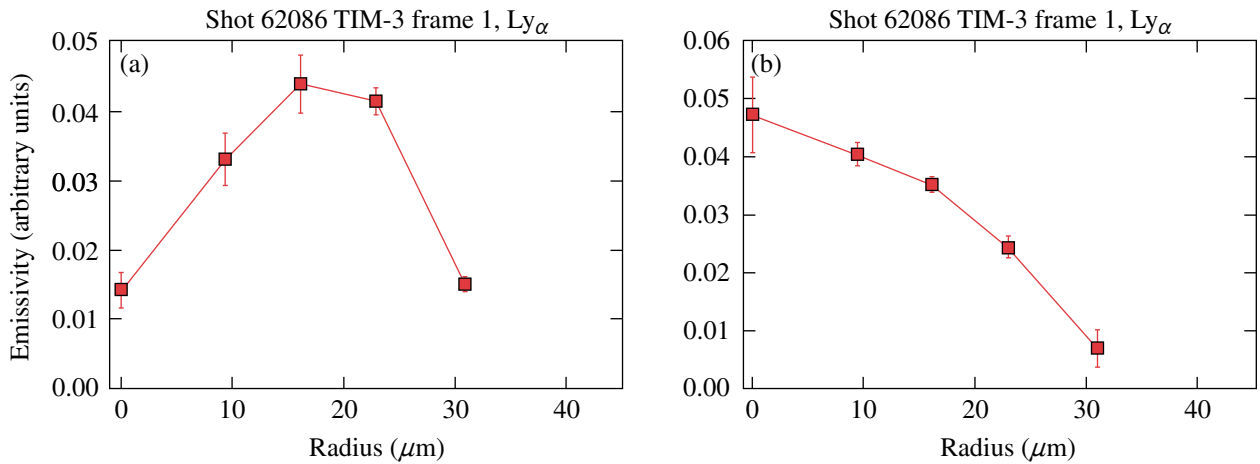
Figure 132.61 shows gated narrowband images reconstructed from spectrally resolved image data recorded in frame 1 of OMEGA shot 62086 with the MMI instrument mounted on TIM-3. In addition to the narrowband image based on the Ti Ly $\alpha$  line transition ( $1s-2p$ ,  $h\nu = 4979$  eV), an x-ray image of the same bandwidth based on the nearby continuum is also displayed. The fact that MMI data afford the extraction of images based on spectral signatures of the tracer, and the nearby continuum is important since it permits the removal of the underlying continuum from the line transition image and, therefore, produces a better approximation to the image due to just the line emission of the tracer; this image is also included in Fig. 132.61. In turn, the intensity distribution observed on the line emission image allows us to track the spatial localization of the tracer originally placed on the inner surface of the shell. Since in a perfectly stable, one-dimensional spherical implosion the tracer remains on the inner surface of the shell (i.e., core-shell boundary), the observation of the actual spatial distribution of tracer in the core (through its line emission) provides information about the stability and mixing of the implosion. In this regard, Fig. 132.62 displays the time evolution of the Ti Ly $\alpha$  line emissivity radial profiles in the core obtained from Abel inversion of angle-averaged narrowband images from data of the same OMEGA shot and TIM shown in Fig. 132.61. Results from two frames, i.e., frames 1 and 3, are shown that are characteristic of early and late times through the collapse of the implosion. The separation in time between frames 1 and 3 is approximately 200 ps. Early in time the tracer emission is localized away from the core center. Later in time, the tracer emission is seen to peak at the center of the core.



U1489JR

Figure 132.61

Gated narrowband images reconstructed from spectrally resolved image data recorded in frame 1 of OMEGA shot 62086 with the MMI instrument mounted on TIM-3. (a) Intensity map and surface plot of the Ti  $\text{Ly}_\alpha$  image; (b) intensity map and surface plot of the nearby continuum image; (c) intensity map and surface plot of the  $\text{Ly}_\alpha$  with the continuum removed.



U1490JR

Figure 132.62

Time evolution of the Ti  $\text{Ly}_\alpha$  line emissivity radial profiles in the core obtained from Abel inversion of angle-averaged narrowband images recorded on OMEGA shot 62086 with the MMI instrument mounted on TIM-3. (a) Early-in-time emissivity profile based on image data recorded in frame 1. (b) Later-in-time emissivity profile based on image data recorded in frame 3. The separation in time between frames 1 and 3 is  $\sim 200$  ps.

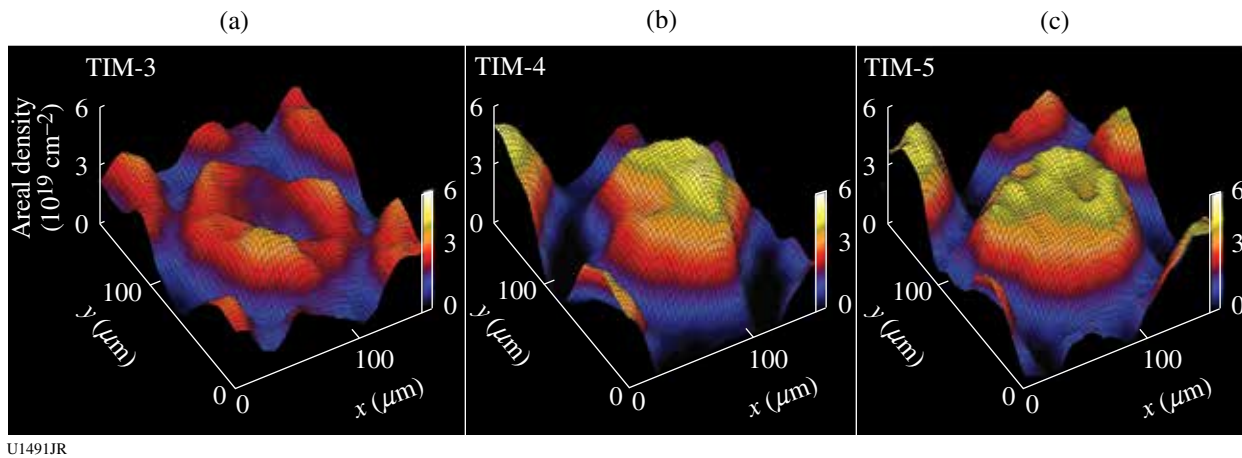


Figure 132.63

Areal-density surface plots extracted from the absorption signature of a Ti-doped tracer layer embedded in the plastic shell, initially located  $3 \mu\text{m}$  from the shell's inner surface. The data were recorded on OMEGA shot 49953 with three identical MMI instruments mounted on TIM-3, TIM-4, and TIM-5. The  $x$  and  $y$  axes' ranges of the surface plots are from  $0 \mu\text{m}$  to  $160 \mu\text{m}$ , and the  $z$ -axis range is from  $0 \text{ Ti-atoms/cm}^2$  to  $8 \times 10^{19} \text{ Ti-atoms/cm}^2$ , or  $\sim 45 \text{ mg/cm}^2$  of plastic areal density. This areal density is due to only the compressed plastic of the Ti-doped tracer layer.

Another important aspect of the stability and symmetry of the implosion is the uniformity of the compression of the (unablated) shell confining the implosion core. In this connection, Fig. 132.63 shows areal-density surface plots extracted from the absorption signature of a Ti-doped plastic tracer layer embedded in the plastic shell,  $1 \mu\text{m}$  thick with a 2% atomic concentration level and initially located  $3 \mu\text{m}$  from the shell's inner surface. In this case, the absorption is due to  $1s-2p$  line transitions in F- through He-like Ti ions that are backlit by continuum radiation coming from the hot spot in the core. The photon-energy range of these transitions spans the range from  $4450 \text{ eV}$  to  $4750 \text{ eV}$ . The data were recorded in OMEGA shot 49953 with three identical MMI instruments mounted on TIM-3, TIM-4, and TIM-5. We emphasize that this areal density is due to only the compressed plastic of the Ti-doped tracer layer and not the entire compressed shell. We also note that the areal-density maps are extracted in two different ways and checked against each other for consistency: on the one hand, from ratios of images based on the (attenuated) absorption feature and the (unattenuated) nearby continuum; on the other hand, from the analysis of sets of spatially resolved absorption spectra. The results displayed in Fig. 132.63 clearly show the modulations in areal density along a given LOS as well as the differences along different LOS. These results provide information about the stability and symmetry of the implosion.

#### ***Charged-Particle Probing of Inertial Confinement Fusion Implosions and High-Energy-Density Plasmas***

Principal Investigators: R. D. Petrasso and C. K. Li (MIT)

Co-investigators: F. H. Séguin and J. A. Frenje (MIT); T. C.

Sangster, V. Yu. Glebov, D. D. Meyerhofer, and R. Betti (LLE); and O. L. Landen (LLNL)

In FY12 MIT work included a wide range of experiments applying proton radiography, charged-particle spectrometry, and neutron spectrometry methods developed by MIT and collaborators to the study of high-energy-density physics (HEDP) and inertial confinement fusion (ICF) plasmas. Eighteen NLUF-related papers were published in FY12,<sup>5-22</sup> including four papers in *Physical Review Letters*,<sup>5,10-12</sup> and there were many invited talks and contributed talks at conferences. Our NLUF experiments also provided unique research opportunities in HEDP for eight MIT graduate students, who will use (or have already used) resultant data in major parts of their theses, and for several undergraduates.

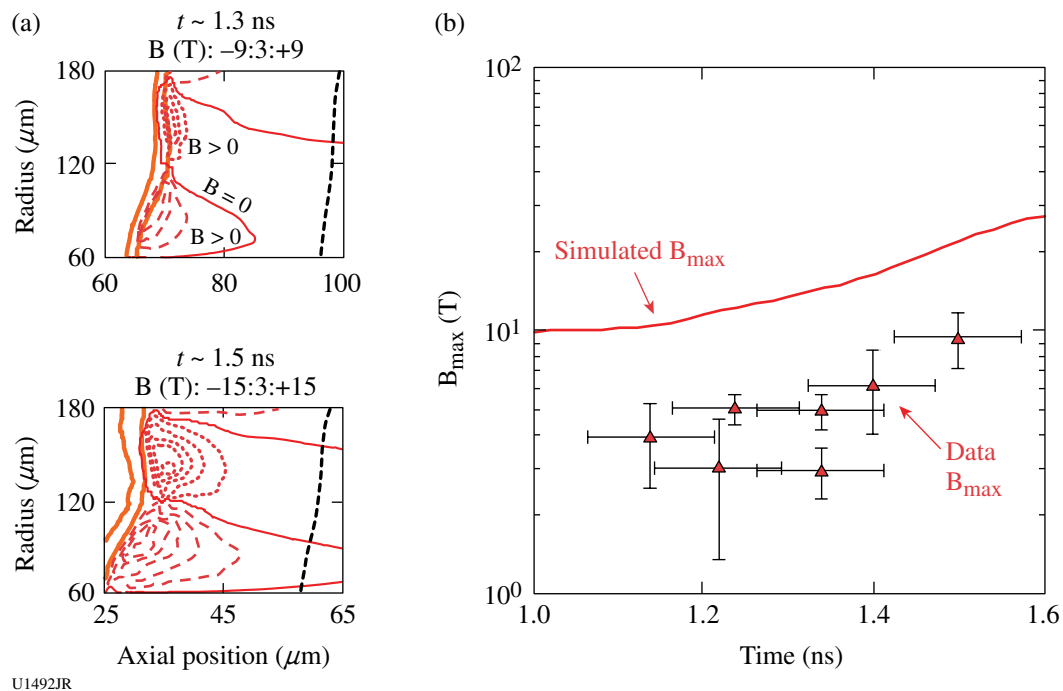
Topics studied on the OMEGA<sup>23</sup> and OMEGA EP<sup>24</sup> lasers included the imaging, identification, and measurement of electric and magnetic fields generated in direct- and indirect-drive ICF plasmas<sup>9,12,13,17,19,21</sup> and other laser-generated plasmas;<sup>7,9,10</sup> Rayleigh–Taylor<sup>7,10</sup> and other<sup>12,13</sup> instabilities; the characterization of ICF capsule implosions;<sup>8,11,13</sup> ions accelerated by laser–plasma interactions;<sup>6,8</sup> plasma nuclear science;<sup>5</sup> and diagnostic development.<sup>14-20,22</sup> The work successfully addressed basic physics issues and issues directly relevant to the future success of ignition experiments at the National Ignition Facility (NIF) as well as general issues of importance to HEDP and the physics of fields generated by laser–plasma interactions.

As described in Physical Review Letters<sup>10</sup> and illustrated in Fig. 132.64, monoenergetic, charged-particle radiography<sup>17,25</sup> was used to make the first measurements of magnetic fields generated by Rayleigh–Taylor (RT) instabilities.<sup>10</sup> Experiments were performed using laser-irradiated plastic (CH) foils with pre-imposed surface perturbations to stimulate the instability at a known spatial wavelength. Path-integrated field measurements were compared directly with benchmarked hydrodynamic simulations, and it was shown that diffusion processes were necessary to explain the observations.<sup>10</sup> Figure 132.64(a) illustrates that RT-induced fields are generated near the ablation front, where local resistivity is high; therefore, magnetic fields of the measured strength, shown in Fig. 132.64(b), will have a minimal impact on thermal heat conduction. This evidence demonstrated for the first time that RT-induced magnetic fields do *not* significantly reduce heat conduction in directly driven targets until perturbation growth reaches the hotter, more-conductive region near the critical surface.<sup>7</sup>

Work described in Physical Review Letters<sup>12</sup> and illustrated in Fig. 132.65 provided novel physics insight into the

effects of hohlraum fill gas on x-ray–driven implosions. The first time-gated proton radiography showing spatial structure and temporal evolution of fields and plasma in the hohlraum interior demonstrated that fill gas compresses wall blowoff, inhibits plasma jet formation, and impedes plasma stagnation. The important roles of spontaneously generated electric and magnetic fields in the hohlraum dynamics and capsule implosion were demonstrated. Interpenetration of blowoff and fill gas occurs as a result of the classical RT instability as the lighter, decelerating ionized fill gas pushes against the heavier, expanding gold wall blowoff. The results will have an important impact on the ongoing ignition experiments on the NIF.

Two other papers in Physical Review Letters<sup>5,11</sup> described important studies of basic nuclear physics and ICF dynamics. Neutron spectrometry was used to diagnose implosions of deuterium–tritium (DT)-gas–filled capsules on OMEGA. The neutron spectrum from the  $T(t,2n)^4\text{He}$  ( $tt$ ) reaction was measured<sup>5</sup> and used to study the  $tt$  reaction in thermonuclear plasmas at low reactant center-of-mass (c.m.) energies. When compared to accelerator experiments at higher c.m. energies



U1492JR

Figure 132.64

(a) Contour plots of magnetic fields from hydrodynamic simulations of a growing Rayleigh–Taylor instability in a laser-driven plastic foil that had machined grooves with a wavelength of  $120\ \mu\text{m}$  (thick solid orange). The times corresponding to the two plots are 1.3 and 1.5 ns during a 2-ns laser pulse. Magnetic-field contour levels are identified at the top of each plot and contours are indicated as follows: negative (into page) (red dots); positive (out of page) (red dashes); and zero contour (thin red solid line). Maximum field strength is clearly shown to occur near the ablation front, far from the hotter critical surface (short black dashes). (b) Comparison of measured and simulated peak magnetic fields. The factor of  $\sim 2$  discrepancy is due to exclusion of collisional terms (diffusion) in the model. For more information, see Refs. 7 and 10.

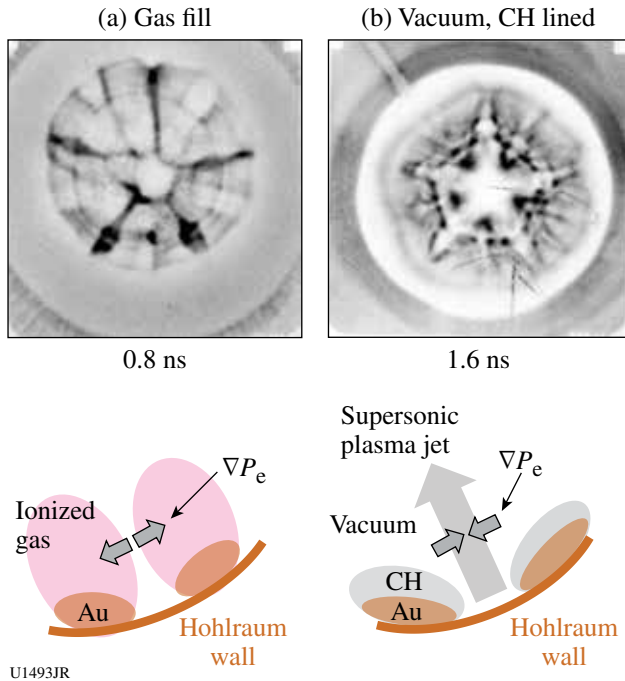


Figure 132.65  
Some differences between plasma behavior in laser-driven hohlraums (a) with gas fill and (b) without gas fill but with a CH liner, shown by proton radiography images. The images were recorded during indirect-drive ICF experiments, looking down the hohlraum axis from a CR-39 detector toward a monoenergetic, 15-MeV proton backlighter. The proton fluence distributions in these images show a proton surplus in the regions between pairs of expanding plasma plumes in (a) a gas-filled, Au hohlraum but a proton deficit in (b) a CH-lined, vacuum Au hohlraum, indicating opposing directions of the self-generated electric fields as illustrated schematically by the corresponding cartoons. For details, see Ref. 12.

(above 100 keV), the results indicate an energy-dependent  $n + {}^5\text{He}$  reaction channel branching ratio not previously recognized. In addition,  $\text{D}(d,p)\text{T}$  ( $dd$ ) and  $\text{T}(t, 2n){}^4\text{He}$  ( $tt$ ) reaction yields were measured and compared<sup>11</sup> with those of the  $\text{D}(t,n){}^4\text{He}$  ( $dt$ ) reaction yield. Absolute spectral measurements of  $dd$  protons and  $tt$  neutrons were measured. It was concluded that the  $dd$  yield is anomalously low and the  $tt$  yield is anomalously high relative to the  $dt$  yield, an observation that we conjecture to be caused by a stratification of the fuel in the implosion core. This effect may be present in ignition experiments planned on the NIF.

**Collisionless Shocks in Laboratory High-Energy-Density Plasmas**

Principal Investigator: A. Spitkovsky (Princeton)  
Co-investigators: L. Gargate (Princeton); H.-S. Park, B. A. Remington, S. Pollaine, and D. Ryutov (LLNL); J. P. Knauer, G. Fiksel, and R. Betti (LLE); Y. Sakawa, T. Ide, T. Kato, Y. Kuramitsu, T. Morita, and H. Takabe (Osaka University);

T. Bell (University of Oxford); M. Koenig and A. Ravasio (Ecole Polytechnique); and E. Liang (Rice University)

This NLUF program studies the creation of collisionless shocks in counter-propagating laser-produced plasmas. Collisionless shocks are of great importance in astrophysical and space plasmas and occur when the mean free path to Coulomb collisions is large compared to the size of the shock transition. The shock is then mediated by collective plasma effects as the result of the interaction between plasma particles and the self-generated electromagnetic fields. Collisionless plasma conditions can now be created on OMEGA and OMEGA EP, where the laser-driven plasmas propagate at speeds of  $\sim 1000$  km/s and densities of  $\sim 10^{18}$  to  $10^{19}$   $\text{cm}^{-3}$ . The experiments in this program collide two streams of high-speed plasma and study the formation of shocks as a function of an externally applied magnetic field that is generated by a set of Helmholtz coils at the interaction region (Fig. 132.66). The theoretical expectation is that at low external fields the shock is mediated by the filamentation (Weibel) instability, while at higher fields magnetic reflection of ions will form the shock. These regimes are representative of the conditions encountered in a range of astrophysical environments, including supernova remnant shocks and solar wind shocks. The experiments on OMEGA are testing these shock-formation mechanisms and addressing the open questions of astrophysical collisionless shock physics such as the presence of particle acceleration and the mechanisms of magnetic-field amplification in shocks.

In FY12, we performed shock experiments in a joint OMEGA/OMEGA EP shot day on 24 April 2012. In this experiment, we used the OMEGA laser to initiate two ablated plasma

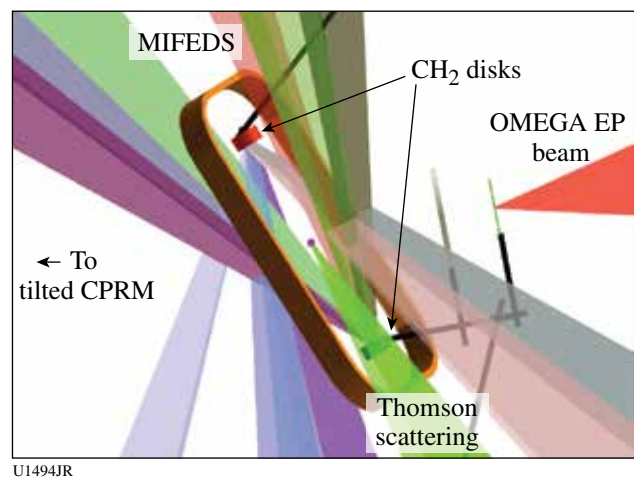


Figure 132.66  
Diagram of the experimental setup for NLUF MagShock-12a.

flows from CH foils. OMEGA EP was used to provide a short pulse for proton radiography of the interaction region. The new configuration of the magnetic coil was fielded (fabricated by G. Fiksel's group at LLE). The new design used a single coil, which delivered a higher peak magnetic field of 5 T (compared to 1 T in 2011). The diagnostics included Thomson scattering and proton radiography (delivered by a short pulse from OMEGA EP). We moved the radiochromic film pack (CPRM) closer to the target to obtain a wider field of view than in 2011. We performed seven shots (five joint) and are very thankful to the facility for providing outstanding support during this challenging experiment.

We studied the Thomson signal and proton images as a function of the external magnetic field and tried several time

offsets for diagnostics to build a time series. The Thomson signal was fairly insensitive to the magnetic field. The proton signal showed characteristic filamentation that we observed in 2011. It is important that this signal is reproducible. The field had a moderate effect on the early time signal [Figs. 132.67(a) and 132.68(a)]. Analysis of later snapshots (5 ns) is still continuing and requires additional shots to completely fill out the time series. This will be performed in 2013.

We modeled the proton signal using particle-in-cell (PIC) simulations. We concentrated on the unmagnetized 3-D PIC simulations of interpenetrating flows, tracing orbits of test protons through the simulation domain to accumulate proton images. The results (Fig. 132.69) show that we can reproduce main features of the interaction—turbulent ripples with horizon-

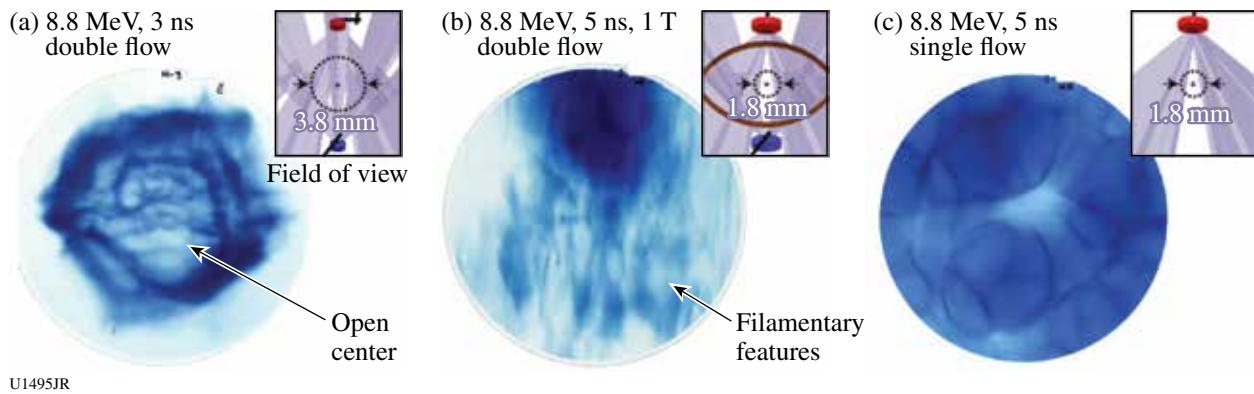


Figure 132.67 Proton images of plasma flows with little or no external magnetic field. (a) 3-ns counter-streaming flows, (b) 5-ns counter-streaming flows, and (c) 5-ns single-plasma flow. Insets: experimental configuration and proton-image field of view.

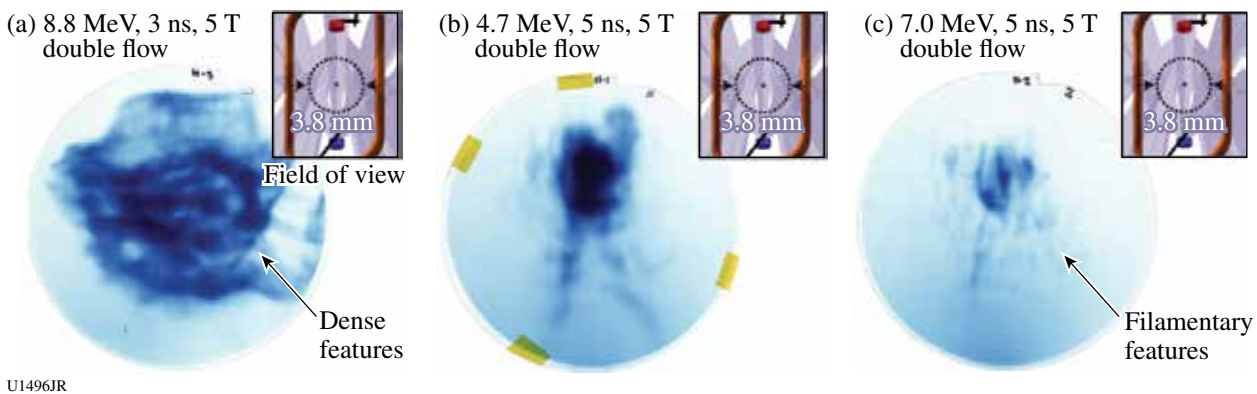


Figure 132.68 Proton images of counter-streaming plasma flows with a moderately strong external B field of 5 T. Both foils are illuminated. (a) 3 ns with 8.8-MeV protons, (b) 5 ns with 4.7-MeV protons, and (c) 5 ns with 7.0-MeV protons. Insets: experimental configuration and proton-image field of view.

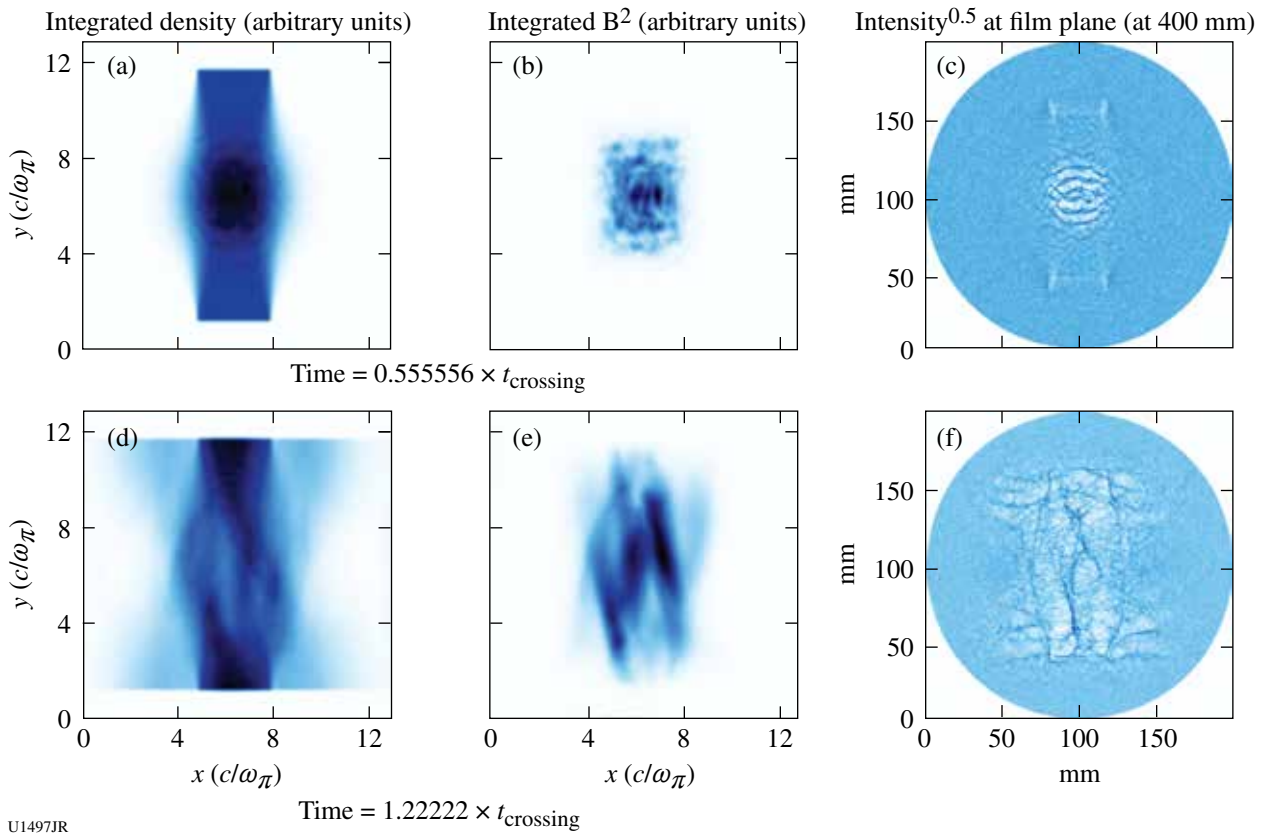


Figure 132.69

Simulated proton imaging using PIC simulations. Plasmas collide along the  $y$  axis. [(a),(d)] Time evolution of the integrated density and [(b),(e)] magnetic-energy profiles. [(c),(f)] Simulated proton imaging signal as collected on the film plate 400 mm from the proton source. These images show horizontal and bubble-like features at early times and filamentary features at late times. The field of view in (c) is  $2\times$  larger than in (f).

tal features at early times and longitudinal filaments at later times. The ripples are caused by electrostatic fields that are created in the first moments of collision, while the later filaments are driven by the magnetic field from the Weibel instability. We are currently exploring how the flow parameters can be better approximated in the simulation and checking whether any of the structures observed in the experiment are a result of electrostatic shocks.

We developed a suite of post-processing diagnostics for the PIC simulation code that allows us to calculate Thomson and radiography signals based on the full distribution function from the simulations. Preliminary analysis of the data and PIC simulations indicates that the next experiment in this program in FY12 will require stronger magnetic fields. The design work on increasing the magnetized inertial fusion energy delivery system (MIFEDS) magnetic fields is currently underway, and we expect another increase by a factor of 2 after the upgrade of MIFEDS.

This NLUF research has been reported in three peer-reviewed publications,<sup>26–28</sup> five invited papers,<sup>29–33</sup> and one contributed paper.<sup>34</sup>

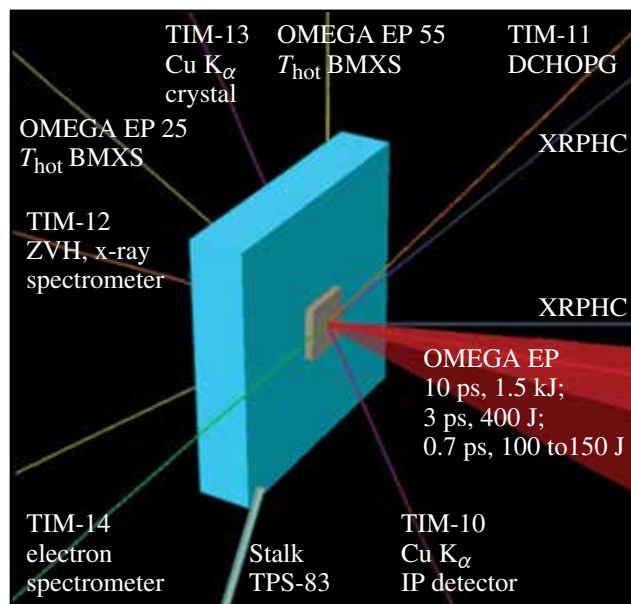
#### ***Investigation of Laser-to-Electron Energy Coupling Dependence on Laser Pulse Duration and Materials Composition***

Principal Investigators: M. S. Wei and R. B. Stephens (General Atomics)

Co-investigators: F. N. Beg, R. Mishra, H. Sawada, L. C. Jarrott, and J. Peebles (University of California, San Diego); H. McLean and P. Patel (LLNL); W. Theobald and C. Stoeckl (LLE); and Y. Sentoku (University of Nevada, Reno)  
Lead graduate student: A. Sorokovikova (University of California, San Diego)

Efficient conversion of laser energy to fast electrons (1 to 3 MeV) and their subsequent energy transport to the compressed fuel are extremely important for the success of fast ignition.

Energy coupling is controlled by the nature of the plasma (i.e., density profile, ionization, etc.) at the laser–plasma–interaction (LPI) interface and the dynamic response of the transport material, which both evolve with time, therefore dependent on laser pulse length. For full-scale fast ignition, the high-intensity ignitor pulse duration will be of the order of 10 ps. So far, most of the electron source and transport studies have been limited to subpicosecond pulses with energies  $\sim 100$  J. The goal of the General Atomics NLUF project is to extend such investigation to fast-ignition (FI)–relevant pulse durations using the high-energy ( $>1$ -kJ) OMEGA EP laser. In this second-year NLUF experiment in FY12, our study is focused on the effect of the laser pulse length on LPI and fast-electron source generation and the transport by systematically varying laser pulse duration from 0.7 ps up to 10 ps at a constant laser intensity and using identical multilayered planar-foil targets. Figure 132.70 shows the schematics of the target and experimental setup on the OMEGA EP laser. The planar multilayered foil targets consist of an Al substrate with a Cu x-ray tracer layer ( $20\ \mu\text{m}$  thick) buried  $\sim 100\ \mu\text{m}$  below the front surface and a large, thick ( $5\text{-mm} \times 5\text{-mm} \times 1\text{-mm}$ ) conductive carbon layer at the back to minimize fast-electron refluxing. The OMEGA EP backlighter beam was normally incident onto the front target surface. The beam was tightly focused with a spot radius of  $\sim 20\ \mu\text{m}$  within which contained 80% of the laser energy. The experiment was performed with identical targets at the same laser intensity ( $I_{\text{peak}} \sim 2 \times 10^{19}\ \text{W}/\text{cm}^2$ ) for three different laser pulse lengths,

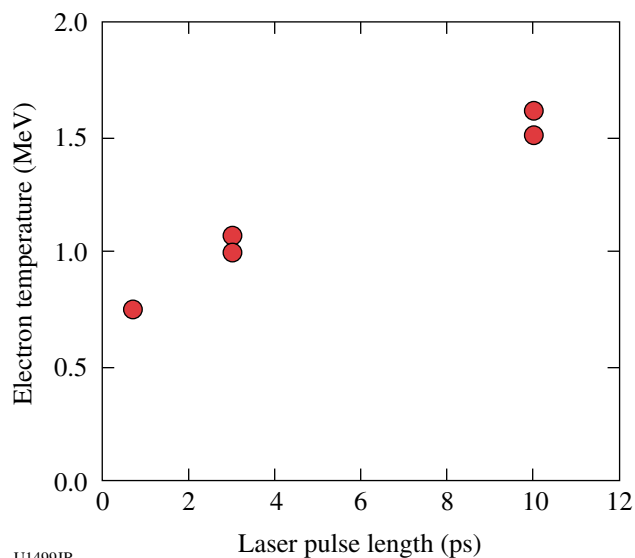


U1498JR

Figure 132.70  
Schematic of the experimental setup.

i.e., 0.7 ps, 3 ps, and 10 ps, with main pulse energies of 100 to 150 J, 400 J, and 1500 J, and prepulse energies of 5 mJ, 16 mJ, and 110 mJ, respectively. Fast electrons were characterized by the induced K-shell fluorescence from the Cu tracer layer and high-energy bremsstrahlung x rays from the whole target. Two-dimensional Cu  $K_{\alpha}$  spot and the total  $K_{\alpha}$  yield were measured with a spherical quartz crystal imager (SCI) and a calibrated x-ray spectrometer using a highly oriented pyrolytic graphite (HOPG) diffraction crystal, and the high-energy bremsstrahlung spectrum was monitored at two angles behind the targets with two fixed-port bremsstrahlung MeV x-ray spectrometers (BMXS), which were recently implemented in the OMEGA EP chamber by the PI and project team.

The measured bremsstrahlung spectrum data suggest a hotter energy distribution in the 10-ps interaction case. Figure 132.71 shows the inferred fast-electron temperature from the Monte Carlo modeling analysis fitting a synthetic electron energy distribution (one temperature exponential) to the measured bremsstrahlung spectrum. The slope temperature increased by a factor of 2, i.e.,  $\sim 1.5$  MeV in 10-ps LPI compared to 0.7 MeV in the 0.7-ps case. The 2-D Cu  $K_{\alpha}$  images (Fig. 132.72) showed a large change in LPI-produced electron-beam spatial distribution with increasing laser pulse duration. The fast-electron beam evolved from a single beam with a beam spot size of about  $160\ \mu\text{m}$  in a subpicosecond interaction into multiple narrow ( $\sim 70\text{-}\mu\text{m}$ ) filaments over a 10-ps pulse dura-



U1499JR

Figure 132.71  
Inferred fast-electrons' energy spectrum slope temperature from the measured bremsstrahlung spectrum data.

tion. The very large angular separation ( $\sim 45^\circ$ ) between these distinct filaments in the 10-ps case is quite unusual, indicating a significant deviation of energy flow directions from the original laser propagation axis. The observed new phenomena such as hotter energy distributions and multiple widely separated filaments can be caused by the presence of an extended pre-plasma in the 10-ps case. It is well known that LPI in a longer pre-plasma can produce fast electrons with a hotter electron spectrum as the result of stochastic heating. Extended pre-plasmas can also result in strong nonlinear LPI processes such as filamentation, hole boring, and hosing instabilities, which

can develop over a longer pulse duration leading to the formation of widely separated electron-beam filaments. Preliminary collisional particle-in-cell (PIC) simulations to examine LPI and fast-electron generation over 2 ps using the PICLS (PIC simulations for large-scale plasmas) code have suggested that these widely separated electron filaments could be initiated by the filamented and self-focused laser beam [Fig. 132.73(a)] in the long-scale-length pre-plasma, injecting electrons into solid plasmas at particular angles. These electron filaments could be further pinched by self-generated resistive magnetic fields inside the high-density plasmas as shown in Figs. 132.73(b)

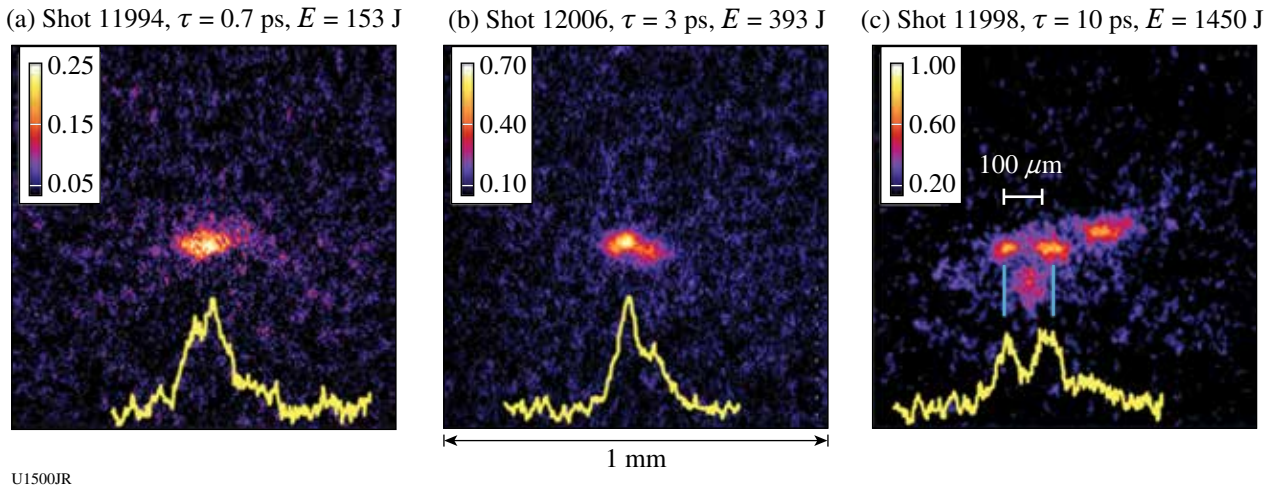


Figure 132.72 Cu  $K_\alpha$  fluorescence images showing a fast-electron beam cross section  $\sim 100 \mu\text{m}$  below the generating point using a laser pulse of (a) 0.7 ps, 153 J, (b) 3 ps, 393 J, and (c) 10 ps, 1450 J in the OMEGA EP experiment. All images are to the same spatial scale and compressed vertically because of the view angle. The yellow lines at the bottom of each image are plots of the pixel intensity along a horizontal line through the points.

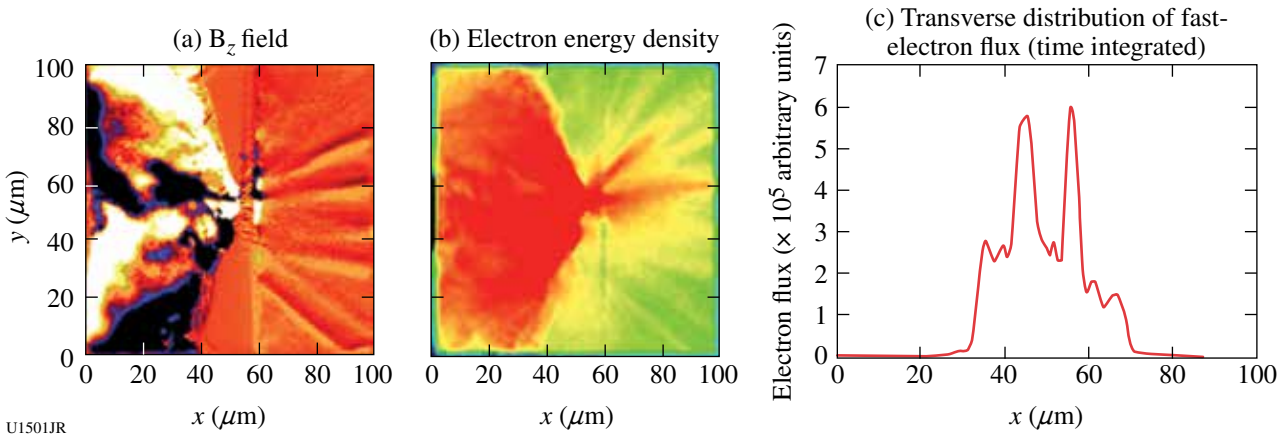


Figure 132.73 Preliminary 2-D PIC modeling results of LPI and fast-electron generation over a 2-ps pulse duration. The semi-infinite high-intensity laser with a focal-spot size of  $30 \mu\text{m}$  rises to peak intensity ( $10^{20} \text{ W/cm}^2$ ) in 330 fs and stays constant. The target is a planar Al slab with a pre-plasma ( $8\text{-}\mu\text{m}$  density scale length) in front of the solid Al. (a) Quasi-static azimuthal  $B_z$  field; (b) electron energy density at 2 ps; and (c) the transverse profile of the time-integrated fast-electron flux taken in a  $2\text{-}\mu\text{m}$ -thick,  $100\text{-}\mu\text{m}$ -wide sampling box at  $x = 65 \mu\text{m}$ .

and 132.73(c). Although this simulation was performed with a much higher laser intensity, the pre-plasma scale length is of a similar order as that in our experiment and the observed phenomena may be applicable to the observed electron filaments in our experiment. Simulations with the realistic laser and pre-plasma parameters are underway, which will examine the dependence of beam filaments on pre-plasma scale length and pulse duration.

In summary, the FY12 GA-led NLUF experiment has systematically investigated the dynamics of the LPI-produced fast-electron source generation and transport from subpicosecond to over 10-ps pulse durations. We observed formation of multiple electron filaments in LPI with a longer scale length of pre-plasma over 10 ps. Future experiments using the newly available ultrahigh-contrast OMEGA EP pulses are planned to further examine the LPI and electron-beam dynamics in an initially pre-plasma free condition to help identify the roles of the pre-plasma and pulse length on the laser filaments and resistive beam filamentation.

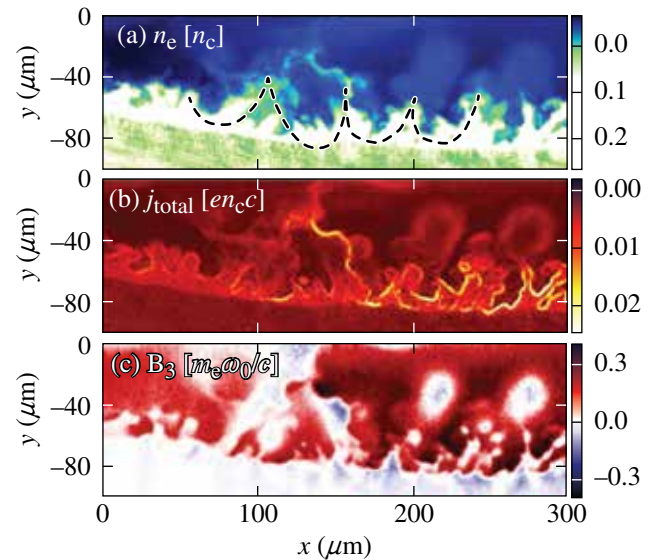
#### **Intense Laser Interactions with Low-Density Plasma Using OMEGA EP**

Principal Investigator: L. Willingale, C. Zwick, A. G. R. Thomas, A. Maksimchuk, and K. Krushelnick (University of Michigan); P. M. Nilson, R. S. Craxton, C. Stoeckl, V. Yu. Glebov, and T. C. Sangster (LLE); H. Chen (LLNL); J. Cobble (LANL); and P. Norreys (RAL)

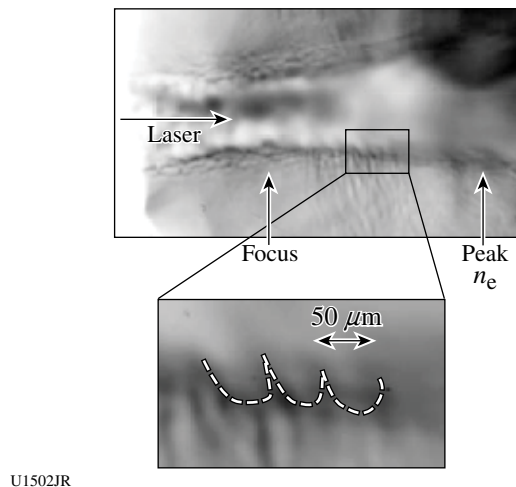
The study of high-intensity laser interactions with low-density plasma is of interest to many phenomena such as channeling,<sup>35</sup> electron and ion acceleration, and neutron and x-ray production. The focus of the low-density plasma campaign this year has been to investigate electron acceleration and neutron production. To generate an underdense target, a long-pulse beam (2.5 ns, ~1200 J in an 800- $\mu\text{m}$ -diam focal spot) is used to create a plasma plume from a plastic-foil target. The main interaction beam is then focused into the plasma plume, with the laser propagating parallel to the target surface so that it sees an approximately Gaussian density profile (2-D *SAGE* modeling estimates the plasma-density profile).

Electron spectra along the laser axis were measured using the electron positron proton spectrometer (EPPS). High-energy electrons with an effective beam temperature many times greater than the ponderomotive potential were measured under several different laser pulse-length and energy conditions. Since the channels are almost completely cavitated at OMEGA EP laser intensities, a plasma wakefield cannot be responsible for

the electron acceleration. Instead, particle-in-cell simulations indicate that a direct laser acceleration (DLA) mechanism is responsible.<sup>36</sup> For the electrons to be accelerated via DLA, they must be injected into the cavitated channel with some initial momentum. Based on proton probe data showing the channel formation, periodic modulations are observed at the channel wall [Fig. 132.74(d)], which are consistent with surface wave formation. Particle-in-cell simulations indicate the surface waves can act as the required injection mechanism for DLA.<sup>37</sup>



(d) Experimental proton probe image of the channel



U1502JR

Figure 132.74

Particle-in-cell simulation data showing the modulations in the channel wall region in (a) electron density, (b) the total current, and (c) the transverse magnetic field. (d) Experimental proton probe image of the channel wall illustrating the periodic modulations.

Figures 132.74(a)–132.74(c) show simulation data illustrating the surface wave modulation that has been driven in the channel walls. High-temperature electron spectra are also observed in the simulations.

The shape of the neutron spectra from underdense plasma interactions can enable us to estimate the ion heating within the channel.<sup>38</sup> For the neutron-production experiment, deuterated polyethylene (CD<sub>2</sub>) targets were used instead of the regular CH<sub>2</sub> targets. To measure the neutrons, a time-of-flight scintillator diagnostic that was gated using a microchannel plate to reduce the signal from the prompt gamma flash. Simultaneously, the transverse ion spectrum was measured using the Thomson parabola ion spectrometer (TPIE). Figure 132.75(a) shows an example of a time-of-flight trace and indicates the main features. Figure 132.75(b) shows the uncalibrated neutron spectra comparing the signal from CH and CD plasma at the same plasma density and under the same laser conditions. The residual signal from the prompt  $\gamma$  flash means that it is not possible to measure neutrons with energies >12 MeV. A plasma density scan was also performed and indicated higher neutron yield for higher plasma density as would be expected [shown in Fig. 132.75(c)]. Analysis is underway to address

calibration and saturation effects for the neutron diagnostic so that comparison with the measured ion spectra and qualitative conclusions can be made.

The authors gratefully acknowledge the *OSIRIS* consortium for the use of the *OSIRIS* 2.0 code.

**FY12 Laboratory Basic Science Programs**

In FY12, LLE issued a solicitation for LBS proposals to be conducted in FY13. A total of 32 proposals were submitted. An independent review committee reviewed the proposals and recommended that 16 proposals receive 28 shot days at the Omega Laser Facility in FY13. Table 132.VIII lists the successful LBS proposals.

Fifteen LBS projects were allotted Omega Facility shot time and conducted a total of 273 target shots at the facility in FY12. This work is summarized in this section.

**Measurements of the Viscosity of Shock-Compressed Fluids: Studies of Water and Silica**

Principal Investigators: P. M. Celliers and M. A. Barrios (LLNL)

This is the second in a series of experiments that aims to demonstrate a method for determining the viscosity of a high-pressure fluid created by the propagation of a strong shock front through an initially transparent sample. The measurement technique is based on observing the evolution of a spectrum of perturbations imposed on a multi-Mbar shock front passing through the sample material. The viscosity of the liquid state just behind the shock front is expected to influence the decay rate of the perturbations as the shock front propagates; detailed measurements of the perturbation state can be compared with calculations to assess the viscosity. The sample under study is liquid silica (SiO<sub>2</sub>), produced by propagating the shock through samples of either alpha-quartz or fused silica. The viscosity of high-pressure liquid silica has obvious geophysical relevance, and measurements in the Mbar domain are impossible with conventional methods. An earlier campaign in 2010 examined the shock response to a perturbation spectrum that was generated by an etched array of shallow pits a few microns deep and 10  $\mu$ m in diameter that were created on the sample surface at the interface with the ablator. The 2012 campaigns examined the response to a random distribution of surface perturbations generated by roughening the silica surface with a grinding technique. Initial experiments in October 2011 used the active shock breakout (ASBO)/streaked optical pyrometer (SOP) to perform hohlraum drive characterization measurements in preparation

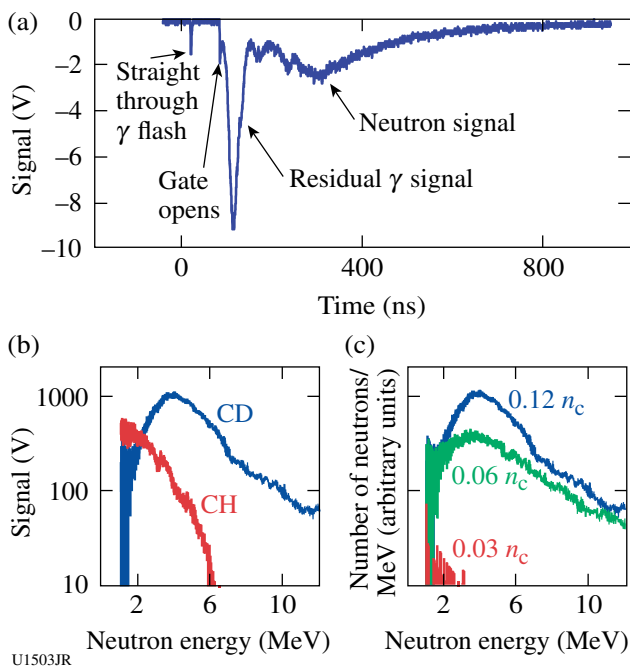


Figure 132.75 (a) Time-of-flight trace showing the main features of the signal. Uncalibrated, preliminary neutron spectra comparing (b) CH with CD plasma shots and (c) different peak CD plasma density shots.

Table 132.VIII: Approved FY13 LBS proposals.

Principal Investigator	Affiliation	Project Title
P. M. Celliers	LLNL	Equation of State and Optical Properties of Dense Silica: Shock Study of Coesite and Stishovite
H. Chen	LLNL	Exploring Pair Plasma and Their Applications Using OMEGA EP
J. R. Davies	LLE	Fast-Electron Control with Magnetic Field in Hohlräum
J. H. Eggert	LLNL	HED Condensed Matter: Magnesium and Aluminum
G. Fiksel	LLE	Magnetic Reconnection and Particle Energization in High-Energy-Density Plasmas in the Presence of an External Magnetic Field
G. Fiksel	LLE	Magnetized ICF Implosions on OMEGA
R. F. Heeter	LLNL	“Gatling Gun” Long-Duration Radiation Sources on OMEGA EP for Sustained-Drive Hydrodynamics and Low-Density Atomic Physics Applications on OMEGA EP and the NIF
B. R. Maddox	LLNL	Direct Measurements of Dislocation-Based Plastic Flow in Quasi-Isentropically Compressed bcc Metals
H.-S. Park	LLNL	Astrophysical Collisionless Shock Generation by Laser-Driven Experiments
P. K. Patel	LLNL	Areal-Density Measurements of Cone-in-Shell Implosions Using Compton Radiography for Fast Ignition
Y. Ping	LLNL	Long-Term Dynamics of Hole Boring and Target Heating at Fast-Ignition-Relevant Conditions
S. P. Regan	LLE	Collective X-Ray Scattering from Shocked Liquid Deuterium
J. R. Rygg	LLNL	Extreme Chemistry, Equation of State, and Optical Properties of Dense Water at Terapascal Pressure
A. A. Solodov	LLE	Fast-Ignition Integrated Experiments with Low-Z Cone-Tip Targets
C. Stoeckl	LLNL	Spectroscopy of Neutrons Generated Through Nuclear Reactions with Light Ions in Short-Pulse Laser-Interaction Experiments
W. Theobald	LLE	Laser Channeling in Long-Scale-Length, Overdense Plasmas

for the rippled shock measurements carried out in May 2012. The second campaign in May used the OMEGA high-resolution velocimeter (OHRV) to observe the velocity perturbations directly on the surface of the reflecting shock front.

The shocks were driven using a hohlraum coupled to a 50- $\mu\text{m}$  poly(methylmethacrylate) (PMMA) ablator followed by the sample. As the shock passed through this interface, the perturbations were transferred to the shock front, which were detected and measured quantitatively by the OHRV. An example of a 2-D velocity spectrum recorded on these experiments is shown in Fig. 132.76. Examples of averaged velocity spectra for  $\sim 170$ -GPa shocks driven into fused silica are shown in Fig. 132.77, along with model calculations of the expected velocity spectra assuming a viscosity of 35 poise. The model calculations employ an analytical expression derived by Miller and Ahrens.<sup>39</sup> Detailed analysis of these data is at a preliminary stage; the goal is to fit the data set to the analytical model in

order to estimate the viscosity. Initial indications suggest that the viscosity is in the range of a few poise to tens of poise.

***Exploring Pair Plasma and Its Applications Using OMEGA and OMEGA EP***

Principal Investigator: H. Chen (LLNL)

In FY12, an LLNL/LLE team performed a Laboratory Basic Science (LBS) experiment on OMEGA EP to study positron production during high-intensity laser interactions with high-Z targets. This experiment was a follow-up on to those of 2010 and 2011. In the previous experiments, a record number of positrons were produced using the 1-kJ, 10-ps OMEGA EP backlighter interacting with a 1-mm-thick Au target.<sup>40</sup> It was deduced that a non-neutral pair plasma was made in those shots.<sup>41</sup> In FY11, the laser energy was extended to 1400 J for the backlighter beam, and a seemingly faster increase in positron number was observed once the laser energy exceeded 1 kJ. In

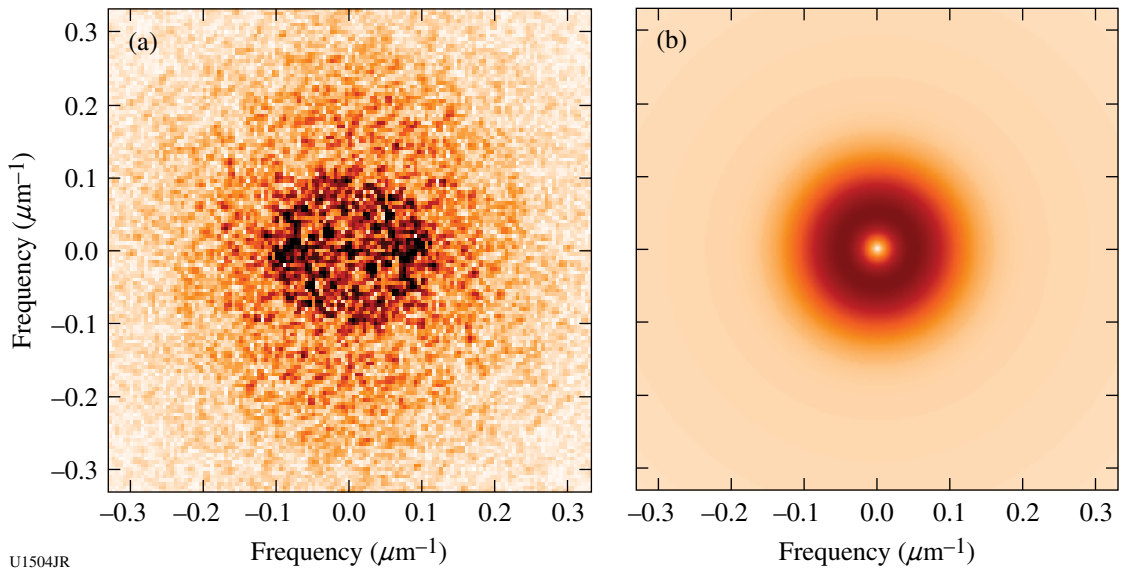


Figure 132.76 (a) An example of a 2-D velocity spectrum on a rippled shock front generated at a roughened interface between a PMMA ablator and a fused-silica sample recorded 650 ps after the passage of the shock through the interface (shot 66008). The gray scale is proportional to mode amplitude. (b) A velocity spectrum computed for similar conditions as in the experiment using the analytical expression provided in Ref. 39.

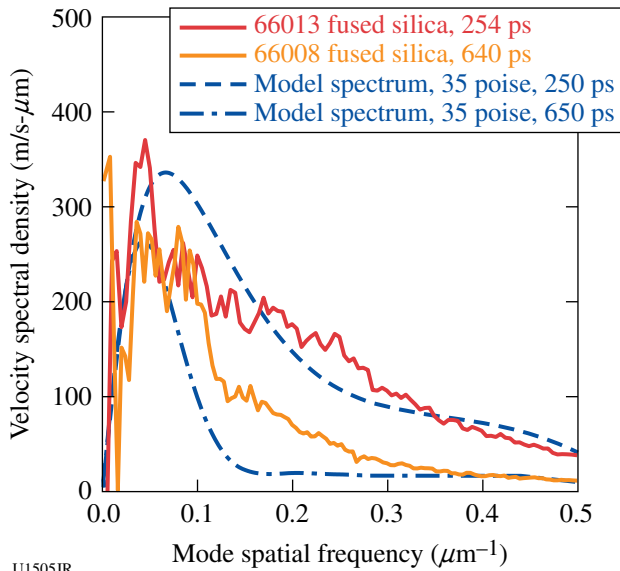


Figure 132.77 Averaged velocity spectra for ~170-GPa shocks in fused silica recorded at 250 ps and 650 ps after passing through the interface, compared with calculations of the expected spectra assuming 35-poise viscosity. More precise fits to the model are in progress.

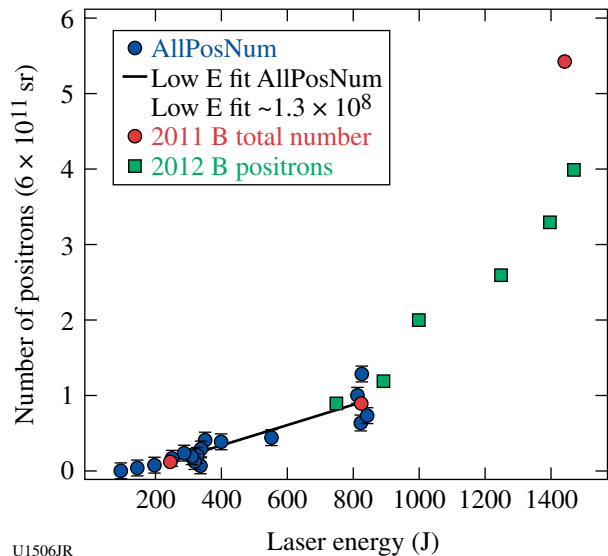
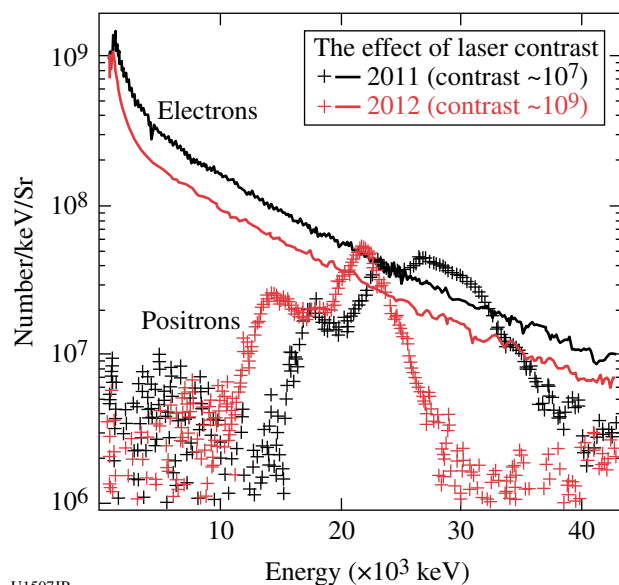


Figure 132.78 Positron yield is nonlinear at higher laser energies (green squares) in 2012B, confirming the conclusion from previous OMEGA EP experiments.

FY12, we carried out systematic experiments to confirm this finding. The preliminary results are shown in Figs. 132.78 and 132.79. At a higher laser-contrast condition ( $10^9$  versus  $10^7$  in FY11), the positron scaling remains “nonlinear” at laser energies greater than 1000 J. The effect of laser contrast to fast elec-

trons and positrons was also observed. Further data analysis is in progress to evaluate the laser–electron conversion efficiency as a result of enhanced contrast. Positron research extends over diverse fields ranging from particle physics and astrophysics to medical application. This often requires the production of



U1507JR

Figure 132.79

Fewer electrons were made in 2012B apparently due to a higher contrast laser condition, resulting in fewer and lower-energy positrons.

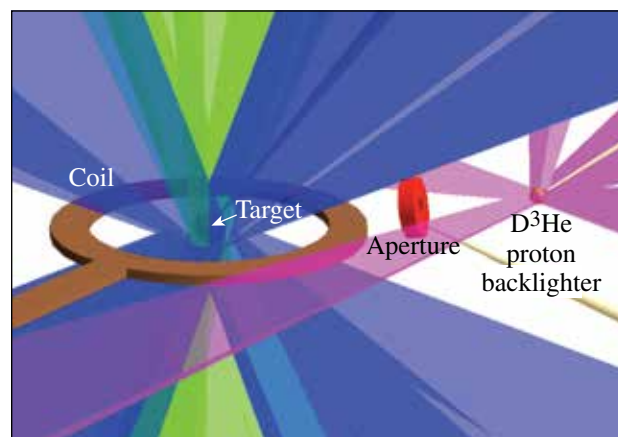
large numbers of positrons on a short time scale, which has been difficult to supply. The new OMEGA EP results could alter the direction of the quest to establish a laser-produced positron source for research in these fields.

### Magnetic-Field Compression in Spherical Implosions on OMEGA

Principal Investigators: G. Fiksel, M. Hohenberger, J. P. Knauer, and P.-Y. Chang (LLE); R. Betti, K. S. Anderson, and J. R. Davies (FSC/LLE); and F. H. Séguin (MIT)

*Project objective:* The main goal of the experiments was to measure the compressed magnetic field in spherically imploded targets embedded in an externally generated seed field. These experiments will establish the scientific basis for magnetizing high-energy-density (HED) plasmas and enhancing the performance of inertial fusion implosions through the use of magnetic fields.

*Experimental setup:* The experimental setup is illustrated in Fig. 132.80. A spherical CH target is embedded in a seed magnetic field generated by a single-loop coil powered by the magnetized inertial fusion energy delivery system (MIFEDS) generator. The target is then imploded by 40 OMEGA beams with a square 1-ns pulse at maximum power. The shell is filled with 5 atm of deuterium gas. The shell's outer diameter is 860  $\mu\text{m}$ , and the shell's thickness is 24  $\mu\text{m}$ . The compressed magnetic field will be measured by the proton radiography



U1508JR

Figure 132.80

Experimental setup to measure magnetic-field compression.

technique. The 14.7-MeV fusion protons, used to radiograph the compressed core and field, are produced by the  $\text{D} + {}^3\text{He}$  fusion reactions from an imploding glass microballoon filled with an 18-atm  $\text{D}^3\text{He}$  gas mix. The implosion of the proton backlighter is driven by ten OMEGA beams. The protons are recorded on a CR-39 nuclear track detector stack that allows for both spatial and energy resolution (via the track diameter) of the particles incident on the surface. The backlighter implosion can be timed so the backlighter proton beam passes through the target at the desired time of peak compression (e.g., “bang” time).

*Preliminary results and future plans:* Despite good laser performance and excellent MIFEDS operations, the obtained proton radiography images did not indicate the presence of deflected fast protons. After analyzing the results, a conclusion was made that the fast-proton fluence was too low and because the compressed magnetized spot has a diameter of less than 20  $\mu\text{m}$ , the number of deflected protons was low as well, comparable to the background noise level of the CR39 detectors. In future experiments we plan to use fast protons generated from the interaction of OMEGA EP with a thin metal foil. The OMEGA EP-generated fast-proton fluence is at least three orders of magnitude higher than that from the  $\text{D}^3\text{He}$  source.

### Magnetic Reconnection in High-Energy-Density Plasmas in the Presence of an External Magnetic Field

Principal Investigators: G. Fiksel and P. M. Nilson (LLE); and W. Fox and A. Bhattacharjee (University of New Hampshire)

*Project objectives:* The primary goals for the magnetic-reconnection experiments are to (1) demonstrate that an

extended reconnection current sheet can be formed in the gap between two laser-irradiated foils by the collision of the high-conductivity blowoff plasmas, (2) show that this interaction can be well diagnosed using proton radiography and x-ray imaging, and (3) observe basic properties of the reconnection, such as inflow and outflow rates, the geometry of the current sheet, and the magnitude of the magnetic field in the current sheet.

*Experimental setup:* Figure 132.81 shows a simplified diagram of the experiment on OMEGA EP. The experiment was carried out in close collaboration with the computational plasma physics group at the University of New Hampshire. This group has recently conducted particle simulations of reconnection in LLE and Rutherford (UK) laser-driven reconnection experiments.

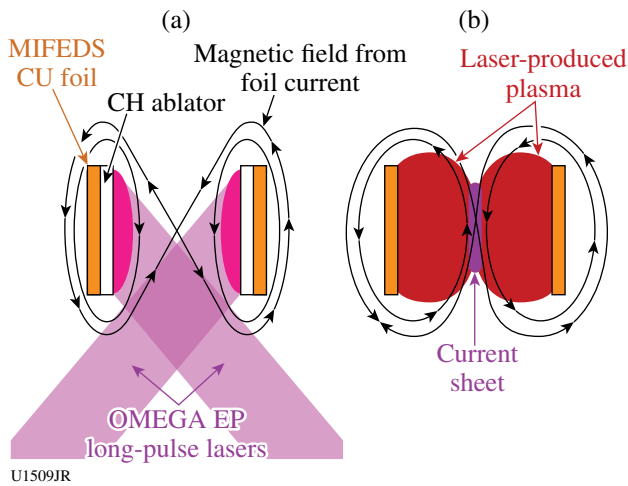


Figure 132.81  
A simplified diagram of the proposed reconnection experiments. (a) Laser-driven plasma blowoff drives the collision of two magnetized plasma flows and reconnection of the (b) seed magnetic fields from the MIFEDS current generator.

For the first series of shots (5 September 2012) the magnetic coils were not energized. The main goal of that experiment was to establish proper parameters of the drive lasers and investigate the dynamics of the colliding plasmas with the proton radiography diagnostic. The actual experimental setup is shown in Fig. 132.82.

*Preliminary results and future plans:* One of the proton images of the colliding plasma interface is shown in Fig. 132.83. The result indicates the presence of a long-lived, self-organized structure similar to what was recently described

in a Nature Physics publication.<sup>26</sup> A new series of experiments on characterization of the reconnection magnetic field and particle energization is planned.

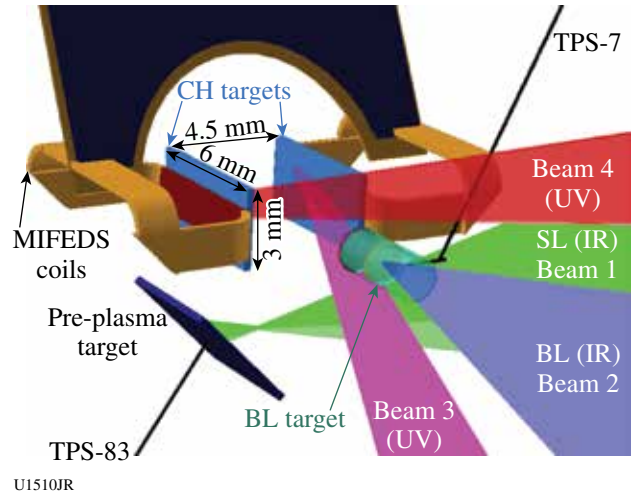


Figure 132.82  
The experimental setup showing MIFEDS coils with the support structure and the attached CH targets. The colliding plasmas are generated with 1.8-kJ, 2-ns OMEGA EP Beams 3 and 4. The proton backlighter beam is generated by the 800-J, 10-ps OMEGA EP Beam 2. The protons are detected with a radiochromic film (RCF)-based detector situated 8 cm away from the target. Also shown is a target for prefilling the intercoil region with pre-plasma.

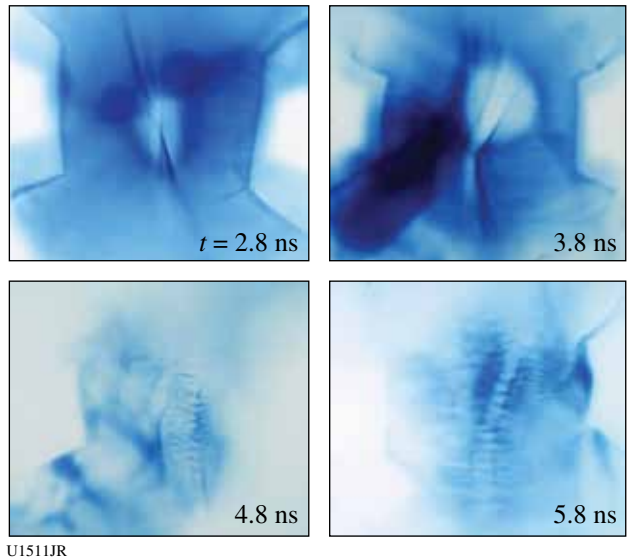


Figure 132.83  
A series of images of the colliding plasmas obtained with the proton radiography diagnostic.

**Measurements of Linear, Nonlinear, and Turbulent Mixing Regimes in Kelvin–Helmholtz Instability in the Subsonic Regime**

Principal Investigators: O. A. Hurricane and V. A. Smalyuk (LLNL)

A Kelvin–Helmholtz (KH) growth experiment was performed using a platform successfully developed in earlier OMEGA experiments.<sup>42–44</sup> Figure 132.84 shows a target schematic that consists of a plastic ablator and a shock tube. In the shock tube the interface between low-density foam and high-density plastic was either flat or had pre-imposed sinusoidal modulation at a 400- $\mu\text{m}$  wavelength and a 30- $\mu\text{m}$  amplitude, as in previous experiments. The central part of the plastic target contained a layer of I-doped CH to increase the contrast to 5-keV backlighter x rays. The ablator of the target was directly driven with laser light, producing a strong shock that propagated through the target. The shock produced a velocity gradient at the interface between foam and plastic. This velocity difference between two materials resulted in the KH growth of the surface modulations. The density of foam

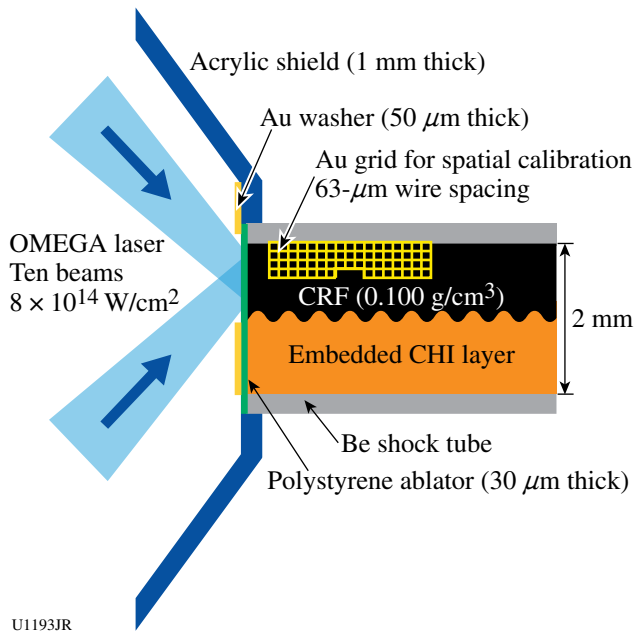


Figure 132.84 Experimental configuration. The interface between lower-density CRF foam and higher-density I-doped plastic was either flat or had a pre-imposed 2-D modulation with a 400- $\mu\text{m}$  wavelength, as in previous experiments. The surface roughness at the interface had a rms amplitude of 100 nm. The density of the CRF foam was 100 mg/cm<sup>3</sup>.

was 100 mg/cm<sup>3</sup>. Previous experiments detected a mixing layer development caused by the growth of 3-D, short-scale modulations in addition to pre-imposed, 2-D, 400- $\mu\text{m}$ -wavelength modulations. New experiments performed with flat CH–foam interfaces were aimed at measurements of 3-D turbulent mixing since in previous experiments the growth of large 400- $\mu\text{m}$ -wavelength modulations could have modified the growth of 3-D, short-scale modulations.

Figure 132.85 shows the experimental data. Figures 132.85(a) and 132.85(b) present flat-interface data at 35 ns and 75 ns, respectively. Figure 132.85(c) shows data with 2-D pre-imposed modulation at 75 ns, taken to confirm evolution measured in previous experiments. The shock traveled from left to right, so the modulations at the left-hand side of the image had more time to grow than the modulations at the right-hand side. The

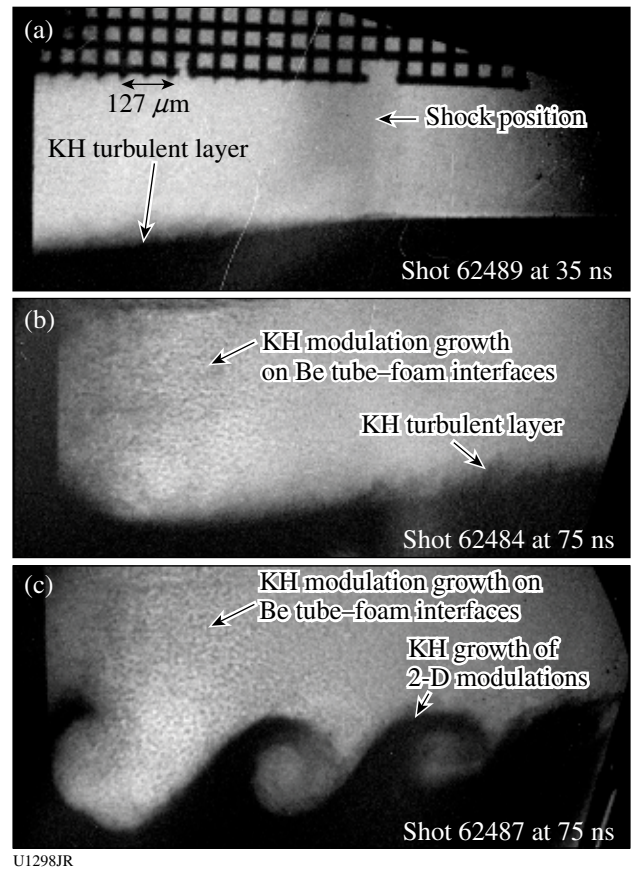


Figure 132.85 X-ray radiographs of KH growth with a flat CHI–foam interface were taken at (a) 35 ns, (b) 75 ns, and (c) with an interface having a 2-D modulation at 75 ns. The areas on the right-hand side of the images experienced less KH growth than the areas on the left-hand side.

light color in the image corresponds to foam material, while the dark color corresponds to plastic. A mixing layer developed behind the shock front, as expected since the Reynolds number was high in this experiment,  $Re \sim 1 \times 10^6$ . The mix width was  $\sim 60 \mu\text{m}$  at  $\sim 700 \mu\text{m}$  behind the shock front, inferred from the measured image at 35 ns, close to mix-model predictions. Growth of 2-D pre-imposed modulations [Fig. 132.85(c)] was similar to previous experiments, confirming the repeatability of the drive. In addition, growth of 3-D modulations at the Be tube–foam interfaces was also detected, as shown in both 75-ns images. These experimental data are used to develop and validate mix models that are based on post-processing of hydrodynamic simulations.<sup>45–47</sup>

**Nuclear-Atomic-Plasma Interactions in Laser-Produced Plasmas (NEEC and NEET)**

Principal Investigator: A. L. Kritcher (LLNL)

Plasma coupling to nuclei in high-energy-density plasmas, or nuclear–plasma physics, is a cutting-edge field that traverses the areas of nuclear physics, plasma physics, and atomic physics. Nuclear–plasma interactions occur in hot and dense plasmas such as inertial confinement fusion environments and astrophysical bodies. The effect of high-energy-density-plasma

(HEDP) environments on astrophysical nucleosynthesis, the formation of heavy elements from pre-existing nucleons in astrophysical plasmas, is expected to play a significant role.<sup>48</sup> Nuclei in stellar plasmas reach a thermal population of low-lying excited nuclear states from photoexcitation, free electrons in the plasma (NEEC),<sup>49–52</sup> excitation from atomic transitions (NEET),<sup>53–55</sup> and inelastic electron scattering in the dense plasma. In these experiments at the Omega facility, we investigate the NEEC process in underdense plasmas by illuminating mini hot hohlraums (400 or 600  $\mu\text{m}$  in diameter) with  $\sim 15 \text{ kJ}$  of laser light (Fig. 132.86).

The goal of these first experiments was to identify the plasma conditions of hot Tm hohlraums with spectral line emission analysis and optical Thomson scattering, measure the energy and time-resolved atomic emission background, investigate this experimental platform to study nuclear lifetime shortening in hot plasmas, and determine the possibility to investigate nuclear–plasma interactions. We collected high-quality data and are in the process of analyzing the results. Future campaigns will continue to measure plasma conditions of hot hohlraums and investigate nuclear–plasma interactions in HEDP plasma environments. We will also field additional isotopes in this configuration.

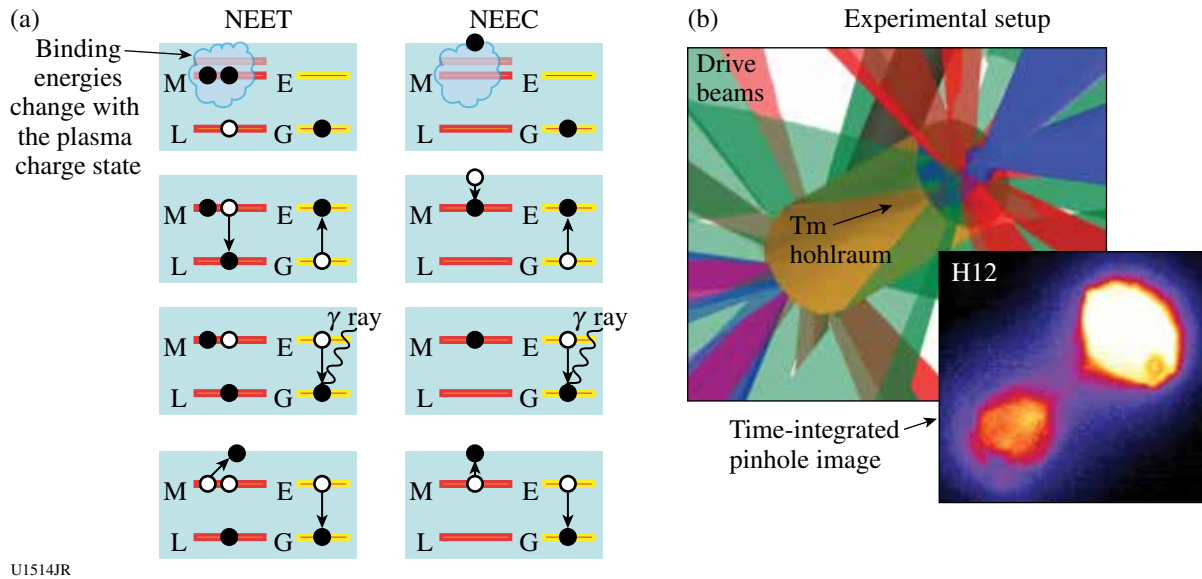


Figure 132.86

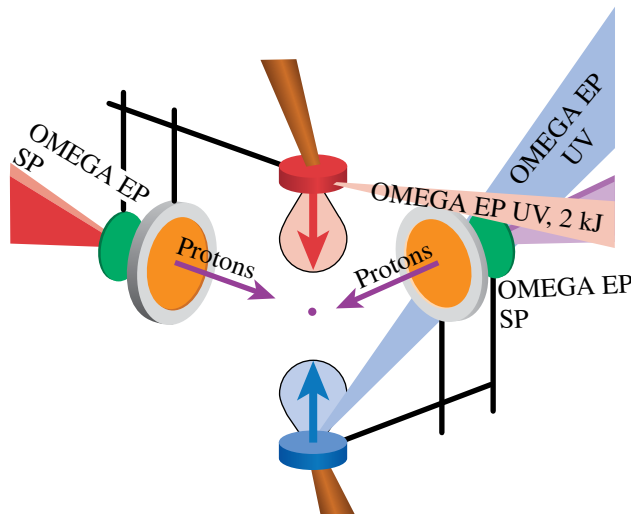
(a) Schematic of the NEET and NEEC processes. The red levels on the left-hand side denote the atomic shells; the yellow levels on the right-hand side denote the nuclear excited and ground states. First, the nucleus in the ground state and atomic shell vacancies are present (and/or free electrons are present). Electrons either transition or are captured into atomic states and the nucleus becomes excited. The nucleus radioactively decays by  $\gamma$ -ray emission or internal conversion. (b) A schematic of the experimental configuration. Tm hohlraums, 400 and 600  $\mu\text{m}$  in diameter, are illuminated by 40 drive beams with a total of 15 to 20 kJ.

**Astrophysical Collisionless Shock Generation by Laser-Driven Laboratory Experiments on OMEGA and OMEGA EP**

Principal Investigators: N. Kugland, S. Ross, and H.-S. Park (LLNL)

The goal of this experiment is to study astrophysical collisionless shocks with counter-streaming plasmas from high-power lasers. Astrophysical “collisionless” shocks form via plasma instabilities and self-generated magnetic fields. Laboratory experiments at large laser facilities can achieve the conditions necessary for the formation of collisionless shocks and will provide a unique avenue for studying the nonlinear physics of shock waves. We are performing a series of experiments on the OMEGA and OMEGA EP lasers in which collisionless shock conditions will be generated by the two high-speed plasma flows resulting from the laser ablation of solid targets using 10 kJ to 20 kJ of laser energy. The experiments will aim to answer several questions of relevance to collisionless shock physics: the importance of the electromagnetic filamentation (Weibel) instability in shock formation, the self-generation of magnetic fields in shock collisions, the influence of external magnetic fields on shock formation, and the signatures of particle acceleration in shocks.

Our second year of OMEGA EP experiments (EP-ACSEL-12A and EP-ACSEL-12B) continued proton imaging to visualize the electromagnetic fields produced by two counter-streaming plasmas. As shown in Fig. 132.87, these plasmas were made by two UV beams that irradiated plastic or carbon



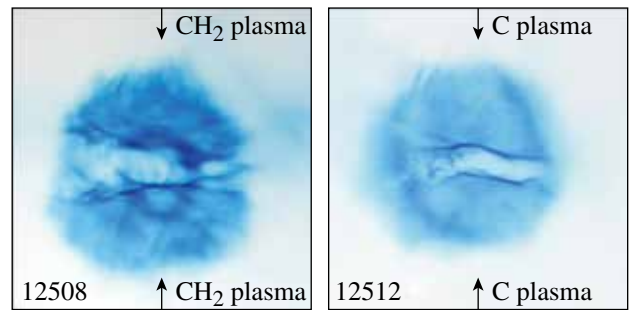
U1292JR

Figure 132.87  
EP-ACSEL experimental setup.

drive targets with 2200 J (per target) in 3 ns. These interpenetrating plasmas were then probed from the side by short-pulse laser-generated protons.

EP-ACSEL-12A confirmed the presence of the large self-organized fields first observed in our FY11 OMEGA EP shots. These surprising structures, formed by a yet unexplained mechanism, are much larger than the intrinsic plasma spatial scales and persist for much longer than the plasma kinetic time scales. Now in press in *Nature Physics*<sup>26</sup> as a cover figure article, this finding provides a new way to understand how electromagnetic order emerges from chaos in the cosmos, such as in the plasma flows that emerge from young stars.

EP-ACSEL-12B explored the sensitivity of these self-organized fields to changes in the laser-drive conditions and target type. Figure 132.88 shows the dramatic difference in the fields that develop in counter-streaming CH<sub>2</sub> flows (a hydrogenated multi-species plasma), and pure C plasmas. The C flows develop much less turbulence. We are currently exploring the origin of these features using basic plasma theories and numeric simulations.



U1516JR

Figure 132.88  
Proton images of the counter-streaming plasmas from the collisionless shock experiments of July 2012.

The results have been presented at many conferences.<sup>56–59</sup> Seven papers<sup>26–28,59–62</sup> have been published and additional papers are in preparation.<sup>63–65</sup>

The ACSEL-12A/B on OMEGA-60 campaigns focused on characterizing plasma conditions in the interaction region of two high-velocity plasma flows. The target geometry is similar to previous ACSEL campaigns with two foil targets separated by 8 mm. The targets are heated with 5 kJ of laser energy per foil, producing high-velocity plasma blowoff. The target material is pure carbon, CH<sub>2</sub>, or beryllium. Thomson scattering is then used to measure the plasma conditions. High-quality data

were obtained, providing plasma parameters that have never before been measured, as seen in Fig. 132.89.

The electron temperature and density are measured from the electron feature; then the ion feature can be used to measure the ion temperature and flow velocity. The ion temperature is shown in Fig. 132.90 for all three target materials. The ion temperatures were similar for the targets containing carbon

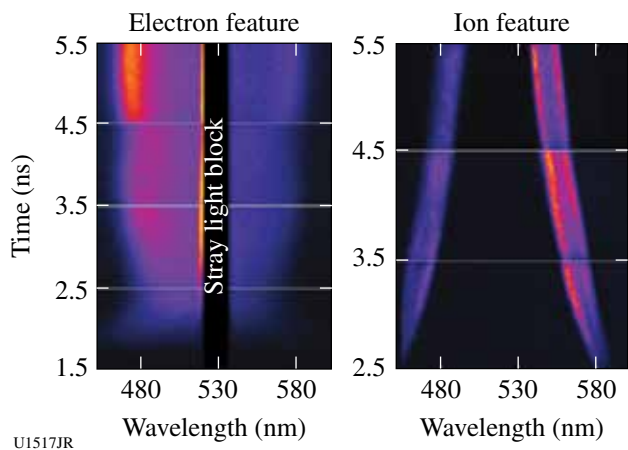


Figure 132.89  
Thomson-scattered light from the plasma is measured on a series of carbon target shots.

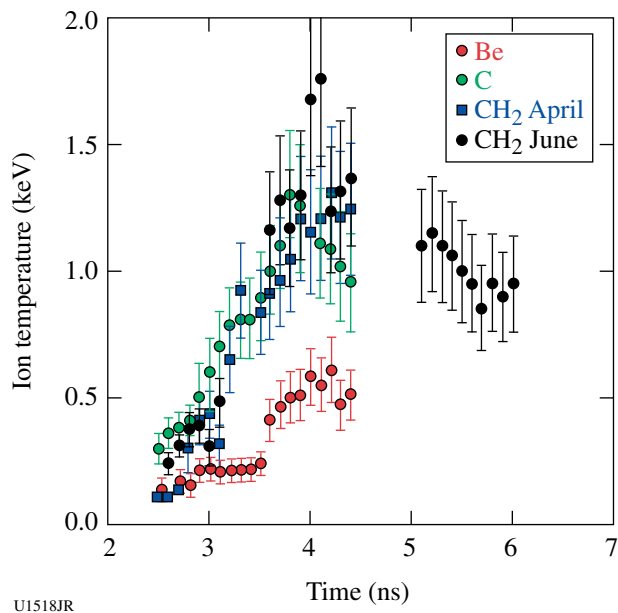


Figure 132.90  
Compilation of ion temperatures of counter-streaming plasmas from different target materials of Be, carbon, and CH<sub>2</sub>. The differences are important to understanding the collisionless shock-creation regime.

and significantly lower for the beryllium target. A detailed understanding of the counter-streaming heating mechanism is currently being developed.

Our work and collaboration produced numerous invited talks and high-profile papers including Nature Physics (cover figure),<sup>26</sup> Physics of Plasmas (highlight research), and Review of Scientific Instruments (invited article).

### ***Dislocations and Twinning at High Pressures and Strain Rate on bcc Metals***

Principal Investigators: B. R. Maddox, A. Comley, and C. Wehrenberg (LLNL)

In TaRDiff-2012 our goal was to study twinning and dislocation motion in shock-compressed tantalum. The experimental configuration used the broadband x-ray diffraction diagnostic on TIM-4 as the primary diagnostic for studying twinning. Alternatively, a recovery tube was fielded on TIM-1, to allow for the study of recovered micro-indented samples. Samples were driven using a 1-ns square pulse with laser energy in the 15- to 65-J range. High-quality diffraction data were obtained and Ta samples were successfully recovered. Initial analysis did not show driven diffraction signal for the (110) Ta samples, which were expected to show larger amounts of twinning. However, high-contrast-driven Laue spots were observed for (100) oriented Ta crystals, and these data were used in Ta strength measurements. Recovered Ta samples will be examined by a transmission electron microscope (TEM) to measure the dislocation motion originating from the micro-indent.

### ***Thermonuclear Reactions in Stellar Plasmas and High-Resolution Measurements of Three-Body Breakup in Isobaric Analogue Reactions***

Principal Investigators: D. P. McNabb (LLNL); R. D. Petrasso (MIT); and T. C. Sangster (LLE)

The starting point for this project was to design a series of direct-drive, exploding-pusher implosions to measure particle production spectra for the  $T(t,2n)^4\text{He}$  fusion reaction. The  $T(t,2n)^4\text{He}$  reaction is important for NIF diagnostics and is the charge-symmetric reaction to  $^3\text{He}(^3\text{He},2p)^4\text{He}$ —a key reaction in the solar proton-proton chain. Our initial goal is to compare these results with those predicted by nuclear theory calculations to gain insight into the reaction mechanism. We will be measuring the neutrons with an improved neutron time-of-flight (nTOF) detector system, with the magnetic recoil spectrometer optimized for lower-energy neutrons and high resolution, and different activation systems. The Thomson parabola ion

energy (TPIE) analyzer has also been optimized to attempt to measure the continuum alpha particle spectrum in addition to the emitted neutrons. Due to difficulties getting capsules filled with high-purity tritium, the shot day was deferred until Q1FY13. There is a renewed interest in these experiments on OMEGA given the recent high-quality TT symcap nTOF data obtained on the NIF and the discrepancy between these neutron spectral measurements and previous experiments. In addition to fielding the TPIE spectrometer, the OMEGA measurements are expected to take place at a higher temperature than the new NIF data.

### Compton Radiography Fast Ignition (CRFI) Campaign

Principal Investigators: P. Patel (LLNL) and H. Sawada (University of California, San Diego)

Co-investigators: C. D. Chen, R. Tommasini, H. S. McLean, and M. H. Key (LLNL); L. C. Jarrott and F. N. Beg (University of California, San Diego); W. Theobald, A. A. Solodov, J. A. Delettrez, V. Yu. Glebov, and C. Stoeckl (LLE); and M. S. Wei and R. B. Stephens (General Atomics)

The goal of the Compton radiography fast ignition (CRFI) campaign is to measure the 2-D areal-density map of an imploded cone-in-shell target using a high-energy bremsstrahlung x-ray backlighter. In cone-guided fast ignition, the formation of a high-density compressed core near the cone tip is critical for efficient fast-electron core heating. The areal density, core shape, and standoff distance from the cone tip provide important parameters for experimentally estimating the energy coupling of an ignition laser to the core. In our joint OMEGA experimental campaign, a 40- $\mu\text{m}$ -thick deuterated carbon (CD) shell was imploded by 54 18-kJ OMEGA beams with a low-adiabat shaped drive pulse. A backlighter target consisting of a 10- $\mu\text{m}$ -diam Au wire embedded on a 300- $\mu\text{m}$   $\times$  300- $\mu\text{m}$  CH foil was irradiated with a 250- to 1500-J, 10-ps OMEGA EP beam in a 100- $\mu\text{m}$  focal spot to produce high-energy bremsstrahlung x rays. The hard x rays with an energy greater than 20 to 30 keV transmitting through CD plasmas were dominated by Compton scattering and the mass attenuation coefficient was weakly sensitive to the plasma density. The bremsstrahlung spectrum and spatial resolution were estimated to be an  $\sim 160$ -keV x-ray slope and 7- $\mu\text{m}$  half width at half maximum (HWHM), respectively, from a radiograph of a 200-mm-diam solid tungsten sphere using 10-ps, 250-J OMEGA EP beam energy. Figure 132.91 shows the radiographic images of an imploded cone-in-shell target at 4.0 ns from the start of the drive pulse with an OMEGA EP energy of 1.5 kJ. Figures 132.91(a) and 132.91(b) show the same image but in different color scales. A preliminary analysis shows a

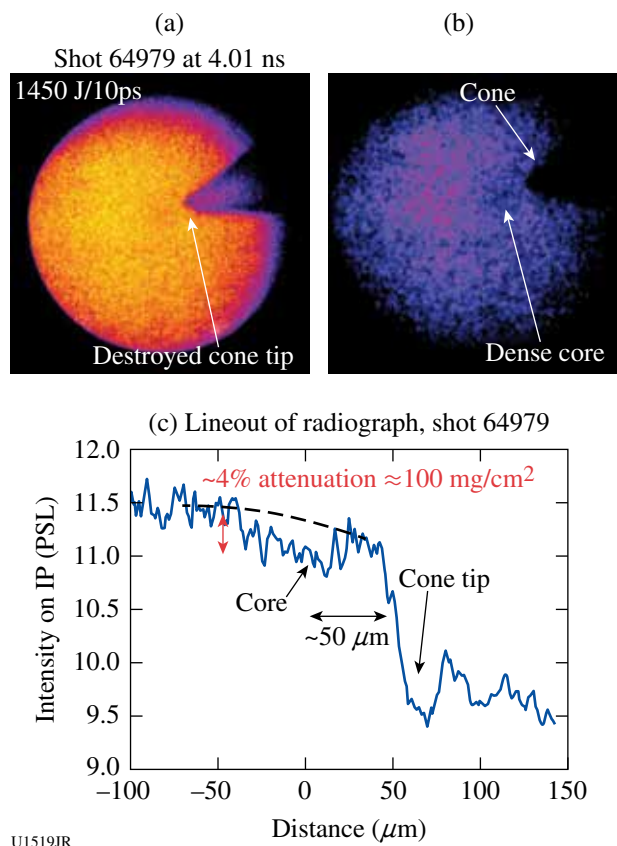


Figure 132.91

[(a) and (b)] Radiographic images of an imploded cone-in-shell target 4.0 ns from the start of the drive pulse. (c) Analysis of images to deduce areal density and standoff distance.

peak areal density of  $\sim 100 \text{ mg/cm}^2$  and a standoff distance of  $\sim 50 \mu\text{m}$  as shown in Fig. 132.91(c). Further analysis is underway to estimate the core size and errors caused by uncertainties in the backlighter spectrum and source size. The inferred areal density from the radiographic images will be compared to a 2-D radiation-hydrodynamic *DRACO* simulation to validate the simulation results.

### Probing Shocked Liquid H, H/He, CH<sub>4</sub>, N<sub>2</sub>, and NH<sub>3</sub> with Inelastic X-Ray Scattering and Shock-Velocity Measurements: Toward the Equation of State of Planetary Interiors

Principal Investigator: S. P. Regan (LLE)

The Fermi-degenerate plasma conditions created in liquid deuterium by a laser-ablation-driven shock wave were probed with noncollective, spectrally resolved, inelastic x-ray Thomson scattering (XRTS) employing Cl Ly $\alpha$  line emission at 2.96 keV (Ref. 66). These first XRTS measurements of the microscopic

properties of shocked deuterium show an inferred spatially averaged electron temperature of  $8 \pm 5$  eV, an electron density of  $2.2 (\pm 0.5) \times 10^{23} \text{ cm}^{-3}$ , and an ionization of  $0.8 (-0.25, +0.15)$ . Two-dimensional hydrodynamic simulations using equation-of-state (EOS) models suited for the extreme parameters occurring in inertial confinement fusion research and planetary interiors are consistent with the experimental results.

The scattered spectrum of the Cl Ly $\alpha$  emission taken at  $t = 5$  ns with a  $250\text{-}\mu\text{m}$  slit in the scattering channel is shown in Fig. 132.92(a). The measurement taken without the slit is shown in Fig. 132.92(b), and the incident spectrum is shown in Fig. 132.92(c). The observed noise in the measured scattered x-ray spectrum is consistent with the estimated signal level. The incident spectrum is measured by irradiating a parylene D foil target on a separate laser shot. The scattered spectrum has a strong Rayleigh peak around 2960 eV and a Compton-downshifted feature. Scattered x-ray spectra were calculated using the x-ray scattering (XRS) code, which uses the finite-temperature random-phase approximation with static local field corrections to obtain the spectral shape of the inelastic (Compton) feature caused by scattering from free electrons.<sup>67</sup> The elastic scattering intensity strongly depends on the degree of ion-ion correlations in the plasma via the structure factor  $S_{ij}$  (Ref. 68). To constrain the value for  $S_{ij}$ , density functional theory molecular dynamics (DFT-MD) simulations were performed using the Vienna *ab initio* simulation package (VASP).<sup>69,70</sup>

The simulations indicate weak ionic correlations for the conditions similar to the average of the plasma probed. This means the ion-ion structure factor  $S_{ij}$  at the relevant scattering wave number is close to unity for most of the conditions probed. With this information, the elastic scattering feature can be used to constrain the temperature and the ionization degree of the system. Structure factors close to unity are also found for the unshocked deuterium liquid. In addition to Doppler broadening, the width and position of the inelastic feature depend on the density for  $\alpha_s \sim 1$ . This fact allows us to bracket the electron density and estimate the ionization charge based on the initial mass density of the sample. The simulated scattering spectra computed using XRS provided the best fit to the spectrum measured with the slit for the following plasma conditions:  $T_e = 8 \pm 5$  eV,  $Z \sim 0.8 (-0.25, +0.15)$ , and  $n_e = 2.2 (\pm 0.5) \times 10^{23} \text{ cm}^{-3}$ . The DRACO simulations are in close agreement with the experimental results. These plasma conditions were repeatable on a subsequent laser shot. The plasma conditions inferred from the spectrally resolved x-ray spectrum recorded without the slit in the x-ray scattering channel are lower with  $T_e = 3 \pm 2$  eV,  $Z \sim 0.6 \pm 0.2$ , and  $n_e = 2.0 (\pm 0.5) \times 10^{23} \text{ cm}^{-3}$ . The lower plasma pressure created by the lower-intensity portion of the laser drive causes bowing of the shock front (see Fig. 131.7 in Ref. 66). When the slit is placed in the scattering channel, the x rays scattered from this under-driven portion of the target are blocked from the detector. This leads to higher inferred values of  $T_e$ ,  $Z$ , and  $n_e$ , which is more representative of the uniformly shocked region.

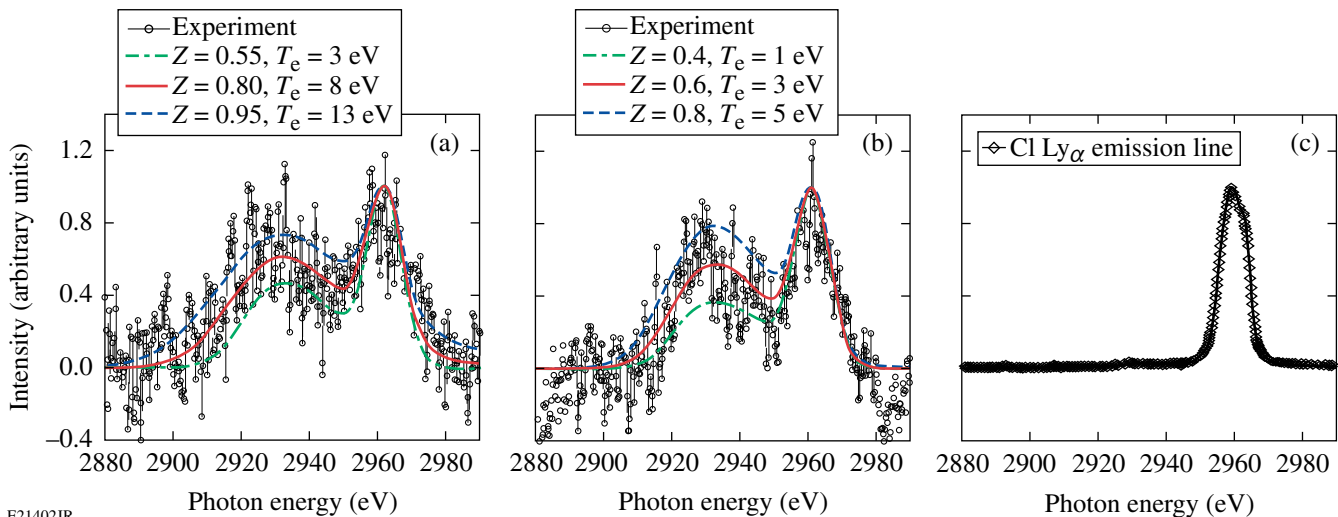


Figure 132.92

Measurement of (a) Cl Ly $\alpha$  emission scattered from shocked liquid deuterium with a  $250\text{-}\mu\text{m}$  slit in the scattering channel and simulated scattering spectra, (b) Cl Ly $\alpha$  emission scattered from shocked liquid deuterium without a  $250\text{-}\mu\text{m}$  slit in the scattering channel and simulated scattering spectra, (c) Cl Ly $\alpha$  emission incident on the shocked liquid deuterium. The inferred plasma conditions in (a) are  $T_e = 8 \pm 5$  eV,  $Z \sim 0.8 (-0.25, +0.15)$ , and  $n_e = 2.2 (\pm 0.5) \times 10^{23} \text{ cm}^{-3}$  and in (b) are  $T_e = 3 \pm 2$  eV,  $Z \sim 0.6 \pm 0.2$ , and  $n_e = 2.0 (\pm 0.5) \times 10^{23} \text{ cm}^{-3}$ .

Unlike previous velocity spectrometer for any reflector (VISAR) measurements, the x-ray scattering experimental platform offers the considerable advantage of probing off-Hugoniot states. This experimental result is a significant step toward achieving accurate measurements of all thermodynamic variables needed to provide stringent tests of EOS models, which would require at least three thermodynamic variables like pressure, mass density, and temperature.

**Extreme Chemistry of Precompressed Nitrogen**

Principal Investigator: J. R. Rygg (LLNL)

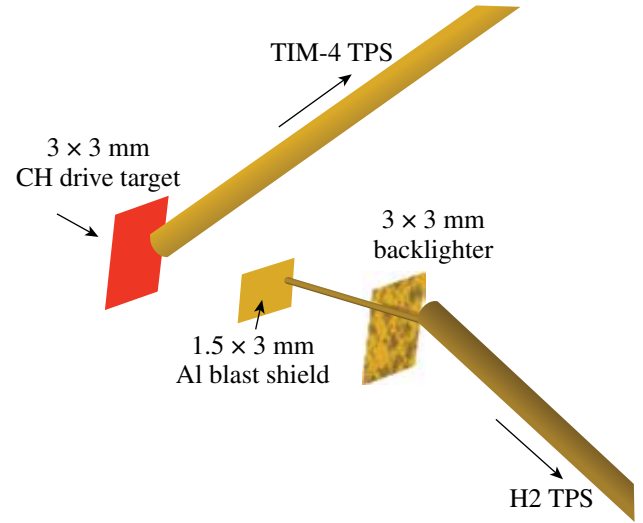
Experimental measurement of the N<sub>2</sub> Hugoniot was extended to 850 GPa by launching shocks into N<sub>2</sub> samples pre-compressed in diamond anvil cells to ~2 GPa (see Fig. 132.93). VISAR and streaked optical pyrometry (SOP) measurements of the N<sub>2</sub> shock front in comparison to concomitant measurements in quartz were used to infer pressure, density, reflectance, and temperature of shocked N<sub>2</sub>. Compressibility, optical reflectivity, and temperature measurements show that N<sub>2</sub> undergoes a complex dissociation–polymerization transition, in good agreement with first principle calculations.

**Measurements of the Ablative Richtmyer–Meshkov Instability in the Nonlinear Regime**

Principal Investigator: V. A. Smalyuk (LLNL)

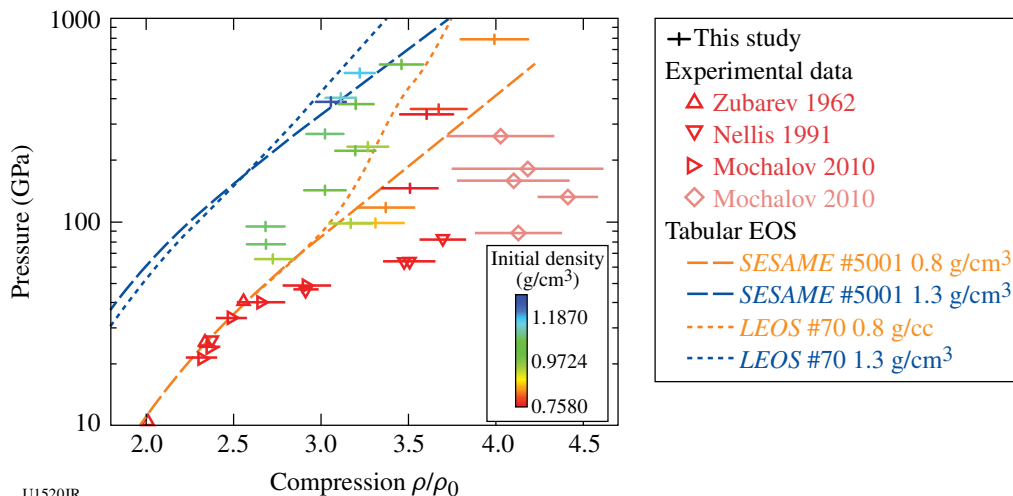
Figure 132.94 shows a schematic of the experimental setup for the nonlinear Richtmyer–Meshkov (RM) instability experi-

ments on OMEGA. Planar CH targets (15, 30, and 50 μm thick) were driven with three UV beams using a 6-ns square pulse shape, a total energy of ~0.7 kJ, and a laser intensity of ~5 × 10<sup>13</sup> W/cm<sup>2</sup>. Initial target modulations were imposed by laser imprinting using a beam with a special 2-D phase plate with a modulation wavelength of ~70 μm. The timing of this beam was advanced by ~200 ps, relative to other drive beams that have regular SG4 distributed phase plates (DPP's). Figure 132.95 shows laser-beam images with an SG4 DPP [Fig. 132.95(a)] and a special 2-D DPP [Fig. 132.95(b)]. Growth of target modu-



U1521JR

Figure 132.94  
Experimental setup.



U1520JR

Figure 132.93

In FY12, the OMEGA laser was used to extend the N<sub>2</sub> Hugoniot from 100 to 850 GPa (crosses). The N<sub>2</sub> shock pressure and density were inferred by shock-velocity measurements impedance matched to a quartz standard.

lations was measured with x-ray radiography using uranium (~1.3-keV), samarium (~1.8-keV), and tantalum (~2.2-keV) backlighters on a framing camera with 10- $\mu\text{m}$  spatial resolution and 80-ps temporal resolution. The backlighter targets were driven with a 2-ns square pulse shape and an intensity of  $\sim 3 \times 10^{14}$  W/cm<sup>2</sup> using seven additional UV beams. Figure 132.96 shows an example of a measured image at 1.1 ns (near the end of the RM phase) taken with a 50- $\mu\text{m}$ -thick CH foil and tantalum backlighter. Evolution of 2-D broadband modulations was observed in the RM phase for all target types during a shock transit time before the onset of acceleration and subsequent RT growth. Figure 132.97 summarizes the areal-density

evolution of 2-D modulation at a wavelength of 70  $\mu\text{m}$  for the 30- and 50- $\mu\text{m}$ -thick foils and compares data with predictions of the 2-D hydrocode *DRACO*. The vertical dashed lines show expected times of the end of the RM phase and the beginning of the RT phase for these types of foils. Blue data points and curves correspond to 30- $\mu\text{m}$ -thick foils, while black curves and data points correspond to 50- $\mu\text{m}$ -thick foils. Areal-density modulations grow throughout the RM phase, and their evolution is similar to code predictions, validating the simulations.

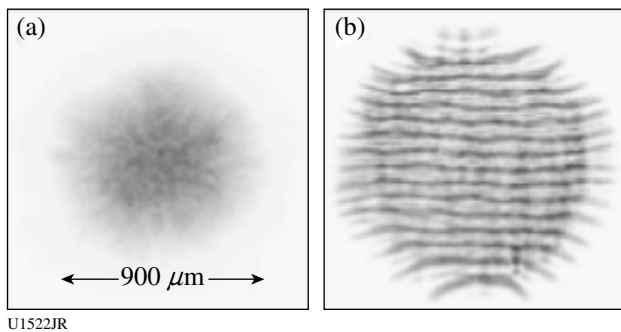


Figure 132.95  
Laser-beam images with (a) regular SG4 DPP and (b) special 2-D DPP.

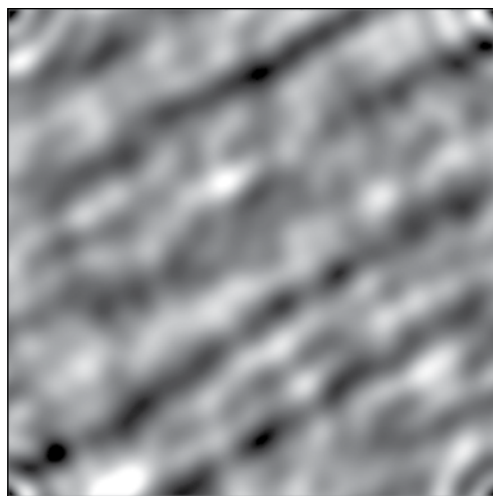


Figure 132.96  
X-ray images of 2-D broadband modulations near the end the Richtmyer-Meshkov instability growth phase measured in 50- $\mu\text{m}$ -thick CH targets.

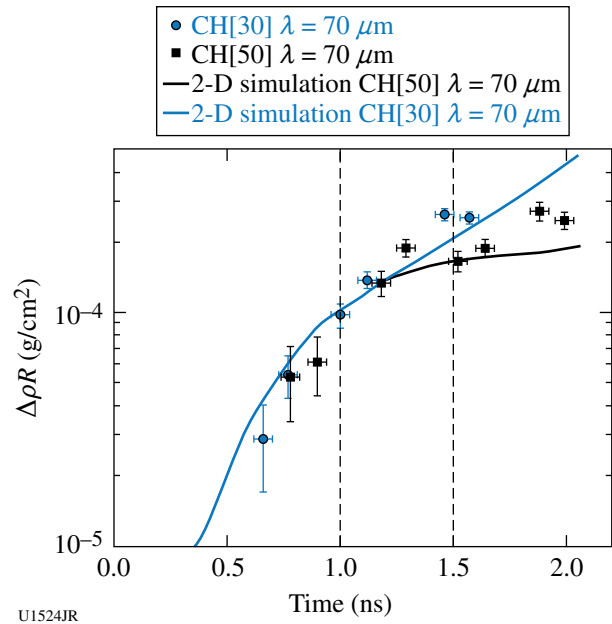


Figure 132.97  
Evolution of 2-D areal-density modulations at a wavelength of 70  $\mu\text{m}$  measured in 30- $\mu\text{m}$ -thick foils (blue circles) and in 50- $\mu\text{m}$ -thick foils (black squares). Solid curves correspond to 2-D *DRACO* simulations, while vertical dashed lines correspond to times of the end of the RM phase and beginning of the RT phase in 30- $\mu\text{m}$ -thick foils (blue curves) and 50- $\mu\text{m}$ -thick foils (black curves).

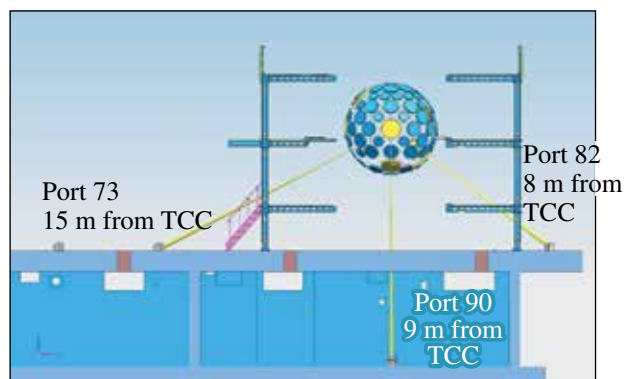
### ***Spectroscopy of Neutrons Generated Through Nuclear Reactions with Light Ions in Short-Pulse Laser Interaction Experiments***

Principal Investigators: C. Stoeckl, V. Yu. Glebov, and T. C. Sangster (LLE)

The experimental objective of this project is to study nuclear reactions in light ions by measuring the spectrum of neutrons generated in short-pulse laser interaction experiments and compare them with simulated spectra based on the published cross sections.

Planar targets are irradiated with one short-pulse beam focused at the target's front surface. Charged particles from the back side of the target create neutrons and charged particles through nuclear reactions in a second converter target placed closely behind the primary interaction target. The spectrum of the neutrons generated in the converter target is measured using a scintillator/photomultiplier-based neutron time-of-flight (nTOF) detector. Charged-particle detectors are used to measure the spectra of the primary particles.

In FY12 three new nTOF detectors were installed on OMEGA EP (see Fig. 132.98). One in the laser forward direction on port 82, one at 90° to the laser on port 90, and one in the laser backward direction on port 73. Each of these detectors is heavily shielded with lead and gated to suppress the signal from the prompt hard x rays generated in the laser-plasma interaction processes on the primary target.

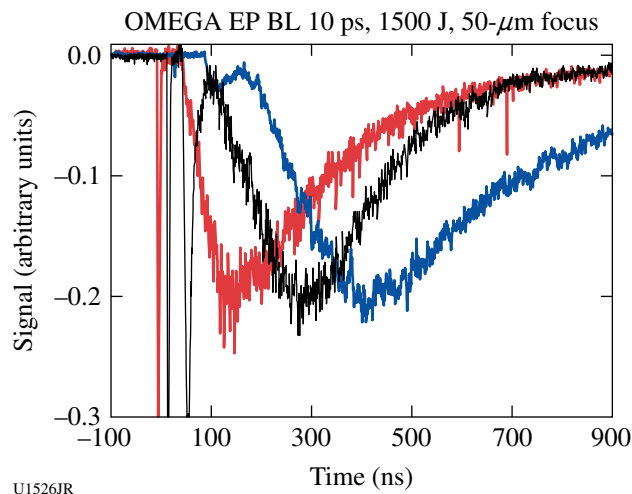


U1525JR

Figure 132.98  
Location map of the three neutron detectors installed in FY12.

In FY12 one shot day (19 September) was available for experiments. Copper foils were used as primary targets to generate protons and irradiated with 10- and 100-ps OMEGA EP pulses and energies of up to 2.0 kJ. A container target was developed to place ~100 mg of LiD inside a stainless-steel container ~2.5 cm behind the primary target. High-quality nTOF spectra were recorded on all detectors for all shots during the day. Figure 132.99 shows data from all three detectors.

No specific spectral features like DT fusion neutrons are visible in the recorded data. The analysis of this data is ongoing. The current working hypothesis is that the measured neutron spectrum is dominated by p-n reactions in the LiD container and the target chamber. Efforts to reduce this background are currently under consideration.



U1526JR

Figure 132.99  
Neutron time-of-flight data from the detectors in ports 82 (red), 90 (black), and 73 (blue). The first peak in the data corresponds to the arrival of the prompt hard x rays. Gating suppresses this peak by at least five orders of magnitude.

### Integrated Fast-Ignition Experiments

Principal Investigators: W. Theobald  
and A. A. Solodov (LLE)

Co-investigators: C. Stoeckl, R. Epstein, V. Yu. Glebov, G. Fiksel, S. Ivancic, F. J. Marshall, G. McKiernan, C. Mileham, P. M. Nilson, and T. C. Sangster (LLE); L. C. Jarrott and F. N. Beg (University of California, San Diego); E. Giraldez, R. B. Stephens, and M. S. Wei (General Atomics); H. McLean (LLNL); H. Sawada (University of Nevada, Reno); H. Habara (ILE); and J. J. Santos (CELIA)

Integrated fast-ignition experiments with cone-in-shell targets on OMEGA have demonstrated ~3.5% coupling efficiency of short-pulse laser energy into a compressed target.<sup>71</sup> The goals of this Laboratory Basic Science (LBS) proposal were to study the short-pulse laser/fast-electron coupling efficiency using an improved OMEGA EP laser and to validate the 2-D radiation-hydrodynamic modeling predictions of a new aluminum cone-tip target design with a backlighter experiment. The new target design has been modeled with detailed hydrodynamic simulations. Figure 132.100 shows a *DRACO*<sup>72</sup> simulation of the cone-in-shell target with an aluminum block mounted in front of a gold cone for different times during the implosion. This design is more resilient against the strong shock from the implosion than a previous design with a gold-only cone.<sup>71</sup> Shock breakout is predicted to be delayed by ~80 ps in the new target design. Figure 132.100(c) shows that the interior of the cone volume is free of plasma up to the time when the shock breaks through. A new backlighter platform has been developed

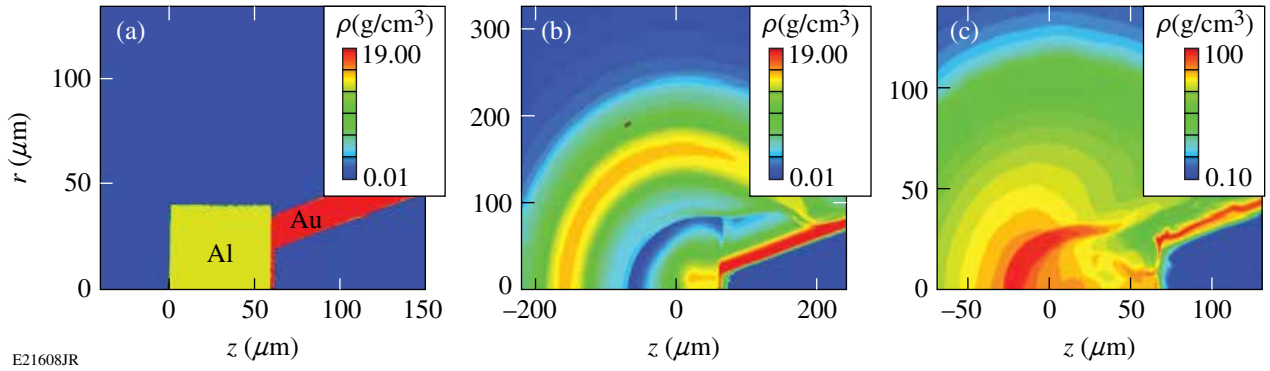


Figure 132.100

Two-dimensional hydrodynamic *DRACO*<sup>72</sup> simulation of a new cone-in-shell target design. (a) Detail of the target tip showing the gold cone with an aluminum tip. (b) Imploding shell before peak compression at 3.25 ns. Simulations predict thermal expansion of the cone material due to radiation preheat. The aluminum tip expands faster than the gold material. (c) Density map at 3.87 ns ( $\sim 0.19$  ns before peak compression) showing better shock resilience of this design than the previous<sup>71</sup> Au cone tip target.

and was tested during the first shot day in FY12 to characterize the fuel assembly of cone-in-shell targets close to peak compression and to validate the 2-D radiation-hydrodynamic modeling predictions. This was done with flash radiography<sup>73</sup> using a monochromatic 8.05-keV x-ray source that radiographed the target that was imploded by 54 OMEGA beams. A thin Cu foil was irradiated by the 1.5-kJ, 10-ps OMEGA EP short-pulse laser and generated a bright Cu  $K_\alpha$  backlighter source. The laser was defocused to an  $\sim 20$ - $\mu\text{m}$  spot that provided an intensity of  $\sim 5 \times 10^{17}$  W/cm<sup>2</sup>. The fast electrons refluxed in the Cu foil and generated  $K_\alpha$  radiation over the  $\sim 1$ -mm foil, which provided an ideal area backlighter source. A spherical Bragg crystal located on the opposite side of the target imaged the implosions onto an image plate detector.<sup>74</sup> Figure 132.101 shows measured images of the implosion at various times around peak compression over a time range of  $\sim 0.4$  ns and over a region of  $500 \mu\text{m} \times 500 \mu\text{m}$ . Note that each image was taken with a different shot. Figure 132.101(a) shows an image of an undriven target, where the Al tip is clearly visible and less opaque than the gold cone. The false color scheme represents the measured optical density. The frame in Fig. 132.101(b) shows an implosion at 3.75 ns after the start of the drive pulse. The fuel starts to assemble in front of the tip and the Al tip is compressed in the radial and longitudinal directions to a higher density. The following frames were taken at successively later times: Fig. 132.101(c) at 3.82 ns, Fig. 132.101(d) at 3.93 ns, Fig. 132.101(e) at 4.05 ns, and Fig. 132.101(f) at 4.15 ns. At later times the Al tip is more deformed and eventually completely destroyed and the fuel assembly reaches higher density. The radiographs show how the implosion destroys and pushes back the cone tip. Peak compression was reached close to the time of the frame in Fig. 132.101(e), while the last frame was

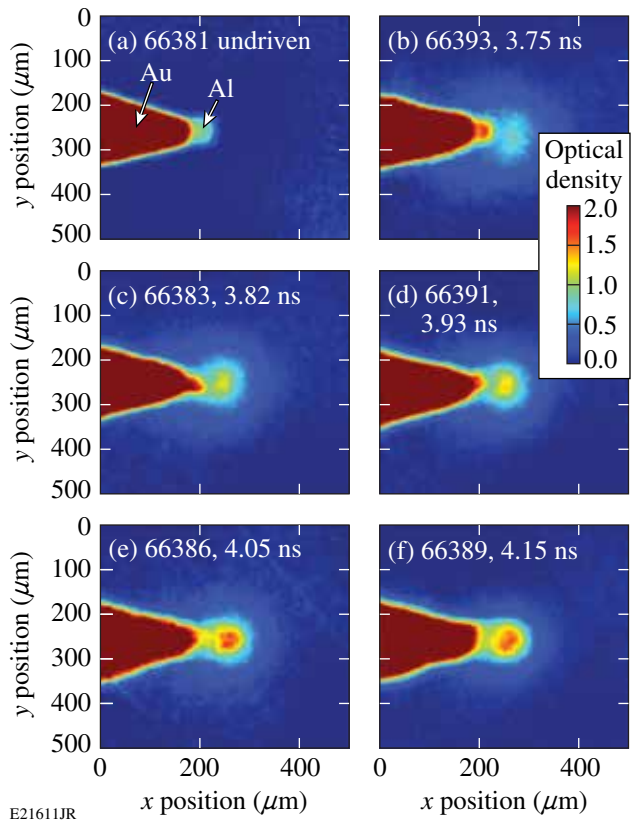


Figure 132.101

(a) Radiography images of an undriven target and imploded cone-in-shell targets at various stages of the implosion: (b) 3.75 ns, (c) 3.82 ns, (d) 3.93 ns, (e) 4.05 ns, and (f) 4.15 ns after the start of the UV drive laser pulse.

after peak compression. The measured time of peak compression ( $\sim 4.10 \pm 0.05$  ns) compares well to the time (4.06 ns) predicted from 2-D *DRACO* simulations. The measured peak

areal density is  $330 \pm 50 \text{ mg/cm}^3$  using a calculated average mass absorption coefficient from the *DRACO* simulation along the line of sight. The predicted peak value of  $360 \text{ mg/cm}^3$  shows that the measured value is close to the 2-D prediction. Interleaved with joint shots, the shock-breakout measurements were performed with OMEGA-only beams. The measured shock-breakout time agrees with the predicted breakout time within  $\sim 60 \text{ ps}$ . The experiments confirm the improved shock resilience of the target. The second shot day at the end of FY12 studied the fast-electron coupling of the new target. The OMEGA EP laser was significantly improved with a smaller focus ( $R_{80} = 15 \text{ }\mu\text{m}$ ), a higher energy (1.35 kJ), and a higher contrast ( $\sim 0.5\text{-mJ}$  prepulse energy). Compared to the previous experiment,<sup>71</sup> the average intensity increased about four times to  $\sim 2 \times 10^{19} \text{ W/cm}^2$ . The laser contrast was sufficiently high so that no significant pre-plasma formation is expected. The data of the integrated experiment are still being analyzed.

### FY12 LLNL OMEGA Experimental Programs

In FY12, LLNL conducted several campaigns on the OMEGA and OMEGA EP lasers, as well as campaigns that jointly used the OMEGA and OMEGA EP beams. Overall, LLNL led 335 target shots involving OMEGA and 121 target shots involving OMEGA EP. Approximately 38% of the total number of shots (124 OMEGA shots and 39 OMEGA EP shots) supported the National Ignition Campaign (NIC). The remaining 211 OMEGA shots and 82 OMEGA EP shots were dedicated to experiments for high-energy-density (HED) physics.

### National Ignition Campaign Experiments

#### *Thermal Conductivity Study of CH/Be and CH/D<sub>2</sub> Interfaces by Refraction-Enhanced X-Ray Radiography*

Principal Investigator: Y. Ping

Co-investigators: O. L. Landen, J. A. Koch, R. Wallace, and G. W. Collins

The Atwood#12A&B campaigns are based on the technique of time-resolved, refraction-enhanced x-ray radiography that was successfully demonstrated in FY11. The evolution of the density profile at a cylindrical CH/Be interface isochorically heated by Ag L-band radiation has been measured to infer the thermal conductivity under inertial confinement fusion (ICF)-relevant conditions. In addition to observing the density evolution caused by thermal conduction, a counter-propagating shock wave and rarefaction wave were also observed as shown in Fig. 132.102. The velocities of these waves were measured simultaneously, providing constraints on the temperature after heating. Preliminary analysis of the data and hydrodynamic

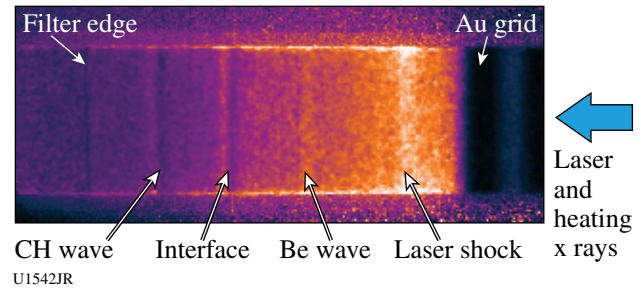


Figure 132.102

A radiograph of the heated CH/Be target. The delay between the heater and the backlighter was 5 ns. The laser beams and heating x rays were incident from the right side. Three fringes show up in the image: the middle fringe representing the interface and two side fringes corresponding to the waves propagating in CH and Be, respectively. The shock driven by the laser, traveling from right to left, is also visible.

simulations shows that the thermal conductivity is higher than most models predict. The measurements of the CH/D<sub>2</sub> interface in cryogenic targets were complicated by leaking in the cryo cells, limited rotation movement, and condensation on the backlighter, which significantly reduced the brightness. A list of potential improvements has been provided to LLE for future experiments with cryogenic targets.

#### *High-Resolution Measurements of Velocity Nonuniformities Created by Microscopic Perturbations in NIF Ablator Materials*

Principal Investigator: P. M. Celliers

Co-investigator: M. A. Barrios

In May 2012, a full day was dedicated to the CAPSEED campaign. This campaign is a continuation of earlier campaigns that studied the performance of National Ignition Facility (NIF) ablaters. The latest capsule designs using glow-discharge-polymer (GDP) ablaters for the NIC currently employ Si doping layers as preheat shielding for the fuel; the earlier NIC designs employed Ge-doping layers. In response to this design change, most of the CAPSEED-12A campaign was devoted to assessing the performance of the newer Si-doped design (as compared to the previous Ge-doped designs). Results from this campaign (see Fig. 132.103) show that the performance of the Si-doped material matches that of the Ge-doped material.

Three additional shots were devoted to studying double-shocked nanocrystalline diamond [or “high-density carbon” (HDC)]. In current capsule designs employing diamond ablaters, the initial shock strength is sufficient to only partially melt the capsule. Shock strengths much higher than this will set the fuel adiabat higher than the design goal of current designs.

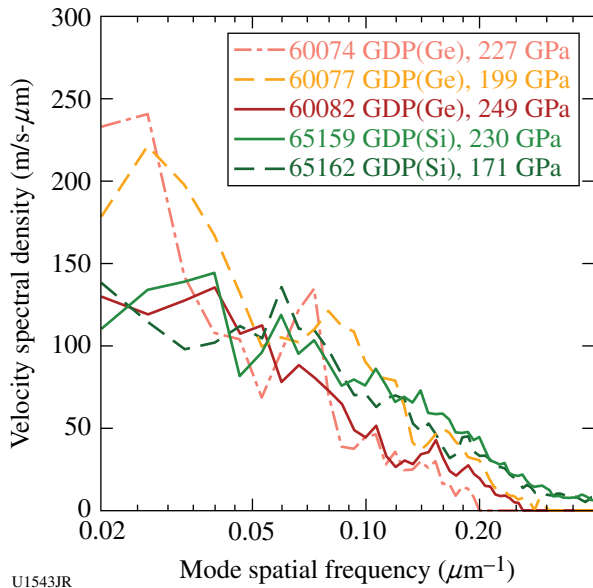


Figure 132.103  
Velocity-fluctuation spectra measured for Ge-doped GDP in 2011 (shots 60074, 60077, and 60082) and Si-doped GDP in 2012 (shots 65159 and 65162). The velocity spectra for all cases appear to be equivalent within the range of statistical fluctuations.

Velocity fluctuations on the first (leading) shock are known to diminish significantly when the shock melting starts. The purpose of the double-shock test is to see whether the second and third shocks that follow in the compression sequence accumulate further velocity fluctuations, owing to the mixed-phase state of the diamond ablator following passage of the first shock. An initial double-shock test performed during the CAPSEED-12A campaign suggests (Fig. 132.104) that subsequent shocks appear to have similar fluctuation levels as the initial shock. Further tests are needed to extend the data set.

**Measuring the Adiabatic Index of Polystyrene Using Counter-Propagating Shocks and X-Ray Thomson Scattering**

Principal Investigator: A. Pak  
Co-investigators: T. Ma, L. Fletcher, T. Döppner, and S. H. Glenzer

The adiabatic index of a material  $\gamma$  is an important quantity in determining a material's equation of state (EOS), which describes the response in density and temperature of a material to a change in pressure (such as that created by a strong shock). Understanding the EOS of polystyrene, a material similar to the NIF ablator, at high densities ( $>4\times$  solid) and at temperatures of several eV, is of interest since it may inform the design and performance of current implosion experiments.

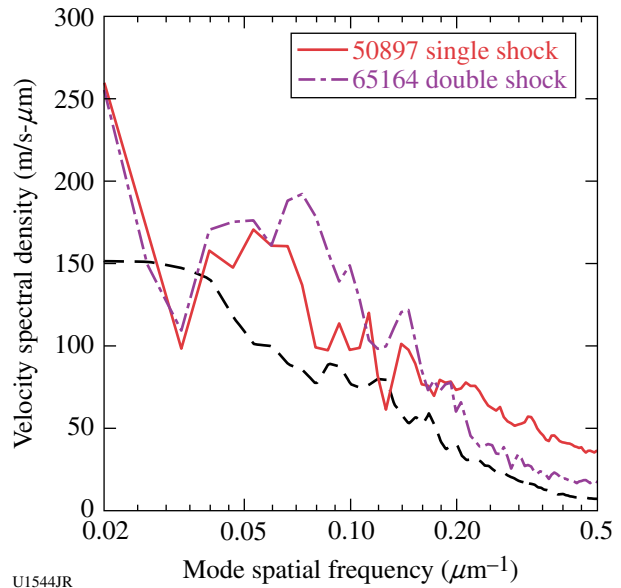
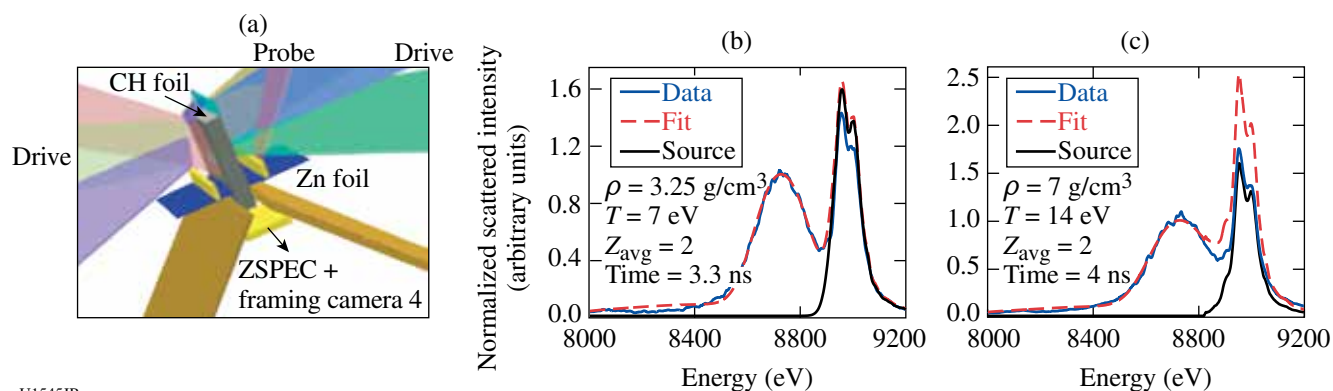


Figure 132.104  
Velocity-fluctuation spectra measured for single-shocked and double-shocked HDC ablators. The black dashed curve represents the noise floor of the measurement (which is higher than for the measurements in Fig. 132.103). The fluctuation levels behind the second shock appear comparable to those behind the first shock.

In the CH-HeatCap campaign on OMEGA, the electron density, temperature, and charge state of shocked polystyrene (CH) were directly measured with x-ray Thomson scattering (XRTS). Using the Hugoniot relationships for a single strong shock,  $\gamma$  can be experimentally determined by measuring the mass density of the shocked material. Additionally, the use of colliding shocks in this experiment allowed for  $\gamma$  to be measured at higher mass densities and temperatures than could be obtained using a single shock.

Figure 132.105(a) shows the experimental setup, in which six drive beams on each side drove counter-propagating shock waves into an initially 200- $\mu\text{m}$ -thick polystyrene foil. The drive beams were each 1 ns long and delayed with respect to one another to create an  $\sim 3$ -ns-long pulse with an 800- $\mu\text{m}$  spot diameter at an intensity of  $\sim 1 \times 10^{14}$  W/cm<sup>2</sup>. An additional eight co-timed laser beams with a 1-ns pulse width and a focused intensity of  $\sim 1 \times 10^{15}$  W/cm<sup>2</sup> created a probe of zinc He $_{\alpha}$  x rays. The x rays scattered through the shocked CH and to the ZSPEC crystal spectrometer onto the framing-camera detector. The timing of the probe with respect to the drive was varied to probe the CH before, during, and after shock collision.

Figures 132.105(b) and 132.105(c) show the scattering spectrum at two different times: just before and after shock collision,



U1545JR

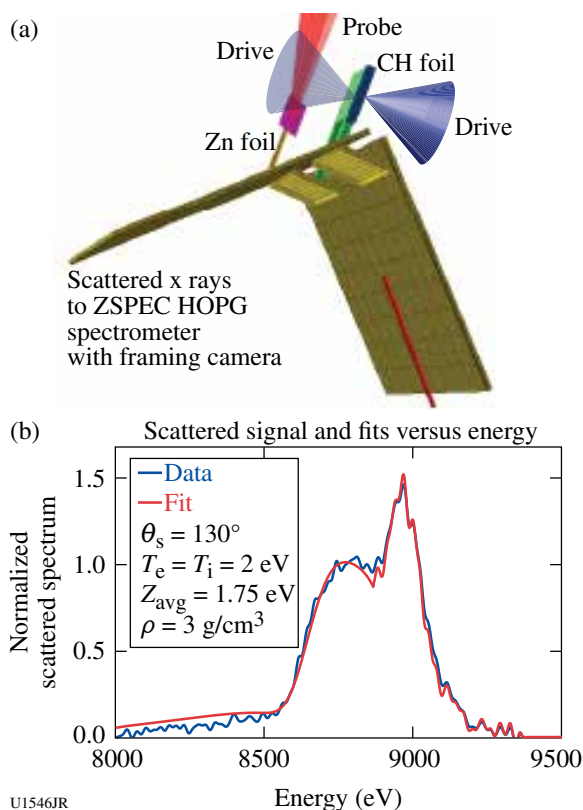
Figure 132.105

(a) Experimental setup. Two drive bundles compress the CH foil, while a probe bundle creates a burst of Zn He $\alpha$  x rays that scatter through the target. Scattered x rays are collected via ZSPEC onto a framing camera detector in TIM-3. The normalized source and scattered x-ray intensity versus energy are shown (b) before and (c) after shock collision, respectively.

respectively. An increase in the width of the lower-energy, downshifted Compton feature indicates an increase in the material's electron density. Initial fits of the data indicate that a single shock density of  $3.25 \pm 0.5$  g/cm $^3$  and a  $7 \pm 0.5$  g/cm $^3$  density after shock collision have been reached. From this preliminary data analysis, the  $\gamma$  measured at the single- and double-shock density is 1.7 to 2.1 and 1.57 to 2.36, respectively. Additional data analysis is in progress.

In a second set of experiments, this time using OMEGA EP, a new experimental platform was developed to pursue similar physics. This year a total of four shot days in the BeXRTS and CH HeatCap campaigns were spent developing an experimental platform utilizing counter-propagating shocks and XRTS on OMEGA EP. One unique property of this class of experiments is that they allow for the adiabatic index  $\gamma$  of warm dense matter (WDM) to be directly measured. Additionally, counter-propagating shocks allow for materials to be compressed to higher densities and temperatures than single-shock experiments can create. A direct measurement of the  $\gamma$  of a material at densities and temperatures relevant to conditions existing in the ablator of NIF implosion experiments will contribute to the understanding, selection, and performance in ablator materials.

The experimental setup is shown in Fig. 132.106(a). In these preliminary experiments, a  $200 \times 1000 \times 1400$ - $\mu$ m polystyrene (CH) foil was driven symmetrically from two sides by separate laser beams. Each drive beam had an  $\sim 351$ -nm wavelength, a 4-ns temporal width, and an average on-target intensity of  $\sim 1 \times 10^{13}$  W/cm $^2$ . Strong shocks, one from each of the two drive beams, counter-propagate with respect to one another and collide at the center of the CH foil. Two additional 1-ns-long UV laser beams are focused onto a zinc foil to create an



U1546JR

Figure 132.106

(a) The experimental setup for the XRTS OMEGA EP colliding-shock campaign. The CH foil is driven from the top and bottom by separate 4-ns-long UV laser beams with  $I_0 \sim 1 \times 10^{13}$  W/cm $^2$ . The counter-propagating shocks are diagnosed using Zn He $\alpha$  x rays created from one or two probe UV laser beams. The scattered x rays travel through a target aperture to the ZSPEC highly oriented pyrolytic graphite (HOPG) crystal spectrometer and onto a framing camera. (b) An example of the measured scattered x-ray signal plotted versus energy taken 4.5 ns from the start of the laser drive. The fit of the scattered signal (red line) indicates that  $\rho = 3$  g/cm $^3$ ,  $T = 2$  eV, and  $Z_{\text{avg}} = 1.75$  eV.

x-ray probe pulse. The Zn He $_{\alpha}$  x rays scatter from the shock-compressed CH foil through a gold aperture in the bottom of the target to the HOPG ZSPEC crystal spectrometer and onto a framing-camera detector that records the scattering signal over  $\sim 500$  ps. Figure 132.106(b) shows an XRTS spectrum obtained at 4.5 ns after the laser drive had begun. The initial fit is in good agreement with predicted values for the density, temperature, and charge state from 2-D HYDRA simulations at this time. Additional analysis of the data is ongoing at this time.

### Ablator Opacity Measurements

Principal Investigator: R. F. Heeter

Co-investigators: A. Graf, G. V. Brown, C. Mauche, R. E. Marrs, and B. Wilson

A new effort was initiated in FY12 to validate models of x-ray absorption and re-emission of capsule ablator materials, including germanium, silicon, and glow-discharge-polymer (GDP) plastic, over x-ray energies and material conditions typical of inertial confinement ablation plasmas. Experiments were undertaken using two platforms: First, the high-energy-density (HED) hohlraum-based opacity platform on OMEGA was used to assess the transmission opacity of Si, Ge, and GDP samples in LTE (local thermodynamic equilibrium) at  $T = 100$  eV at densities around  $0.03$  g/cm $^3$ . The second platform was launched in FY12 on OMEGA EP using dual short-pulse backlighters to measure the x-ray transmission of buried silicon layers embedded in plastic samples. This newer OMEGA EP technique is able to achieve both higher densities and higher temperatures than the OMEGA technique, but it requires tuning to achieve uniform sample conditions.

Sample data from the initial OMEGA experiments are shown in Fig. 132.107. For both Si and Ge samples, the transmission data for the spectral band from 250 to 1500 eV came in below the expected transmission calculated with standard opacity models using the plasma conditions predicted by 2-D radiation-hydrodynamic simulations. These plastic-tamped samples appear to be cooler and denser than expected, indicating either slower ablation and heating than predicted or a substantial error in the opacity models.

In late FY12, a series of follow-up shots were completed, including a tuned-up target design and independent characterization of the plasma conditions. Those data are currently being analyzed. Additional platform improvements, focused on reducing the noise in the transmission measurements, were implemented for beryllium-tamped, Si-doped GDP (plastic) opacity shots taken in early FY13.

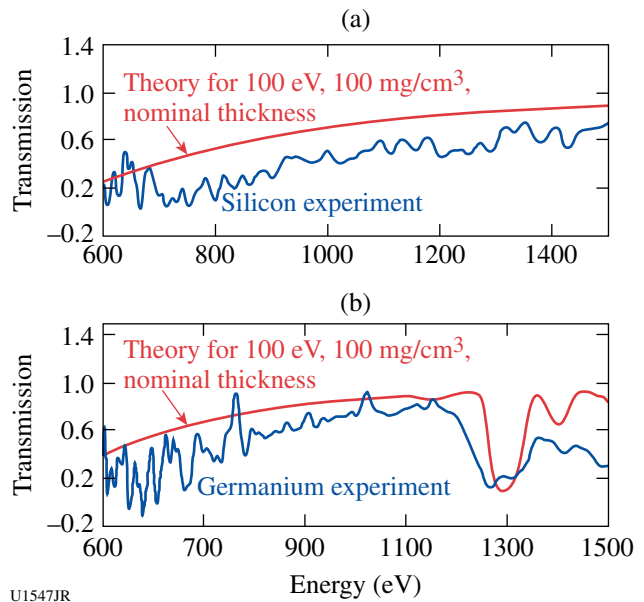


Figure 132.107

Initial results from (a) silicon and (b) germanium transmission experiments on OMEGA with comparison to expected transmissions.

Meanwhile, success was also achieved in obtaining dual-axis transmission spectra for silicon samples. In this new platform, up to two of the OMEGA EP UV beams are used to heat a CH-tamped Si foil with up to 200 J delivered in a Gaussian pulse shape with 100-ps FWHM (full-width-at-half-maximum). Peak sample temperatures of up to 400 eV are inferred from the time-integrated emission spectra of the embedded Si foil. Shortly after the UV heating pulse, a 10-ps IR laser drives a Zn wire backlighter, producing a bright continuum x-ray source with 16-ps FWHM duration and roughly  $20\text{-}\mu\text{m}$  source size. This backlighter probes the expanding silicon plasma edge-on, measuring the sample expansion to yield the plasma density, and measuring the ionization state via absorption spectroscopy to provide information on the sample temperature. A second 10-ps continuum backlighter, synchronized to within 30 ps of the first, probes the sample face-on, delivering precise transmission spectral data for the measured temperature and density. Initial transmission measurements were completed in FY12 and are now being compared with theory.

Furthermore, by choosing a relatively thin tamper layer thickness, it is possible to tailor nonuniform density profiles and study the density of specific charge states as a function of position in an expanding ablated plasma. A sample of the latter data is shown in Fig. 132.108. In this case, 100 J of UV laser energy, arriving from the upper side of the image, heated the sample for 100 ps. The image was recorded roughly 400 ps

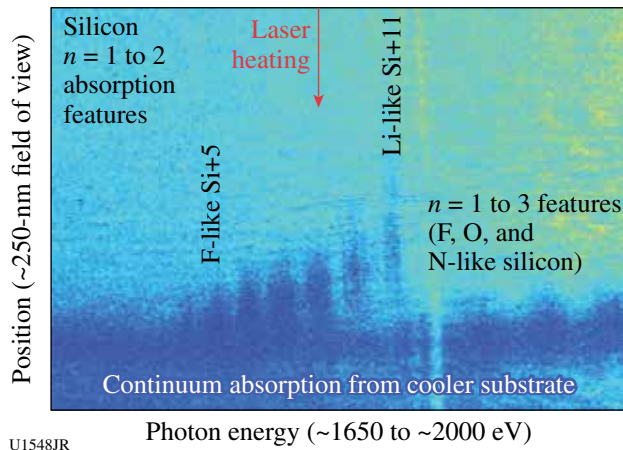


Figure 132.108  
Space-resolved absorption spectrum obtained on OMEGA EP using edge-on broadband radiography of a silicon foil deposited on a carbon substrate and overcoated with a thin CH tamper layer.

after peak drive, during the cooling of the silicon plasma. The  $n = 1$  to 2 absorption features of multiple ionization states of silicon are visible on the left (lower-energy) side of the spectrum, with additional  $n = 1$  to  $n = 3$  features on the right (higher-energy) side. The data show that 400 ps after peak sample drive, lithium-like Si persists on the low-density, laser-heated side of the plasma, while the various charge states of L-shell ions (Be- through F-like) are observed deeper into the plasma at higher density. The typical density at the location of the L-shell features is about  $0.1 \text{ g/cm}^3$ . The laser appears to not have fully heated the carbon substrate and perhaps some of the silicon, so continuum absorption from the rear of the sample is also visible. This technique is now being applied to study x-ray-ablated, silicon-doped GDP ablator plasmas in FY13.

**Multipump Stimulated Raman Scattering**  
Principal Investigator: R. Kirkwood

The second campaign in this series was carried out to investigate the cooperative interaction of multiple beams in a cone to drive stimulated Raman scattering (SRS). The experiments used exploding-CH foil targets preheated by 11 heater beams to create a symmetric density profile. A normally incident seed beam was focused on the back side of the foil where it could produce SRS backscatter with a total power waveform as shown in the “seed beam only” case in Fig. 132.109. When (in a separate experiment) the seed beam was intersected by a cone of two to six pump beams that were pointed to cross the seed on the front side of the foil (where the density and temperature would allow further re-amplification of the SRS), a significant enhancement in the scattered power was observed. The

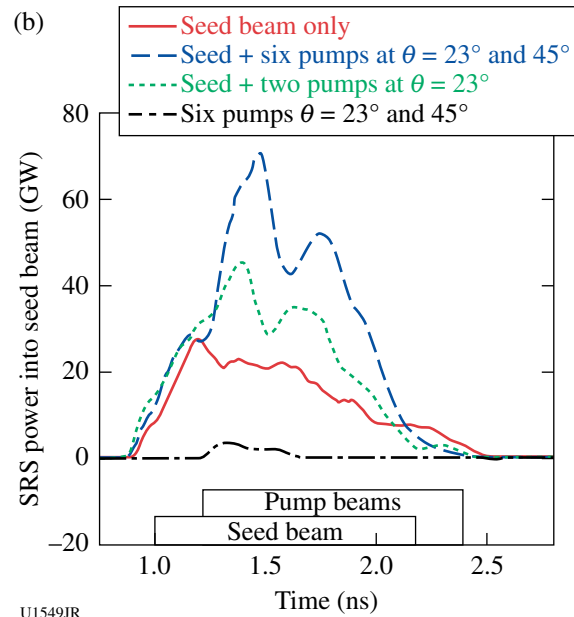
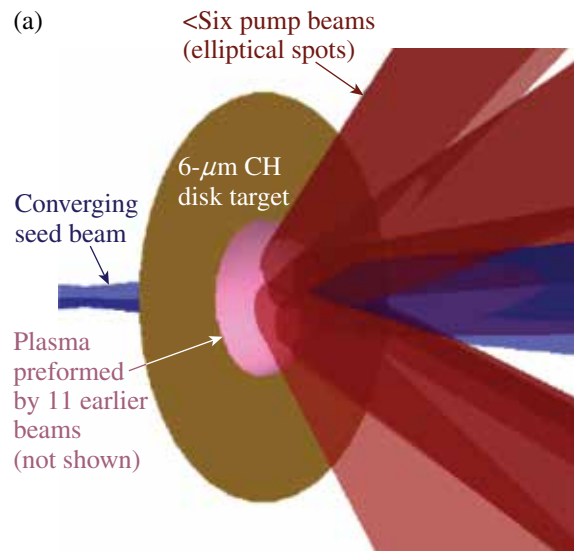


Figure 132.109  
The geometry and measured SRS backscatter of a seed beam in the presence of different numbers of pump beams, from the SRS multipump experiments.

enhanced level of power was seen to increase with the number of pumps as expected from models of SRS re-amplification, and the total peak SRS was significantly greater than the sum of the SRS observed in both “seed only” and “six pumps” cases, as also shown in the figure. The overall increase in SRS with all beams cannot be explained by the simulated change in absorption by the plasma due to the pump beams and has the magnitude expected for SRS re-amplification. The experiment has provided an important benchmark for models of multibeam stimulated Raman scattering from ignition experiments.

### Comparison of Plastic and High-Density Carbon Ablator Performance

Principal Investigator: S. Ross

The HDCEnergy-12A campaign successfully compared high-density carbon (HDC) and CH ablator performance. A series of OMEGA experiments with three distinct pulse shapes were used to investigate HDC and CH performance. The pulse shapes were designed to deliver different drive pressures during the foot of the laser pulse. The pulses delivered foot pressures ranging from ~1.7 Mb (LA234002) to ~7.5 Mb (LA190801) with an intermediate pressure of ~3.6 Mb (LA232301). The capsules were filled with either 40 atm or 20 atm of deuterium. The measured neutron yield is shown in Fig. 132.110.

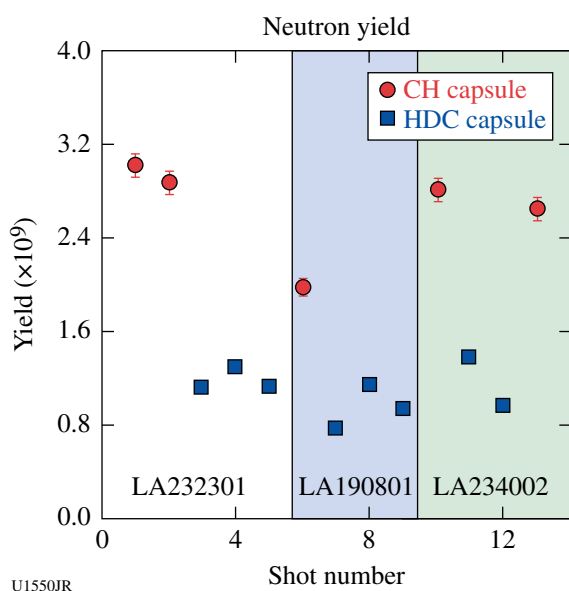


Figure 132.110 The measured neutron yield for different capsule materials and pulse shapes.

The HDC capsules showed very similar neutron yields for all three pulse shapes. This is evidence that the capsule's compression and performance are independent of the pressure in the laser foot for pressures ranging from 1.7 Mb to 7.5 Mb. The difference in HDC and CH yields are expected because of differences in capsule thickness. These results are being used to design future HDC experiments.

### Shock Release of ICF-Relevant Materials

Principal Investigator: D. E. Fratanduono

Inertial confinement fusion (ICF) capsule implosions are driven by four shock waves. The strength and timing of each shock are controlled to maintain a low adiabat. High-pressure

(>1-Mbar) equation-of-state (EOS) experiments on ICF ablators have been primarily limited to Hugoniot measurements. These experiments focus on developing a technique to measure the release isentropes of ICF-relevant materials in order to better constrain the EOS of ICF-relevant materials.

Experiments are performed at the Omega Laser Facility. Target design consists of a glow-discharge polymer (GDP, an ICF ablator), and a thin (~50-nm) silicon nitride film separated by a vacuum or gas-filled gap (~250  $\mu\text{m}$ ) as shown in Fig. 132.111. A strong shock (>250 GPa) is generated in the GDP ablator. When the shock breaks out of the sample and into vacuum, it releases and isentropically expands as it propagates across the gap. When the strong shock in the GDP enters the gas-filled void, a weak shock is generated and propagates across the gap. By measuring the shock state of the gas, a point on the GDP release isentrope is determined. The released material stagnates on the silicon nitride. The velocity of the silicon nitride is measured using a velocity interferometer system for any reflector (VISAR). Using the measured velocity profile, a momentum balance technique is employed to extract information regarding the release isentrope.

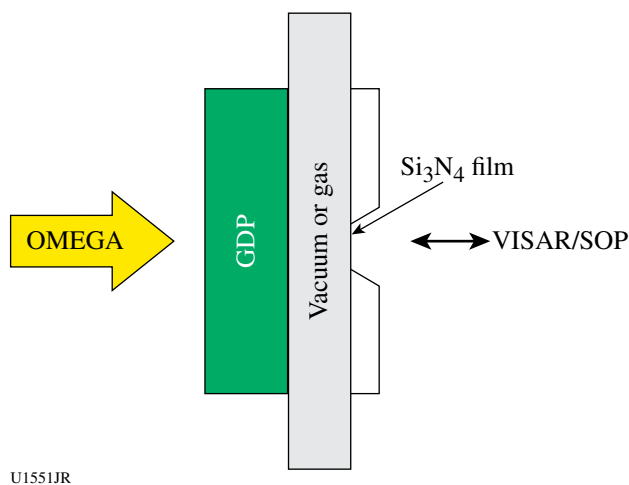
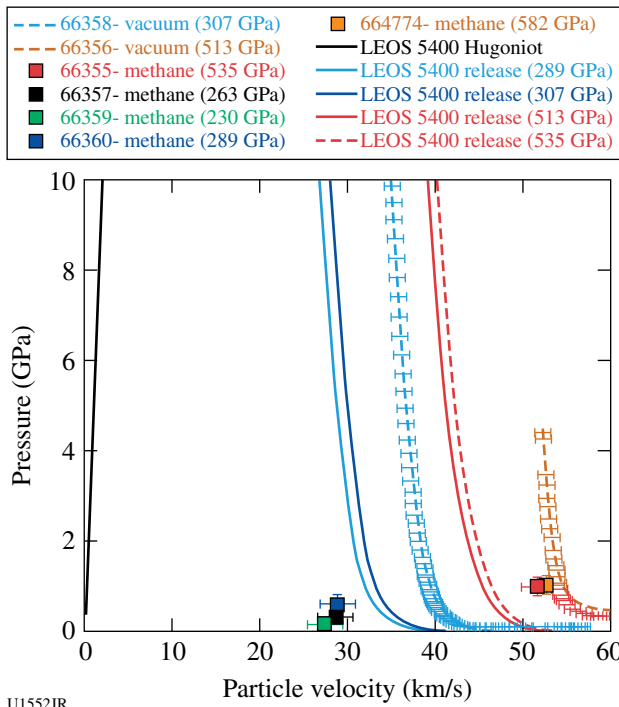


Figure 132.111 Target design.

The vacuum results indicate that the velocity of the leading edge of the release isentrope is traveling ~30% faster than predicted by the LEOS tables. This behavior has been observed on CH, GDP, and diamond. These results are shown in Fig. 132.112. The gas (methane)-filled results are consistent with Hugoniot generated from LEOS tables. However, the data at lower-pressure shock states are inconsistent with the vacuum measurements. Further experiments are being performed to examine this discrepancy. We are in the process of designing



U1552JR

Figure 132.112  
Glow-discharge–polymer release isentropes.

targets to measure the release of D<sub>2</sub> ice into low-density D<sub>2</sub> gas. Using this technique, we may be able to determine species separation for DT.

### High-Energy-Density Experiments

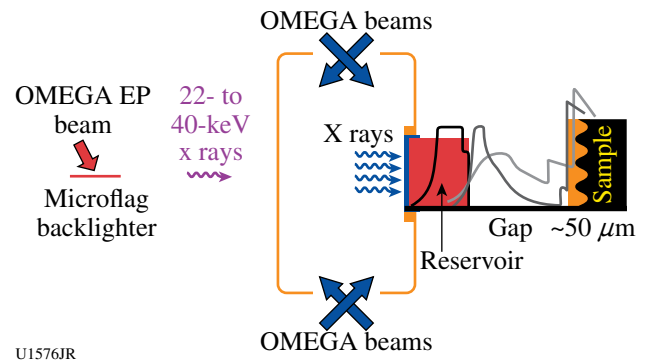
#### 1. Material Dynamics and Equation of State

##### Tantalum Rayleigh–Taylor Experiments

Principal Investigators: H.-S. Park and C. Plechaty

The focus of the ICETaRT campaign was to study Ta material strength at high pressure (>1 Mbar) and high strain rates (10<sup>6</sup> to 10<sup>8</sup> s<sup>-1</sup>). To achieve these conditions in the experiment while keeping the temperature of the Ta sample well below melting, a reservoir and vacuum gap<sup>75</sup> configuration was employed to produce a quasi-isentropic pressure drive (see Fig. 132.113). The plasma drive was produced by ablating a hohlraum with 40 OMEGA beams to deposit a total energy of 20 kJ. Attached to the side of the hohlraum was an ablator/reservoir and a physics package, which were separated by a vacuum gap to produce ramped drive conditions onto the physics package.

The physics package consisted of a CH heat shield placed on a Ta sample. Sinusoidal perturbations were imposed on the



U1576JR

Figure 132.113  
Experimental configuration employed for OMEGA EP joint shots. OMEGA beams deposited energy into the hohlraum, producing a plasma drive. Face-on high-energy radiography was employed on the rippled Ta sample by using a short-pulse OMEGA EP beam to ablate an Ag backlighter. For OMEGA shots, the rippled Ta sample was replaced by a VISAR witness sample to characterize the plasma drive.

surface of the Ta. As the plasma from the reservoir crosses the gap and stagnates on the sample package, the Ta ripples undergo an effective acceleration from the stagnating plasma drive. This acceleration actuates Rayleigh–Taylor (RT) growth of the pre-imposed sinusoidal pattern. Since the Ta material strength acts to suppress the amount of RT growth, measuring the RT ripple amplitude gives a measure of the material strength.<sup>75–77</sup> To measure the perturbation amplitude, face-on high-energy (22-keV Ag K<sub>α</sub>) radiography was employed using an OMEGA EP short-pulse beam. We needed the OMEGA EP beam to employ a high-energy backlighter (22 keV) to probe the high-Z tantalum material. The amount of backlighter transmission through the ripples is governed by the quantity  $\rho\Delta Z$ , where  $\rho$  is the density of the driven ripples and  $\Delta Z$  is the amplitude. The RT growth factor (GF) is determined by measuring the driven  $\rho\Delta Z$ :<sup>75,78</sup>

$$GF = \frac{(\rho\Delta Z)_{\text{driven}}}{(\rho_0\Delta Z_0)_{\text{undriven}} gMTF}, \quad (1)$$

where  $\rho_0$  and  $\rho Z_0$  are the initial density and ripple amplitude (determined from pre-shot metrology) and the MTF is the modulation transfer function, which characterizes the frequency response of the system and is measured by using a knife edge. To determine the properties of the plasma drive, separate shots without the backlighter were performed by replacing the physics package with a witness sample and taking VISAR measurements.

The FY12 ICETaRT campaign employed the experimental setup discussed above to study several aspects of Ta material

strength. The first topic studied was the Ta material failure threshold. In previous experiments, we observed (Fig. 132.114) that as the relative growth increased, defined as the ratio between the ripple amplitude and the Ta sample thickness, the measured relative growth deviated from that predicted by the multiscale model.<sup>79</sup> To study the threshold where the relative growth measured in the experiment deviates from that predicted by the multiscale model, or measure the threshold where failure occurs, a three-amplitude pattern was employed. The Ta sample was split into three regions, each with a 50- $\mu\text{m}$  wavelength, but with a different amplitude—namely, 1.0, 2.0, and 3.5  $\mu\text{m}$ . We found that failure occurred as the relative growth in experiment exceeded  $\sim 20\%$ .

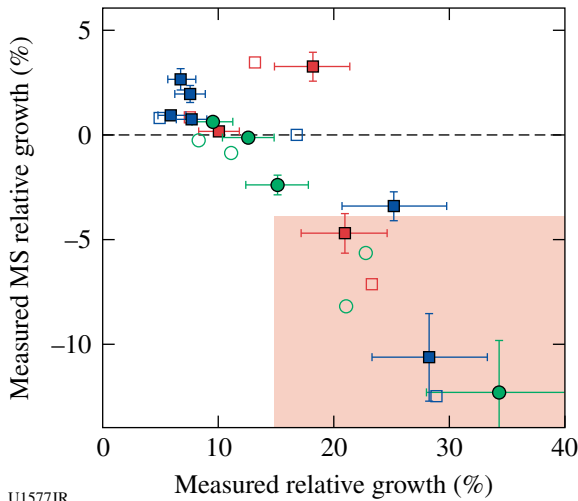


Figure 132.114 Plot of measured relative growth (RG) versus the deviation of the measured relative growth from that predicted by the multiscale (MS) model. The colored box in the lower right-hand corner denotes where the absolute value of this difference becomes  $>4\%$ . This is defined as failure.

The second topic studied was a comparative material strength study between Ta [100] and Ta [111] crystal orientations. In previous studies<sup>80</sup> the target samples were predominantly in the [111] orientation. In the multiscale model, crystal orientation can affect material strength via the Taylor factor. To understand the effect of crystal orientation on the material strength, we placed the two samples side by side and compared the ripple growth for a given shot (see Fig. 132.115). Initial results from just a few shots suggest that the difference in the growth factor between these two crystal orientations is too small to be measured within our error bars of  $\sim 18\%$ .

Lastly, the final topic of study undertaken in the FY12 ICE-TaRT campaign was the study of a new multimode configura-

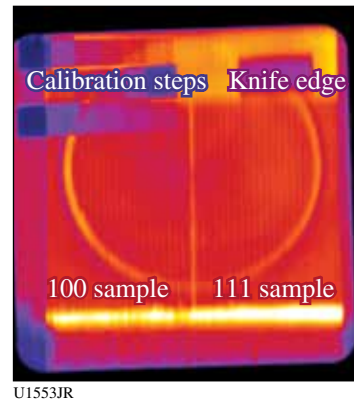


Figure 132.115 Radiography image of [100] and [111] target configuration. The 100 sample is on the left, and the 111 sample is on the right. The calibration steps are employed to relate the backlighter transmission to a specific value of  $\rho\Delta Z$ . The knife edge is used to determine the MTF. The circular structure in the middle is a hole in the hohlraum and indicates where the plasma drive can stagnate onto the sample, driving RT ripple growth.

tion (Fig. 132.116). A superposition of two different sinusoidal ripple patterns was imposed on the Ta sample. The two modes employed had the same amplitude (1.85  $\mu\text{m}$ ) but different wavelengths (75 and 112  $\mu\text{m}$ , respectively) and phases ( $210^\circ$  and  $24^\circ$ , respectively). The purpose of this study was twofold. The first purpose was to study the coupling of RT growth between the modes. For example, the growth of the designed modes with wave vectors  $k_1$  and  $k_2$  induced growth at  $|k_1 \pm k_2|$ ,  $2k_1$ , and  $2k_2$ . The exact details of the coupling are not fully understood. Second, by using multiple modes, the multimode configuration can be used to produce simultaneous Rayleigh–Taylor (RT) measurements, with corresponding strengths. A detailed analysis of this data is currently underway.

### Iron Rayleigh–Taylor Experiments

Principal Investigator: C. Plechaty

The ICEIronRT campaign focused on the study of iron material strength at high pressures and strain rates when a phase transition occurs at lower pressures ( $\sim 100$  kbar). The goal was to understand the strength parameter difference at high pressure when a phase transition occurs from the  $\alpha$ -to- $\epsilon$  phase at a lower pressure level.

For ICEIronRT, we employed a quasi-isentropic plasma drive produced by a reservoir–gap–sample configuration.<sup>76</sup> A newly designed 6% BrCH reservoir was employed to achieve pressures up to  $\sim 1.5$  Mbar. In the experiment, 40 OMEGA beams (with a total energy of 20 kJ) were employed to ablate a hohlraum with a side-mounted reservoir–gap–sample pack-

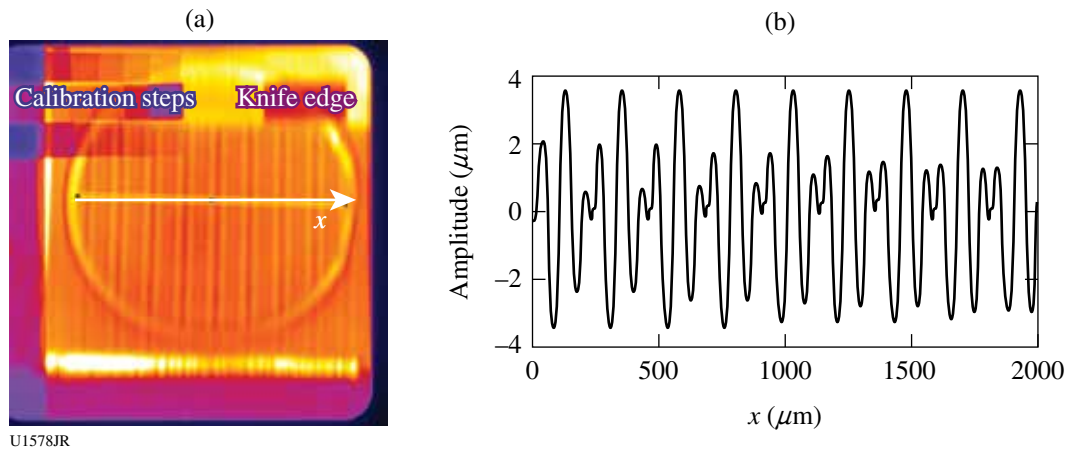


Figure 132.116  
 (a) The radiography image obtained for this multimode configuration; (b) an ideal plot of the ripple structure for  $0 < x < 2000 \mu\text{m}$ .

age in order to produce a plasma drive. As the plasma drive crossed the vacuum gap, it stagnated onto the Fe sample with an imposed sinusoidal pattern on the surface. The stagnation of the plasma drive onto the Fe sample drives Rayleigh–Taylor (RT) growth of the ripples where the observed RT growth rate is dependent on the strength.

To obtain the quantities listed in Eq. (1),  $\rho_0\Delta Z_0$  was derived from pre-shot Veeco measurements and the MTF was measured using a knife edge (Fig. 132.117). To measure  $\rho\Delta Z$  for the driven sample, face-on high-energy (22-keV) radiography

was employed using an Ag microflag backlighter ( $200 \times 200 \times 5 \mu\text{m}$ ). A short-pulse (100-ps) OMEGA EP beam was employed to ablate the backlighter with a 1.0-kJ pulse delivered with a given time delay in respect to the OMEGA drive beams. To resolve the ripple growth, the thinnest side of the backlighter was aligned along the direction of the ripples.

In addition to joint OMEGA EP shots, OMEGA-only shots were performed to determine the properties of the plasma drive. In these shots, the Fe sample was replaced with a witness sample and VISAR measurements were performed.

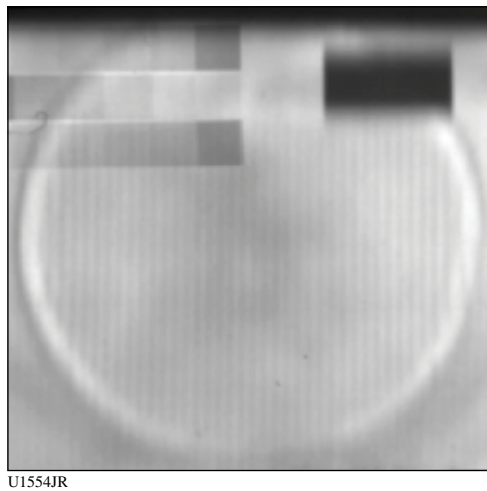


Figure 132.117  
 A radiograph for shot 67210 (60-ns delay). The iron calibration steps, located in the upper left-hand corner, are used to relate the backlighter transmission to a specific value of  $\rho\Delta Z$ . The knife edge located in the upper right-hand corner is used to measure the MTF. The circular feature in the middle of the image indicates the region of driven ripple growth.

Figure 132.118 compares the undriven ripple  $\rho_0\Delta Z_0$  and the driven ripple  $\rho\Delta Z$ . As shown,  $\rho\Delta Z > \rho_0\Delta Z_0$ , indicating that the driven ripples have undergone RT growth. The GF, calculated

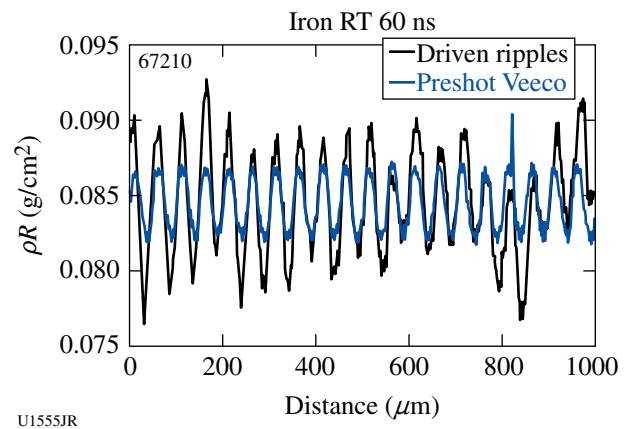


Figure 132.118  
 Comparison of the pre-shot values of  $\rho_0\Delta Z_0$  and the shot values of  $\rho\Delta Z$  for a 60-ns delay between the OMEGA drive and OMEGA EP backlighter beams.

with Eq. (1), is shown in Fig. 132.119 with error bars of  $\sim\pm 50\%$ . An initial analysis indicates that the iron material strength is higher than that predicted using a hybrid  $\alpha$ -to- $\epsilon$  phase-transiting Preston–Tonks–Wallace (PTW) strength model<sup>81</sup> calculated using our experimental condition of  $\sim 1.5$ -Mbar pressure and strain rate  $>10^6$  s<sup>-1</sup>.

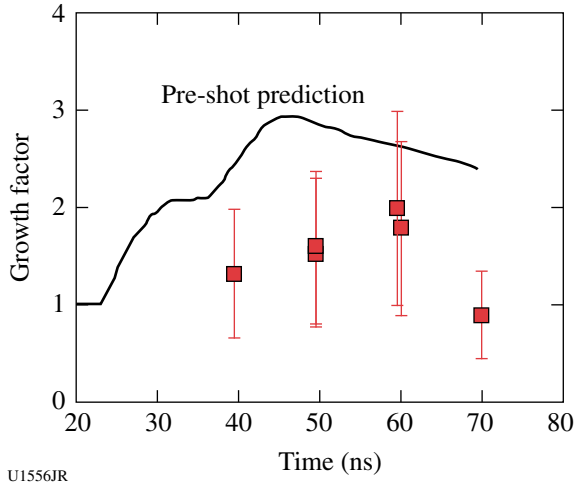


Figure 132.119  
Comparison between the GF (with error bars of 50%) and the GF prediction obtained from a hybrid  $\alpha$ -to- $\epsilon$  transition PTW model.

**Double-Pulse Radiography Development**

Principal Investigator: C. Plechaty

Laser-driven, high-energy ( $>22$ -keV) x-ray radiography has been employed as a diagnostic tool in many different types of high-energy-density (HED) experiments with applications ranging from material strength studies<sup>75,78,82,83</sup> to capsule

implosion experiments. In FY12, the DBLPULSE campaign focused on the development of a new multiframe radiography technique that takes advantage of the multiple beams available at state-of-the-art laser facilities such as Omega and the NIF. This concept is of particular importance to the NIF and HED programs since it will yield twice the amount of data per shot.

Experiments were performed on OMEGA EP using two short-pulse (100-ps, 100- $\mu$ m spot size) beams to independently ablate two  $300 \times 300 \times 10$ - $\mu$ m foils (Cu and Ag) placed 1.2 mm apart (Fig. 132.120). In the experiment a 1-kJ beam was employed to ablate the Cu backlighter. After delayed time  $t$ , the Ag backlighter target was irradiated by a 1.5-kJ beam. The performance of the two time-delayed x-ray pulses were tested by radiographing a Au grid pattern placed 10.3 mm from the foils. To obtain two distinct images of the grid pattern, a collimator was employed. The collimator consisted of a 1-mm-thick Au disk, with two tapered holes to act as pinholes for each backlighter. The surface of the collimator was placed 3.2 mm from the center of the foils. The angle of the holes was chosen such that two distinct and spatially separate images were produced at the location of the image plate (IP), placed  $\sim 500$  mm from the foils.

To characterize the frequency response of the system, we employed a Au grid pattern that consisted of several orthogonal mesh elements, each with different spatial scales. The Au grid had 10-, 20-, 30-, 40-, and 80- $\mu$ m mesh features, aligned along the horizontal and vertical axes of the grid. The Cu and Ag foils were mounted orthogonal to each other and the IP such that each backlighter would produce a 1-D orthogonal x-ray source aligned along either the vertical or horizontal axis of

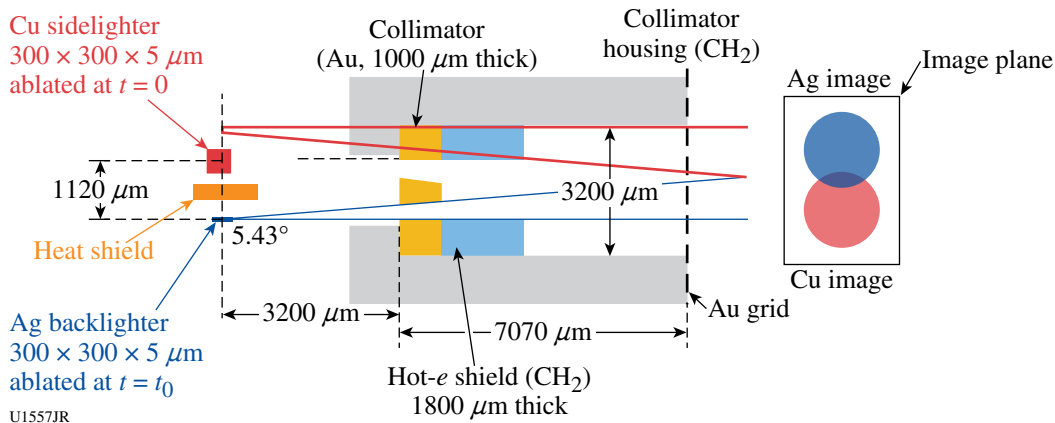


Figure 132.120  
Schematic of experimental setup. X rays from the two independently ablated backlighter foils pass through a collimator assembly. This produces two temporally and spatially independent images of an Au grid on an image plate.

the Au grid. The IP was placed far enough away so that two spatially distinct images were captured.

To protect the second backlighter target from the hydrodynamic expansion and x-ray emission from the first backlighter, a heat shield was placed between the foils on a separate target positioner.

Radiography images captured using this configuration are shown in Fig. 132.121. In Figs. 132.121(a)–132.121(c), the heat shield employed was a  $1000 \times 1000 \times 200\text{-}\mu\text{m}$ -thick CH heat shield. At  $t = 0$  ns [Fig. 132.121(a)] the 10-, 20-, 30-, and 80- $\mu\text{m}$  features are clearly visible in the Cu (top) image. In the Ag (bottom) image, the 10- and 30- $\mu\text{m}$  features are observed, while the other features are located out of the instrument field of view. At  $t = 5$  ns [Fig. 132.121(b)], the image produced by the delayed backlighter is observed to degrade; only the 30- $\mu\text{m}$  features are visible. This trend continues when  $t = 20$  ns [Fig. 132.121(c)], where the Ag backlighter resolution has degraded enough so that the grid features are not observed.

An explanation for the reduction in the image quality can be found by examining the time-integrated x-ray pinhole camera (XRPHC) images (Fig. 132.122). As shown by Fig. 132.122, the Ag backlighter x-ray source size becomes notably larger for the  $t = 20$  ns case [Fig. 132.122(c)] when compared to the  $t = 0$  ns case [Fig. 132.122(b)], causing the delayed image quality to degrade.

Since the CH heat shield employed for the images captured in Figs. 132.121(a)–132.121(c) is transparent to laser backscatter and x-ray emission from the  $t = 0$  ns backlighter, it was replaced

by a  $1000 \times 1000 \times 50\text{-}\mu\text{m}$  Au heat shield [Fig. 132.121(d)]. When employing this heat shield design, the resolution of the delayed backlighter only slightly increases. Employing an even thicker Au heat shield ( $1000 \times 1000 \times 200\text{ }\mu\text{m}$ ) does not yield better system resolution.

Since the 50- $\mu\text{m}$ -thick and 200- $\mu\text{m}$ -thick Au heat shields prevent a significant portion of the low-energy x-ray emission from the Cu backlighter from reaching the Ag backlighter, the observed preheating of the Ag backlighter is likely caused by radiating plasma expansion. As the Cu backlighter is ablated, the resulting plasma expands past the heat shield and radiates. This causes the Ag backlighter to be preheated, producing plasma and increasing the x-ray source size once the backlighter is ablated. A future study will investigate this effect.

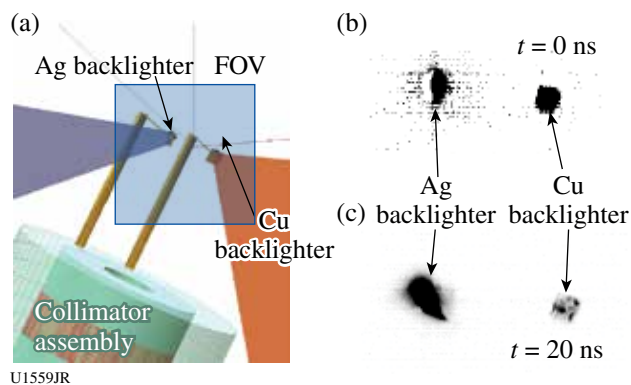


Figure 132.122 XRPHC images. (a) Image geometry showing the Cu beam and backlighter (on the right) and the Ag beam and backlighter (on the left). The field of view (FOV) for the XRPHC images is shown. The captured time-integrated images are shown in (b) for the case of  $t = 0$  ns and (c) for the case of  $t = 20$  ns.

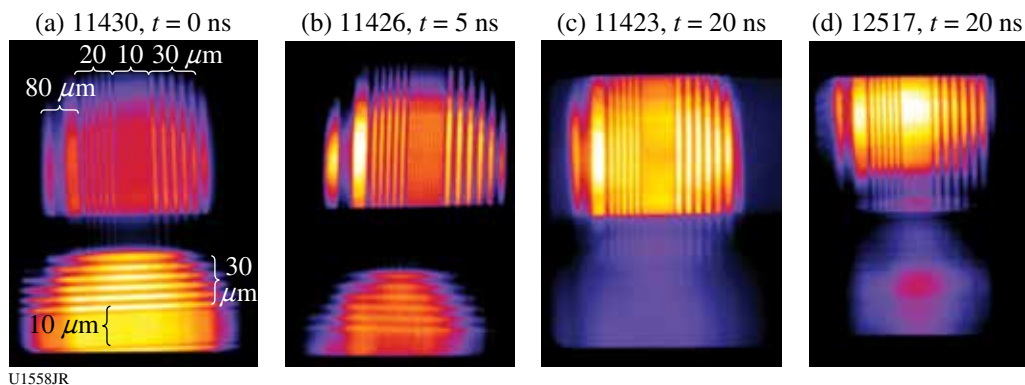


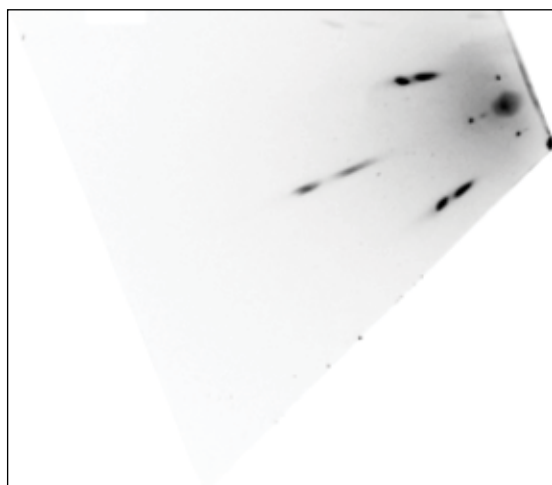
Figure 132.121 Images obtained with the HERIE. In these images, the top image was produced by the Cu backlighter, which is always taken at  $t = 0$  ns. The bottom image was produced by the Ag backlighter, which ablates the foil at the time shown. [(a)–(c)] A  $1000 \times 1000 \times 200\text{-}\mu\text{m}$ -thick CH heat shield was employed; (d) a  $1000 \times 1000 \times 50\text{-}\mu\text{m}$ -thick Au heat shield was employed.

### ***Diffraction Studies on Shocked Tantalum***

Principal Investigators: B. Maddox, A. Comley, and C. Wehrenberg

Three distinct experiments were conducted to study the behavior of shocked and ramp-loaded tantalum.

*StrDiff-12A*: The goals of the StrDiff-12A campaign were to observe twin formation in single-crystal Ta shocked along the [110] direction, obtain large-pinhole diffraction for a quantitative temperature analysis of shocked Ta, extend out previous measurements of the lattice anisotropy of Ta shocked along [100] to lower peak pressure, verify our simulations using a stepped diamond drive target, and test a glueless target for future studies of shock- and ramp-compressed Ta. The experiment used the broadband x-ray diffraction diagnostic (BBXRD) on TIM-4 as the primary diffraction diagnostic, as well as the tilted VISAR. Crystal samples were driven using a single beam (Beam 18) with an SG8 phase plate. The x rays for diffraction were produced by an imploded CH shell driven by 44 beams with SG4 phase plates. All beams used a 1-ns square pulse. We achieved 12 shots and obtained excellent data. Due to the initial crystal sample quality of the Ta [110] samples, we were unable to observe any useful driven diffraction patterns for Ta shocked along [110] and, therefore, observed no twinning. However, all other experimental goals were met. In this campaign, we recorded our highest-quality Laue diffraction pattern to date, detecting up to seven compressed diffraction spots on a single side of the BBXRD detector (shown in Fig. 132.123).



U1560JR

Figure 132.123  
Example of high-quality Laue diffraction recorded from Ta single-crystal shock compressed to ~0.5 Mbar along the [100] direction.

*ShkLaue-2012*: In ShkLaue-2012 our goal was to extend previously successful strength measurements of shocked Ta using *in-situ* Laue diffraction to ramped-loading conditions, allowing us to compare our measurements to Rayleigh–Taylor strength experiments with similar strain rates. As in previous ShkLaue campaigns, the BBXRD diagnostic was used to record Laue diffraction data, giving a direct measurement of lattice anisotropy and shear strength of the material. A reservoir drive was developed in which a directly driven brominated-CH reservoir releases across a gap and creates a ramped stagnation shock on the Ta sample. A new glueless target design was also developed for this campaign, in which the Ta samples were kept on the MgO substrate and the substrate was polished down to the desired thickness. This design allowed us to record high-quality VISAR data simultaneously with Laue diffraction data. Initial analysis shows that the reservoir drive was successful in creating the ramped drive, which demonstrated highly repeatable behavior. High-contrast diffraction data were recorded for a range of drive times and show a range of lattice anisotropy ratios.

*EP-TaBragg-2012*: In EP-TaBragg-2012 our goal was to study shock-compressed Ta using *in-situ* Bragg diffraction, building on the successful BraggDiff-2011 campaign. The experimental configuration used the Lawrence Livermore diffraction imager as the primary diagnostic on TIM-13. Samples were driven using two defocused beams with a 10-ns pulse, while a short-pulse beam was used to drive a silver backlighter to create the high-energy x rays. There were a few issues in adjusting the drive-backlighter relative timing, producing an imbalance in the signal strength in either the driven or static diffraction signal in the initial shots. This issue was solved by comparing VISAR data with previous campaigns, resulting in a 0.5-ns shift from previous experiments. The data quality obtained was excellent and, combined with BraggDiff-2011 data, provides a range of pressures for Ta strength measurements.

### ***Ta X-Ray Diffraction***

Principal Investigators: A. Lazicki, J. H. Eggert, and J. R. Rygg

In FY12 powder x-ray diffraction experiments (Fig. 132.124) on solid ramp-compressed tantalum yielded additional data points confirming a high-pressure phase transition near 300 GPa (Fig. 132.125). The structure was determined to be consistent with a predicted simple hexagonal ( $\omega$ ) phase.<sup>84,85</sup> During the shot day, we ramp compressed Ta and Fe samples to pressures above 10 Mbar. The technical difficulties encountered while trying to measure x-ray diffraction at these high pressures

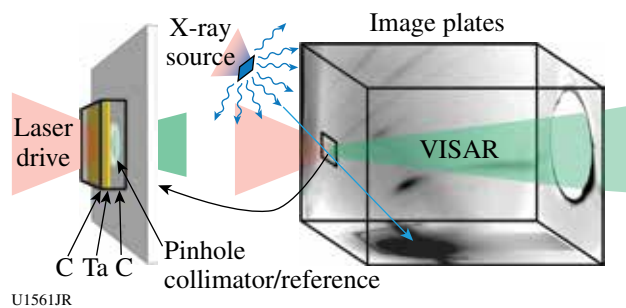


Figure 132.124  
X-ray diffraction experimental setup. The target consisted of a 4- $\mu\text{m}$  foil of Ta sandwiched between single-crystal diamond plates. The x-ray source was laser-excited  $\text{He}_\alpha$  radiation from Fe or Cu thin foils. X rays diffracted off of the Ta sample were scattered onto the inner surfaces of a box lined with image plates, yielding crystal structure and volume. Target rear-surface velocities were detected using VISAR, yielding pressure.

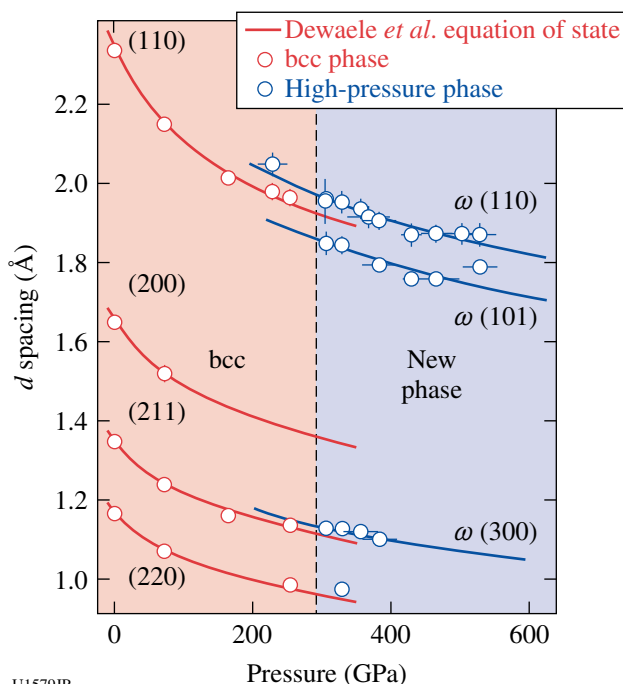


Figure 132.125  
Shift of the  $d$  spacings of x-ray diffraction peaks under pressure showing evidence of a new phase at 300 GPa.

have provided critical feedback for our design of terapascal-range x-ray diffraction experiments on the NIF.

### Hydrogen Equation of State

Principal Investigators: A. Lazicki, M. Millot, J. R. Rygg, and J. H. Eggert

The purpose of this study was to look for pressure-induced chemistry in deuterium by electron doping from an added ~5%

of xenon, evidenced by the effects on the Hugoniot and the reflectivity, compared to pure deuterium. Gas mixtures were precompressed to fluid deuterium density in a diamond anvil cell prior to shock compression. Measurements (Fig. 132.126) reveal a Hugoniot shifted to higher density but not to the extent predicted by a simple linear mixing model, indicating chemical interaction between the species. There is, however, some uncertainty in the concentrations of gas captured in the diamond cells, so the conclusion awaits further experiments. Because of difficulties in sample preparation, some of the shots were devoted instead to the measurement of the Hugoniot of the hydrogen compound lithium hydride (Fig. 132.127), precompressed to 5 to 9 kbar in a diamond anvil cell. Results will aid in refinement of equation-of-state models.

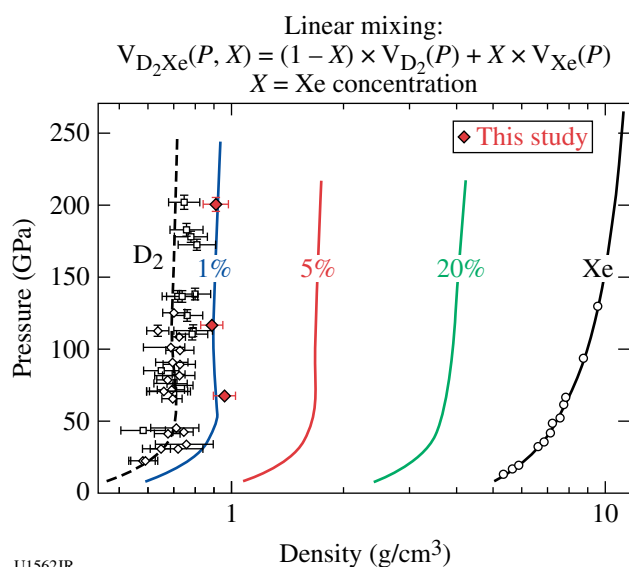
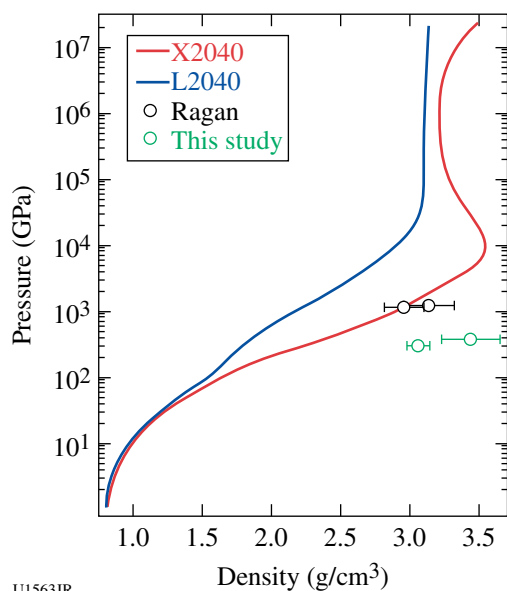


Figure 132.126  
Hugoniot of  $\text{D}_2$  (Ref. 86) and Xe (Ref. 87) compared with the data from this study. Curves predicting the behavior the mixture are based on the linear mixing model.

### XAFS Study of Ramp-Compressed Fe, Ta, and Mo

Principal Investigator: Y. Ping  
Co-investigators: F. Coppari, D. G. Hicks, D. E. Fratanduono, S. Hamel, J. H. Eggert, J. R. Rygg, R. F. Smith, D. C. Swift, and G. W. Collins (LLNL); B. Yaakobi and T. R. Boehly (LLE)

Extended x-ray absorption fine structure (EXAFS) measurements of dynamically compressed iron have been performed on OMEGA using an implosion backlighter. Iron is compressed in the solid state to 560 GPa (5.6 Mbar), the highest solid-state pressure for iron explored in the laboratory (Fig. 132.128). EXAFS measurements provide simultaneous density, tem-



U1563JR

Figure 132.127

Hugoniot of LiH from EOS models, compared to experimental data.<sup>88</sup> The data shown from this study are for LiH precompressed to  $\sim 6.5$  kbar.

perature, and local-structure data for compressed iron in this new regime—the first such data for constraining solid-state theory and evolution models for many newly discovered extra-solar terrestrial planets. The data show that the close-packed structure of iron is stable up to 560 GPa, the temperature at peak compression is significantly higher than expected from

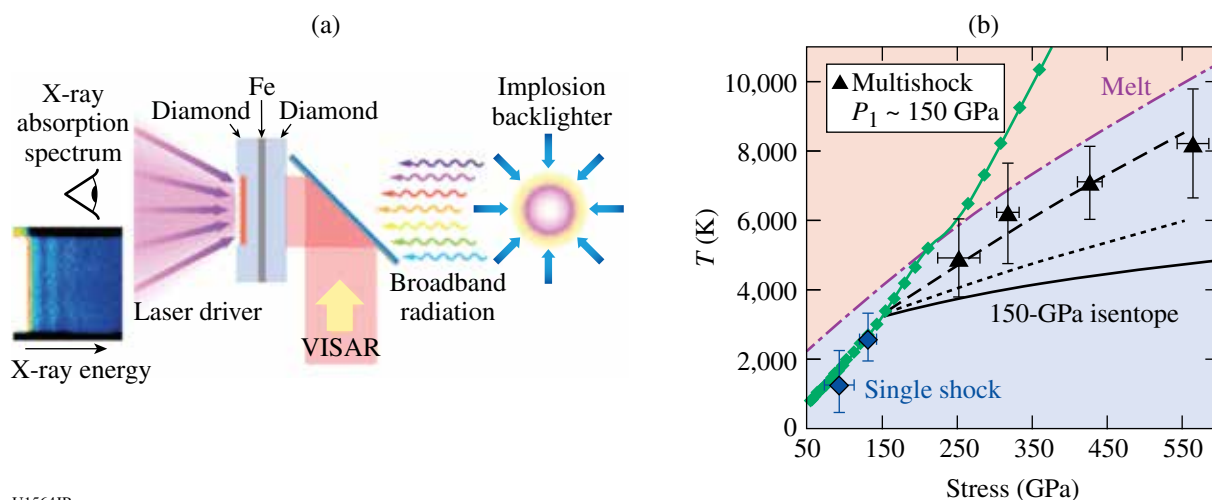
pure compressive work, and the strength of iron is many times greater than expected from lower-pressure data.<sup>89</sup>

Based on the success of EXAFS measurements of iron, we have extended this platform to study L edges of Ta and Mo. Data on Mo at ambient conditions, 2 Mbar, and 3 Mbar have been obtained, and EXAFS of undriven Ta has been observed for the first time on OMEGA. The last campaign in September 2012 demonstrated  $2\times$  enhancement in backlighter brightness and  $4\times$  enhancement in the spectrometer efficiency, making it possible to do single-shot EXAFS measurements of driven Ta in FY13.

### Tin Melt

Principal Investigator: A. Lazicki

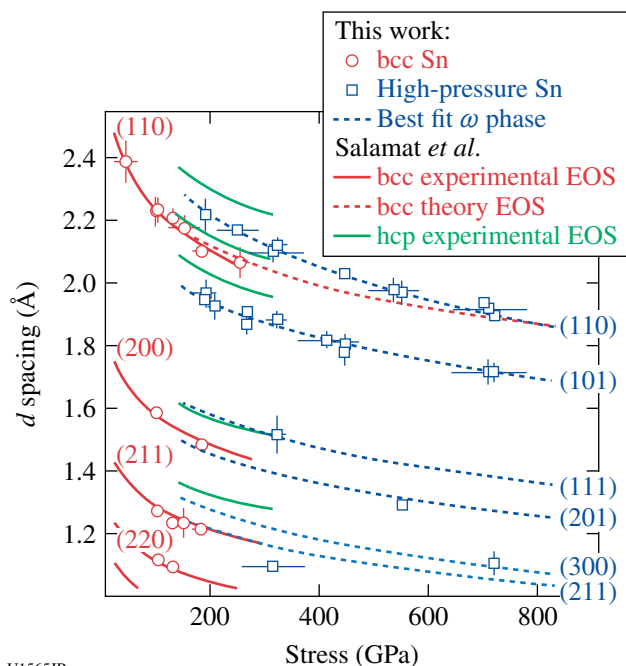
Campaigns investigating the high-pressure solid crystal structure and probing the melting curve of tin have continued in FY12, extending the measured diffraction up to 720 GPa (Fig. 132.129), and potentially yielding information about the melting curve up to 300 GPa (Fig. 132.130). The new x-ray diffraction data provide further evidence for a high-pressure, high-temperature phase transition near 200 GPa. The structure of this new phase differs from the hexagonal close-packed structure that arises near 200 GPa at ambient temperature.<sup>90</sup> We propose the simple hexagonal omega phase as a likely crystal structure for this new phase. The particle velocity histories of shock-melted and ramp-compressed tin show a plateau consistent with changing sound velocities at a phase transition such as recryst-



U1564JR

Figure 132.128

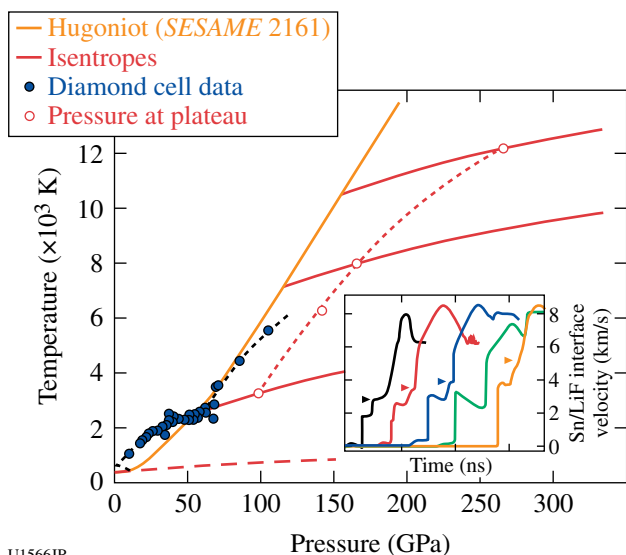
(a) Experimental schematic. The raw image of a typical x-ray absorption spectrum is displayed at the lower left corner, showing the intensity modulations above the K edge. (b) Temperature inferred from EXAFS data as a function of stress for the shock + ramp data with an initial shock of 150 GPa. The single-shock data are also shown (blue diamonds). The melting curve (dashed-dotted lines) and the Hugoniot (green solid lines with squares) are plotted for comparison. Also shown are isentropes (solid lines), isentropes with the temperature increase calculated using static strength  $Y_{sta}$  (dotted lines), and dynamic strength  $Y_{dyn} = 3Y_{sta}$  (dashed lines).



U1565JR

Figure 132.129

The  $d$  spacing of observed peaks, compared with known isothermal equation of state and phase transition from static experiments.<sup>90,92,93</sup> Our observed high-pressure  $d$  spacings fit a simple hexagonal ( $\omega$ ) phase. The line weight is proportional to the expected relative peak intensity.



U1566JR

Figure 132.130

Melting curve of tin with new data from this study, determined from the pressure at which a plateau is seen in the ramp-compression wave profile (shown in the inset). Paths in phase space are approximated as shown, with the temperatures associated with the principle Hugoniot and subsequent ramp-compression pathways (modeled as isentropes) determined from the SESAME 2161 table.

tallization. Assuming recrystallization, a preliminary analysis shows the melting temperature rising steeply with pressure, in qualitative agreement with recent diamond anvil cell results.<sup>91</sup>

### Gigabar Equation of State

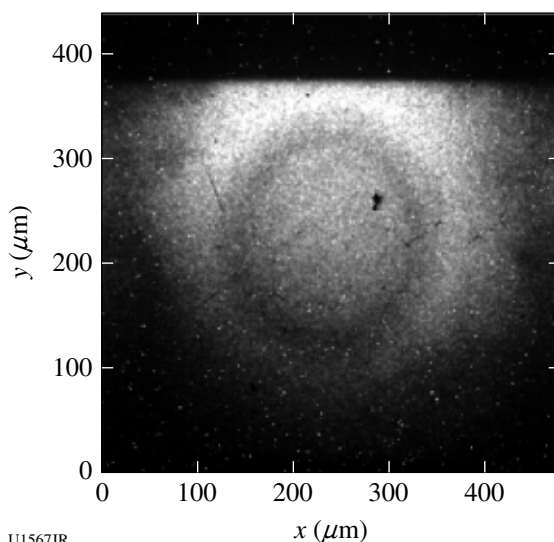
Principal Investigator: J. Hawreliak

High-pressure equation-of-state (EOS) experiments using convergent compression of a solid spherical target have a geometric advantage over conventional planar techniques, in which a constant ablation pressure causes the propagating shock to maintain a constant pressure, because in the converging case the shock will increase in strength as it approaches the sphere's center. This approach makes it possible to achieve shock pressures >100 Mbar at the Omega Laser Facility. These experiments use *in-situ* gated radiography to measure the propagating shock speed and density. We will apply the Hugoniot relations to determine the pressure based on the measure shock front speed and density:

$$P = \rho_0 u_s^2 \left( 1 - \frac{\rho_0}{\rho} \right)$$

$$\frac{\delta P}{P} = \sqrt{\left( \frac{2\delta u_s}{u_s} \right)^2 + \left[ \left( \frac{\rho_0}{\rho - \rho_0} \right) \frac{\delta \rho}{\rho} \right]^2}, \quad (2)$$

where  $\rho_0$  is the initial density and  $\delta u_s$ ,  $\delta \rho$ , and  $\delta P$  are the associated uncertainties in the shock speed, density, and pressure, respectively. Figure 132.131 is an example of a single frame



U1567JR

Figure 132.131

Gated 2-D radiograph from a shock propagating through a solid sphere, demonstrating a key capability needed for high-pressure equation-of-state measurements.

from a radiograph image from which the density profile can be inferred.

### Equation of State for Foams Using OMEGA EP

Principal Investigator: J. Hawreliak

The equation of state (EOS) of porous materials is of great interest in high-energy-density (HED) science because it allows conventional shock techniques to achieve different thermodynamic end states than the principal Hugoniot. Figure 132.132 is an example of the pressure–density space of shock-compressed quartz for a range of different initial densities. For the low-density foam materials, where the final density is below the ambient density of the base material, the pressure is dominated by the thermal pressure caused by compressing the voids in the material. Many carbon-based foams are opaque, unlike transparent foams where the shock front becomes reflective at high pressures and velocity can be measured directly. The opaque materials require an x-ray technique to view the shock. We are developing an *in-situ* radiograph technique to make Hugoniot EOS measurements of shock-compressed opaque low-density foams. We had success using a chlorinated plastic (PVC) area backlighter for 50-mg/cm<sup>3</sup> carbon resorcinol foam (CRF).

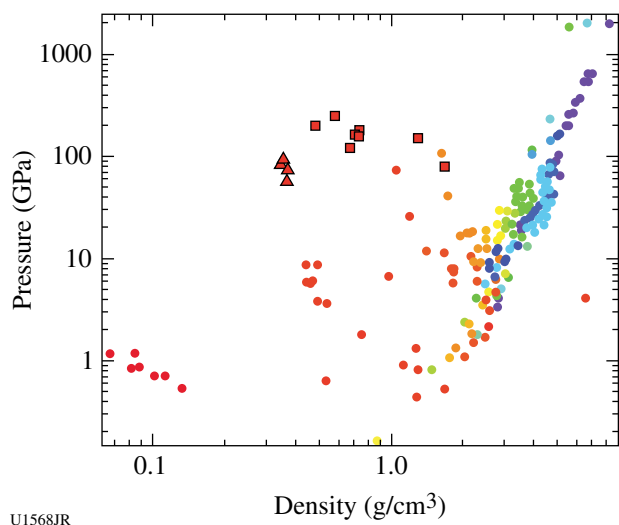


Figure 132.132

Pressure-density space of shock-compressed quartz foams.

### Advanced X-Ray Diffraction Techniques

Principal Investigator: J. Hawreliak

Since the discovery of x rays by Rontgen over a century ago, x-ray diagnostic techniques have been used to examine the macroscopic structure of samples through radiography, the atomic structure of materials through x-ray diffraction (XRD), and

electronic structure of atoms through x-ray spectroscopy. X-ray diffraction has been one of the most widely used techniques to determine a material's atomic structure. It has recently been applied to dynamic experiments where a shock or ramped pressure wave is applied to a material and then x rays are flashed in a pump–probe experiment to examine the atomic structure as the pressure wave propagates. An effort is currently underway to achieve ultrahigh pressure on laser systems using dynamic compression; in concert with this effort is the development of new advanced XRD techniques that will enable one to structurally probe the material at high pressure. This campaign was the first implementation of a technique that uses a Soller slit-like array of grids to provide limited line of sight of the detector. Figure 132.133 shows the effective geometric shielding the Soller slits provide and a sample image of the x-ray source, which is limited to a small portion of the image plate. This is part of an ongoing development project.

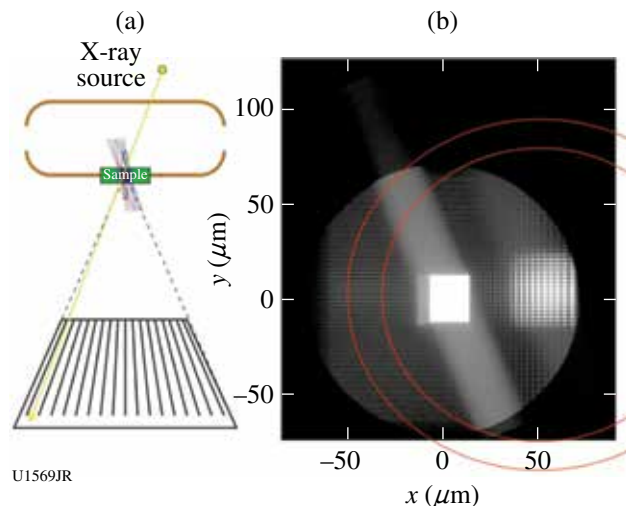


Figure 132.133

Initial data from the new Soller slit diffraction diagnostic.

## 2. Radiation Transport

### Heated Wall

Principal Investigator: K. Baker

The heated-wall campaign measured radiation transport in a geometry that enabled the heat wave to propagate as if there were no wall loss. This was accomplished by placing a thin CRF annulus around a low-density, 30-mg/cm<sup>3</sup>, SiO<sub>2</sub> cylindrical foam. One end of the SiO<sub>2</sub> foam and the outer surface of the CRF annulus were heated by the radiation environment inside a hohlraum driven by 15 OMEGA beams. The thickness of the CRF annulus was chosen such that the time-dependent position

as a function of  $Z$  of the supersonic heat wave propagating down the  $\text{SiO}_2$  cylindrical foam would match the time and  $Z$  position of the subsonic heat wave traveling radially inward through the CRF annulus and reaching the  $\text{SiO}_2$  foam from the side. In this manner the front of the supersonic heat wave traveling along the  $z$  axis of the  $\text{SiO}_2$  foam did not see a significant radial disparity in radiation temperature and consequently propagated as if it were being driven in a 1-D geometry.

The heated-wall campaign used the SXI/SSC-A (an imaging x-ray streak camera) diagnostic to measure the uniformity and breakout time of the supersonic heat wave from the rear of the  $\text{SiO}_2$  foam. The diagnostic measured breakout times consistent with simulations, including a delayed breakout of the heat wave as the density increased in the  $\text{SiO}_2$  foam. Two control experiments were performed: one with a gold disk covering the front of the  $\text{SiO}_2$  foam to block radiation from entering the  $\text{SiO}_2$  foam along the  $z$  axis; and a second in which the CRF tube was replaced with gold to prevent radiation from entering the  $\text{SiO}_2$  foam from the radial direction. The shot with a cylindrical block showed no evidence of a heat wave reaching the end of the  $\text{SiO}_2$  foam; the shots with a gold annulus to block radial transport of the hohlraum x rays into the  $\text{SiO}_2$  foam showed a delayed signal that was significantly weaker and significantly shorter temporal emission as compared to the two heated-wall shots.

### Crystal Window

Principal Investigator: B. Maddox

The CrystalWindow-12A campaign was designed to test fused silica as a VISAR window up to pressures exceeding 50 Mbar (5 TPa). Quartz had been shown to be an excellent high-pressure VISAR window at ultrahigh pressure. Although quartz blanks at low shock pressures, the shock wave in the quartz becomes reflective at higher shock pressures and can be used to measure the shock velocity transmitting into the quartz crystal. Fused silica is a noncrystalline form of silicon dioxide ( $\text{SiO}_2$ ), the crystalline form being quartz. Due to the amorphous nature of fused silica, it can be polished readily making it an ideal window material for state-of-the-art experiments on the NIF that require nonplanar VISAR witness windows. The CrystalWindow-12A campaign used the 15 H7 Cones 2 and 3 beams to drive a scale-one halfraum to 190 eV. To collect the VISAR signal, the aluminum-coated VISAR samples were attached to the open end of the halfraum and mounted on a 2.65-mm-diam gold washer with a 0.4-mm central aperture. A 2-mm-diam, 2-mm-long gold tube was also mounted on the VISAR side of the target to shield the VISAR optics from any

scattered light from the drive laser. Figure 132.134(a) depicts a photo of the completed target. Two thicknesses of aluminum were tested ( $50\ \mu\text{m}$  and  $70\ \mu\text{m}$ ) to study any blanking caused by preheating in the  $50\text{-}\mu\text{m}$ -thick Al samples. Additionally, two samples were fitted with reference quartz windows for comparison. Figure 132.134(b) shows VISAR traces for  $70\text{-}\mu\text{m}$  Al/quartz and  $70\text{-}\mu\text{m}$  Al/fused-silica window targets. The decaying velocity seen here represents the ultrahigh-pressure shock wave traveling through the quartz and fused silica. The data obtained in this campaign confirmed that fused silica works well as a VISAR window at a peak shock pressure of

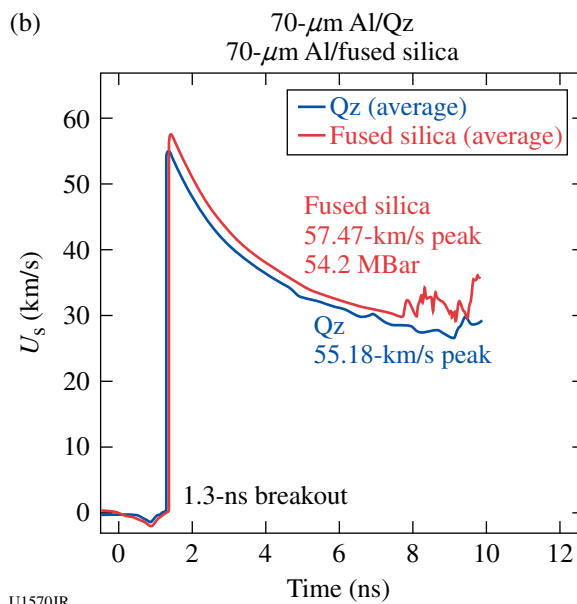
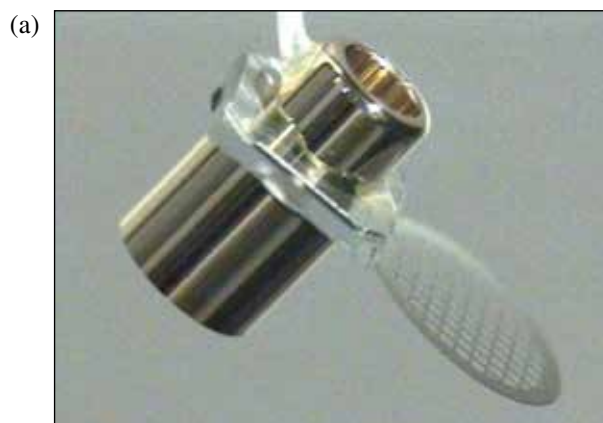


Figure 132.134

(a) CrystalWindow-12A target used to verify fused silica as a VISAR window and shock witness material to  $>50$  Mbar. (b) VISAR data confirming that fused silica works well as a VISAR window at a peak pressure of 54.2 Mbar. The velocity versus time trace represents the shock wave traveling through the fused-silica and quartz ( $Q_2$ ) windows.

54.2 Mbar with little to no blanking using a 70- $\mu\text{m}$  Al ablator. Some blanking was seen in the 50- $\mu\text{m}$  aluminum ablator targets, likely related to x-ray preheat.

### 3. High-Temperature Plasma Opacity

#### High-Temperature Plasma Opacity Experiments on OMEGA and OMEGA EP

Principal Investigator: R. F. Heeter  
 Co-investigators: A. Graf, G. V. Brown, C. Mauche, and R. E. Marrs

LLNL's high-energy-density (HED) opacity research on OMEGA in FY12 had three main directions: First, the MBOP-12 campaign followed up on physics questions from the very successful 2009–2011 Ti opacity shots, where the observed Ti continuum opacity and one to three line opacity regions did not match code expectations. New data obtained with a modified hohlraum design indicated that up to that 50% higher sample temperature was achieved.

The second campaign, NLTE-Dynamics-12, continued previous work on the non-LTE x-ray emission properties of hot high-Z plasmas as found in hohlraums at the laser-driven "hot spots."

Uranium was chosen as the sample material because of its use on ignition and other shots on the NIF and also the paucity of experimental data. Shots performed in FY12 extended earlier work on uranium emission to 2 $\times$  lower intensity (material temperature) and the data are now being compared with simulations.

The third research direction was the EPOp-12 series, which substantially upgraded the novel short-pulse "absorption-emission" opacity platform developed on OMEGA EP in FY10–FY11. The new platform uses a sample driven with up to 200 J via 100-ps FWHM Gaussian UV laser pulses using two of the "long-pulse" beams on OMEGA EP. The two short-pulse beams deliver up to 1500 J in 10 ps to a pair of continuum x-ray backlighters that probe the plasma after some delay. Figure 132.135 shows the first face-on transmission spectrum obtained from this new platform using a silicon sample and a probe beam delayed about 300 ps. Multiple L-shell charge states are observed in absorption. Self-emission from helium- and hydrogen-like silicon (produced prior to the backlighter probe but recorded on the time-integrated detector) is also observed. The presence of the Be-like and Li-like ions implies that this new platform achieves temperatures similar to those observed with the single-backlighter platform and titanium samples in FY11.

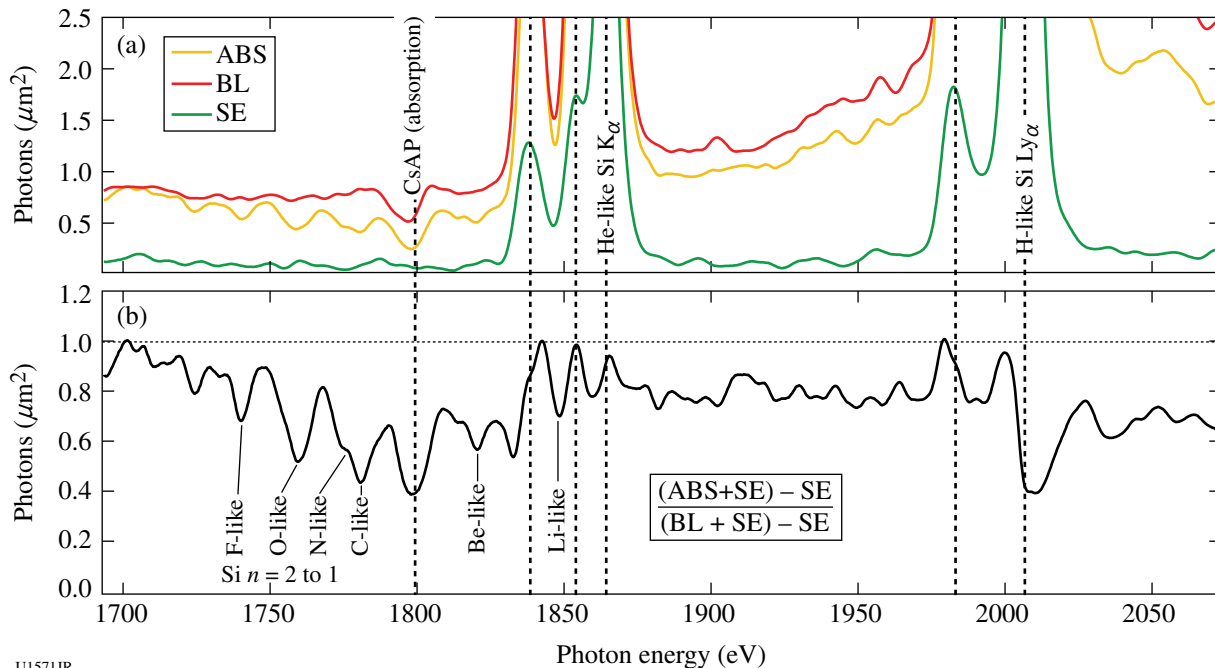


Figure 132.135 Initial silicon opacity spectra from OMEGA EP. (a) Backlighter, sample absorption, and sample self-emission spectra recorded on Biomax film; (b) sample transmission.

#### 4. Burn Physics

##### ***Non-LTE Transport and Nuclear Lifetimes***

Principal Investigator: A. Kritcher

Plasma coupling to nuclei in high-energy-density plasmas, or *nuclear-plasma* physics, is a cutting-edge field that traverses the areas of nuclear physics, plasma physics, and atomic physics. Nuclear-plasma interactions occur in hot dense plasmas such as inertial confinement fusion (ICF) environments and astrophysical bodies. The effect of high-energy-density-plasma (HEDP) environments on astrophysical nucleosynthesis—the formation of heavy elements from pre-existing nucleons in astrophysical plasmas—is expected to play a significant role.<sup>48</sup> Nuclei in stellar plasmas reach a thermal population of low-lying excited nuclear states from photoexcitation, free electrons in the plasma (NEEC),<sup>49–52</sup> excitation from atomic transitions (NEET),<sup>53–55</sup> and inelastic electron scattering in the dense plasma. In these experiments at the Omega Laser Facility we investigate the NEEC process in underdense plasmas by illuminating mini hot hohlraums (400 or 600  $\mu\text{m}$  in diameter) with  $\sim 15$  kJ of laser light.

The goal of these first experiments was to identify the plasma conditions of hot Tm hohlraums with spectral line emission analysis and optical Thomson scattering, measure the energy and time-resolved atomic emission background, investigate this experimental platform to study nuclear lifetime shortening in hot plasmas, and determine the possibility of investigating nuclear-plasma interactions on OMEGA. In these first experiments we have collected high-quality data and are in the process of analyzing the results. Future campaigns will continue to measure plasma conditions of hot hohlraums and investigate nuclear-plasma interactions in HEDP plasma environments. We will also field additional isotopes in this configuration.

#### 5. Hydrodynamics

##### ***Short-Pulse, UV Backlighting Development for the NIF***

Principal Investigator: V. A. Smalyuk

High-energy-density complex hydrodynamics experiments on the NIF require short-pulse backlighting capability. Experiments on OMEGA EP tested the short-pulse, UV beam backlighting concept for the NIF. Four OMEGA EP beams were focused onto 10- $\mu\text{m}$ -thick Ag wires, mounted on 300  $\times$  300- $\mu\text{m}$ -sq, 10- $\mu\text{m}$ -thick polyimide foils to mimic the illumination conditions of one quad on the NIF. The total laser energy was  $\sim 400$  J with an  $\sim 100$ -ps Gaussian pulse shape, a peak laser intensity of  $\sim 3 \times 10^{16}$  W/cm<sup>2</sup>, and a mispointing of  $< 50$ - $\mu\text{m}$

rms. Three beams were co-timed while the fourth beam was advanced up to 300 ps from the co-timed beams to maximize the x-ray backlighter signal. Results were compared with  $\sim 1.2$ -kJ short-pulse ( $\sim 100$ -ps) IR beam backlighting with the same Ag-wire targets, driven at an intensity of  $\sim 1 \times 10^{17}$  W/cm<sup>2</sup>. Figure 132.136 shows a measured image of the target, created with Ag-wire backlighting on an image plate using a high-energy radiography imager for EP (HERIE) diagnostic located 50 cm from target chamber center on OMEGA EP. The configuration consists of a Au grid to determine magnification, a 100- $\mu\text{m}$ -thick Au plate to determine resolution, and seven Cu steps with 18- $\mu\text{m}$  thickness between adjacent steps to determine contrast and sensitivity. Areas inside and outside the Au plate were also used to measure noise. Figure 132.137 shows the change in the intensity across the Cu step wedge. The 300-ps advance produced the brightest signal, while a 150-ps advance produced nominally the same results as all four beams co-timed. The  $\sim 20$ - $\mu\text{m}$  spatial resolution was similar to IR-beam experiments, while the signal was  $\sim 100\times$  lower. The short-pulse UV backlighting might be feasible for complex hydrodynamics experiments on the NIF if hohlraum and backlighter x-ray backgrounds do not exceed  $\sim 10$  PSL (photostimulated luminescence) on the image plate at 50 cm from the NIF target chamber center.

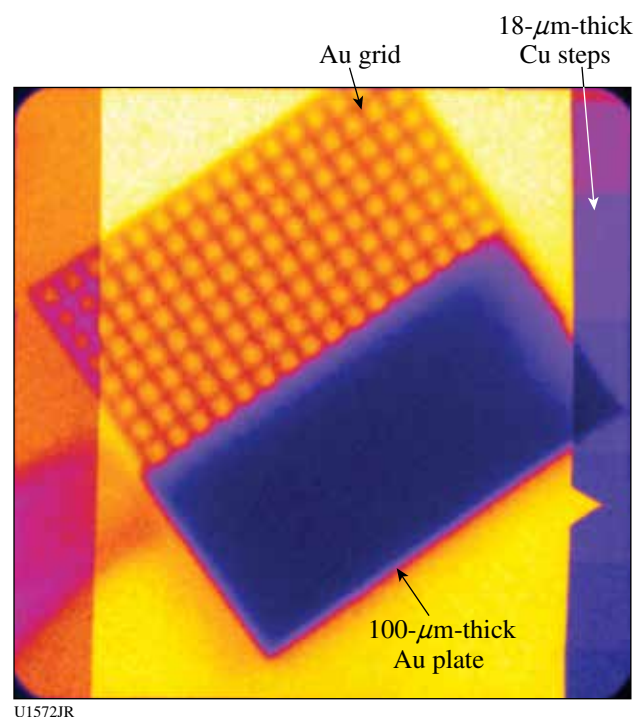


Figure 132.136  
X-ray radiograph of the target consisting of an Au grid, a 100- $\mu\text{m}$ -thick Au plate, and seven 17- $\mu\text{m}$ -thick Cu steps.

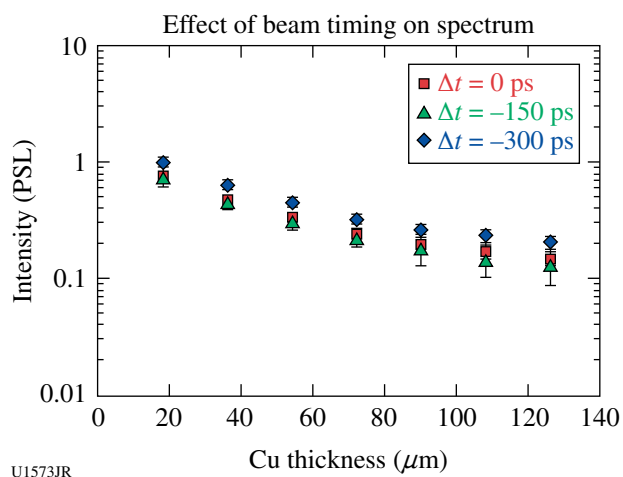


Figure 132.137

Intensity across the step wedge shows relative differences in backlighter emission. A 300-ps advance in beam timing shows a small increase in signal. Uncertainties illustrate shot-to-shot variation.

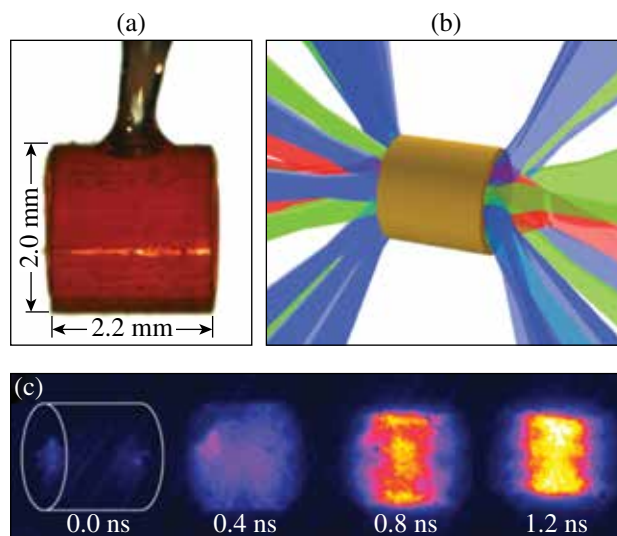
## 6. X-Ray Source Development and Application

### *X-Ray Source Development with Nanostructured Materials*

Principal Investigator: R. Patterson

Progress in the fabrication of new metallic aerogels for x-ray generation<sup>94</sup> led to a campaign for optimizing titanium x-ray sources, as illustrated in Fig. 132.138. Experiments were conducted in FY12 by the X-Ray Source Development team in collaboration with the Defense Threat Reduction Agency and researchers from Commissariat à l'Énergie Atomique (CEA). In the FY12 shots, when irradiated by 40 OMEGA beams, Ti-doped aerogels (4 mg/cm<sup>3</sup>, 4 at. % of Ti) made by a wet-chemistry process yielded only a 0.7% laser-to-x-ray conversion efficiency (CE) in the x-ray band between 4.6 and 5 keV, which is significantly lower than the previous record of 3% CE (Ref. 95). However, in this campaign novel aerogels were measured to provide a 5.5% CE in the same energy range. These new targets were made by coating SiO<sub>2</sub> aerogel templates with TiO<sub>2</sub>. They are of similar ultralow density (4 mg/cm<sup>3</sup>) but reach a higher Ti concentration (22 at. %).

Current analysis is focused on precise understanding of the x-ray spectra, which will bring interesting new insights to our understanding of the heating of these targets. Analysis will also cover the heating dynamics<sup>96,97</sup> and yield optimization of these targets using hydrodynamic simulations. The objective is to design future targets by optimizing the Ti concentration and aerogel pore size, which are now controllable.



U1574JR

Figure 132.138

(a) Photograph of a cylindrical aerogel target held inside a thin plastic tube. (b) Irradiation structure from 40 OMEGA beams. (c) Example of x-ray emission images at different times relative to the beginning of the interaction.

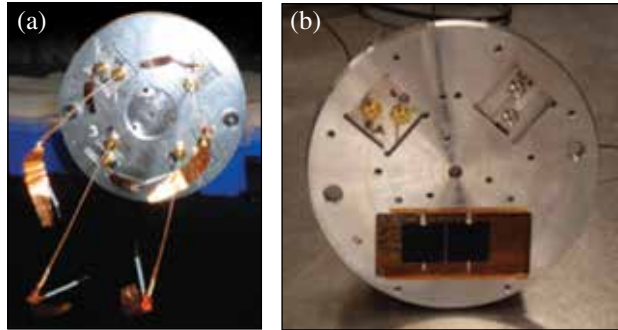
### *Solar Cell Electrostatic Discharge*

Principal Investigator: R. Patterson

During FY12, the X-Ray Source Development team, in collaboration with the Naval Research Laboratory and the Defense Threat Reduction Agency, conducted a series of experiments to examine the effects of x-ray loading on solar cells. Our tests were broken into two parts: We first evaluated the ability of the Omega facility to produce a laboratory environment suitable for conducting electrostatic discharge experiments on solar cells; then we subsequently conducted the first tests of active solar cell arrays. For each of these experiments, Fe- or Ge-based targets positioned at the center of the target chamber were irradiated with ~20 kJ in a 1-ns square pulse. The XRSA Langmuir Probe Diagnostic (XLDP) or a modification including active solar cells was positioned a few tens of cm from the target.

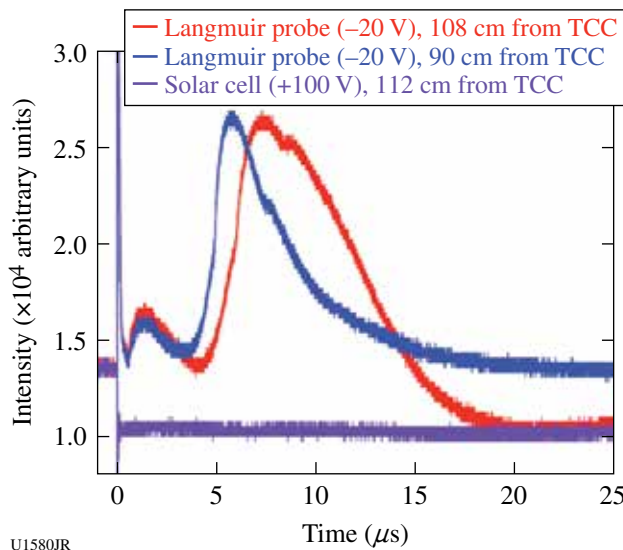
Building on initial tests in the previous year, we deployed XLDP configured as an array of eight cylindrical Langmuir probes [Fig. 132.139(a)] on 29 February 2012 to observe the arrival of the source plasma. Time-of-flight measurements resulted in an observed velocity of  $\sim 16 \pm 2$  cm/ $\mu$ s for the leading edge of the source plasma.<sup>98</sup> Based on these measurements, we concluded that the OMEGA target chamber is suitable for conducting electrostatic discharge experiments on solar cells, provided that the cells are positioned sufficiently far from the target.

On 12 September 2012 we did indeed place an array of two solar cells along with four standard XLPD probes [Fig. 132.139(b)] a minimum of 40 cm from target chamber center to examine the response of these cells to the x-ray and plasma environment produced from Ge-aerogel targets. Figure 132.140 shows the prompt x-ray response of the probes as well as the solar cells. In addition, the Langmuir probes show



U1575JR

Figure 132.139 (a) An XLPD cassette with four pairs of Langmuir probes. Each pair is composed of one 2.5-cm and one 20-cm probe. (b) Modification of XLPD to include an active solar cell array. Two  $2 \times 2$ -cm Ge triple-junction solar cells are biased up to 100 V and can be fielded with up to two pairs of standard XLPD Langmuir probes.



U1580JR

Figure 132.140 Initial results from the solar cell discharge experiments. Signals from two ion-collecting probes are shown in addition to the signal recorded from a solar cell biased at 100 V.

signals consistent with sheath formation in the first 200 ns, followed by the arrival of charged particles from the target. While our analysis of the solar cell data is ongoing, the data are consistent with an electrostatic discharge, perhaps caused by current flowing to ground through the dense plasma formed from the ablation of the XLPD cassette itself. In future experiments, we will insulate the solar cells from the chassis in order to test the potential arc formation between cells.

**ACKNOWLEDGMENT**

This work was performed under the auspices of the U.S. Department of Energy by Lawrence Livermore National Laboratory under Contract DE-AC52-07NA27344.

**FY12 LANL Experimental Campaigns—Overview**

In FY12, Los Alamos National Laboratory (LANL) executed 244 total shots on OMEGA. LANL experiments contributed to the National Ignition campaign (NIC) in the following ways:

- Measured the x-ray ablative Richtmyer–Meshkov growth of isolated defects on plastic ablators
- Studied branching ratios in DT fusion plasmas
- Continued neutron imaging and radchem scintillator development for the NIF

**High-energy-density (HED) campaigns included**

- Study of shear in a counter-propagating flow geometry and reshock-driven turbulent mixing
- Backlit defect implosion experiments to study the effect of trench defect and polar drive
- Measurement of the effect of capsule asymmetries on neutron yield and ion temperature
- Imaging x-ray Thomson-scattering platform development for dense plasmas and warm dense matter equation of state (EOS)
- Measurement of a supersonic radiation wave and foam aerogel EOS

**CHaRM**

The CH ablative Richtmyer–Meshkov (CHaRM) campaign had two shot days in FY12. The goal of these experiments was to measure the oscillation frequency of small perturbations on CH ablators driven by the x-ray–ablation Richtmyer–Meshkov effect. With this knowledge we would have a better understanding of how isolated defects behave during the first shock transit stage of a NIF ignition attempt, which could then provide methods for minimizing perturbations at the onset of Rayleigh–Taylor.

Our experiments used 15 beams inside large Au half-hohlraums, which were staggered in time to produce a 7.5-ns radiation drive with a radiation temperature of 70 eV (see Fig. 132.141). Targets with 2-D arrays of 5- $\mu\text{m}$ -tall, 17- $\mu\text{m}$  FWHM Gaussian bumps were attached over the opposite laser entrance hole with the defects facing inside the halfraum. During the experiment the bump arrays were backlit with Y and Ta backlighters ( $\sim 2.2\text{-keV}$  emission) and imaged at 37 $\times$  magnification into an x-ray framing camera.

Radiation-hydrodynamics simulations running with EOS tables for CH predict that these small bumps decay for our experimental conditions as shown in Fig. 132.142 (green curve). The trend in our data supports this prediction even though the

data lie somewhat above the simulation curve, which we think is due to either systematic errors in the data analysis or errors in the models. Nevertheless, this decay in amplitude occurs at a rate that is much slower than under direct-drive conditions measured at Naval Research Laboratory (NRL). This has to do with the differences in absorption, transport, and ablation mechanisms between x-ray and laser drives. Under our conditions only very narrow bumps ( $< 20\ \mu\text{m}$ ) exhibited this decay while wider bumps ( $> 30\ \mu\text{m}$ , FY11 data) only saturated.

**Shear**

In FY12 the Shear campaign focused on developing a counter-propagating flow platform for studying shear-driven turbulent mixing. These experiments use Be tubes containing

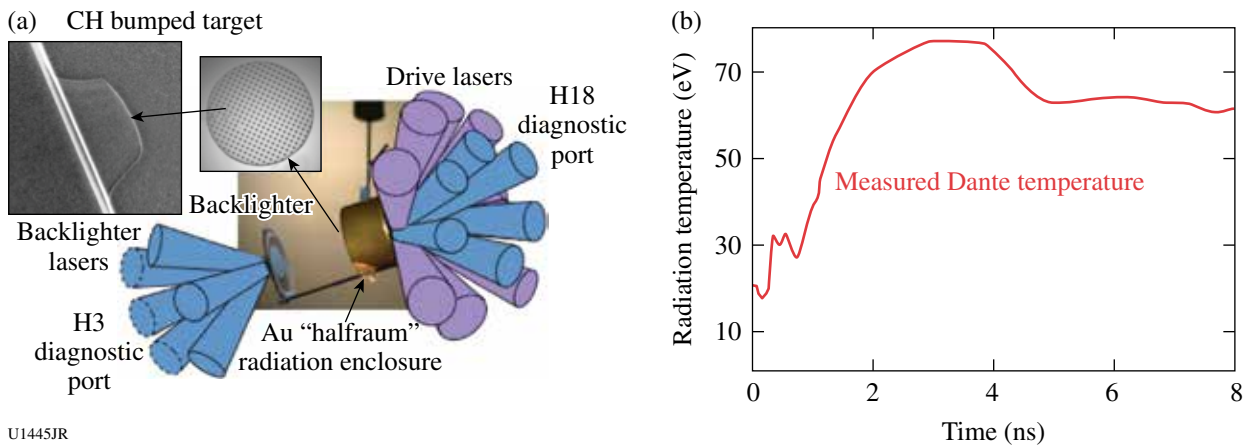


Figure 132.141

(a) Schematic of the CHaRM platform where a Au halfraum is heated to 70 eV, driving an ablation front into an array of isolated Gaussian bump defects. (b) Bumps are radiographed along the axis of the halfraum.

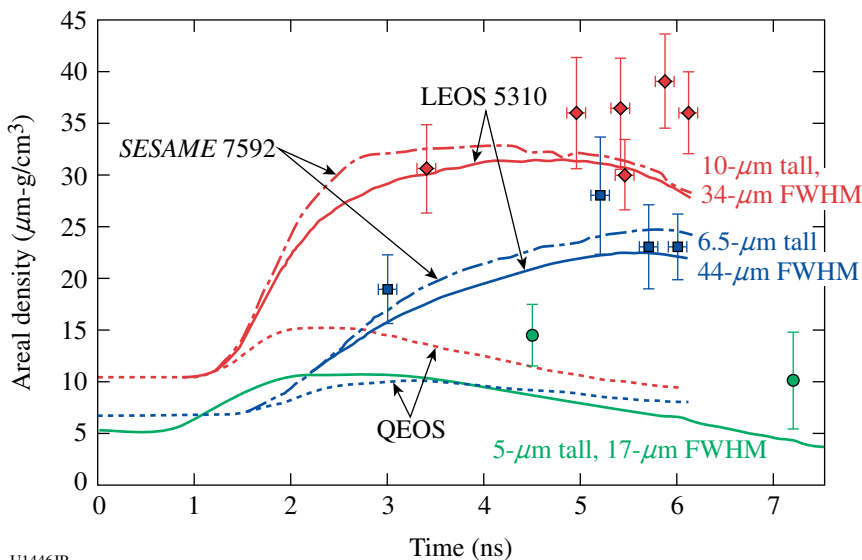


Figure 132.142

Summary of long drive duration data showing the saturation of bumps with  $> 30\text{-}\mu\text{m}$  width and ablative RM decay for those with widths  $< 20\ \mu\text{m}$ .

U1446JR

low-density CH foam semi-cylinders separated by Al tracer layers. The counter-propagating flow is created by inserting Au “plugs” in front of each foam semi-cylinder at opposite ends to hold back the shock in each foam at one end (see Fig. 132.143). With the plugs in place, the Be tube ends are irradiated with  $10^{15}$ -W/cm<sup>2</sup> laser intensity to initiate the counter-propagating flow. When the shocks cross, they establish a shear layer in the Al, which then grows due to turbulent mixing.

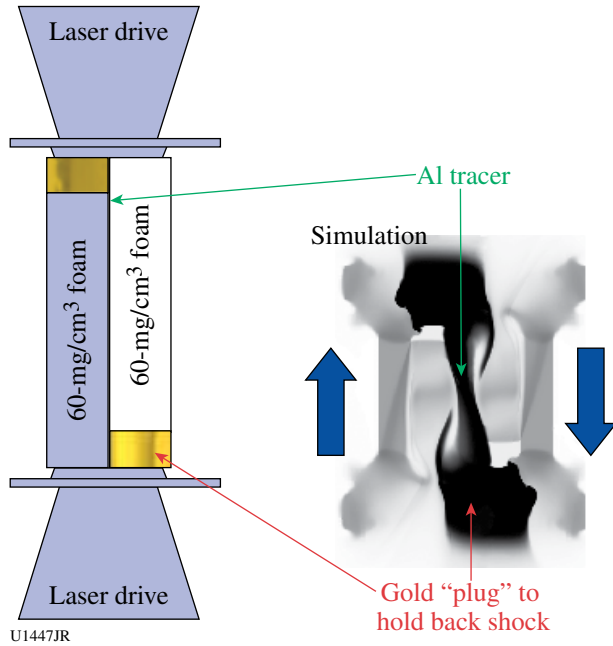


Figure 132.143  
Geometry for a counter-flowing shear platform. Simulations with the Besnard–Harlow–Rauenzahn (BHR) mix model are also shown.

Over the course of the year, we improved the target design by extending the length of the Al tracer so that shocks from one end could not penetrate into the adjacent foam. This created a longer-duration, cleaner shear flow for studying the turbulence. We used x-ray radiography along two orthogonal lines of sight (edge-on and plan view of the tracer layer) to image the evolving turbulent structure at  $>20\times$  magnification. In the edge-on view (see Fig. 132.144) the growing mix layer was imaged at times from 6 to 16 ns and in relatively good agreement with the LANL Besnard–Harlow–Rauenzahn (BHR) turbulent mix model. The same data times were used (on the same shot) for the plan view radiography, which appears to show a transition to turbulence around the 10-ns point where 3-D structures begin to form out of the initially homogeneous flow.

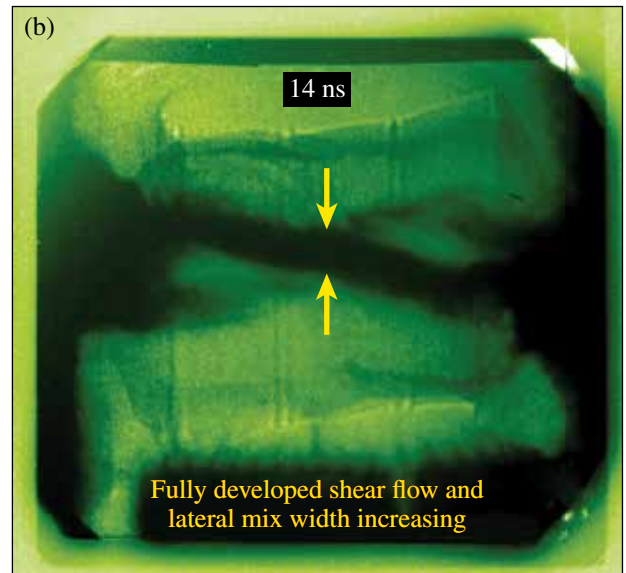
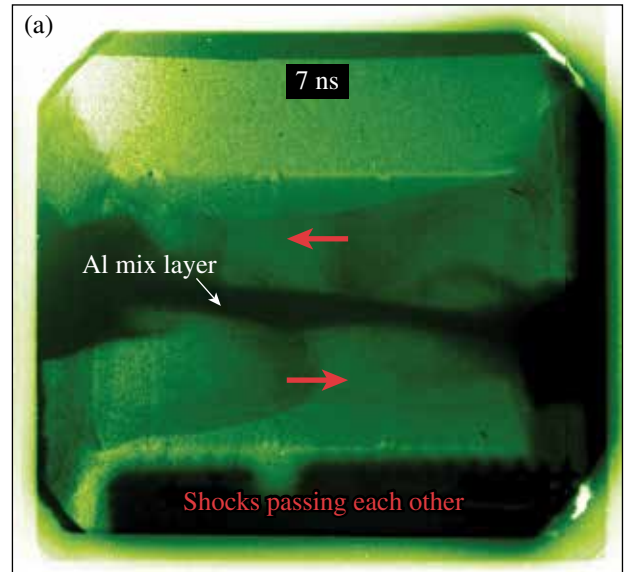


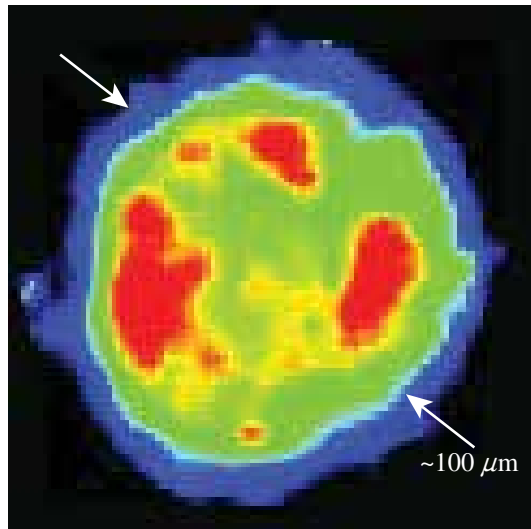
Figure 132.144  
Radiographs at two different times showing development of counter-flowing shear and mixing.

### ABEX

In laser-driven implosions, of importance to inertial confinement fusion and stockpile stewardship, the cold shell is known to mix into imploding nuclear fuel. Yet there are no direct observations of just where, and at what rate, shell material migrates into the fuel. In June 2012 experiments at the Omega Laser Facility, LANL’s ABEX (asymmetric burn experiment) campaign, in collaboration with Prof. Roberto Mancini’s University of Nevada, Reno group, has made advances toward providing time-resolved images of shell mix into fuel. Emission from titanium dopant in the shell is used to make quasi-

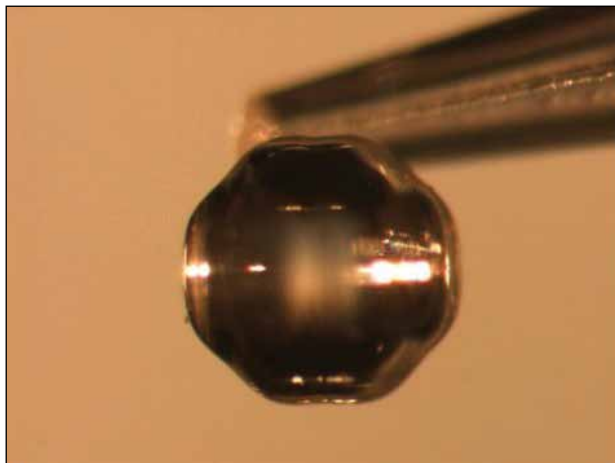
monochromatic images. Temperature, and ultimately a crude estimate of chord-integrated titanium, has been extracted (see Fig. 132.145). Three such separate views, each at multiple times, were obtained during each shot.

A capsule with pre-imposed perturbations (Fig. 132.146) showed images similar to those obtained with perfect spheres—but to just what depth the Ti has penetrated remains ambiguous. The team is now focused on advanced analysis and refinement



U1449JR

Figure 132.145  
Ti originally in the shell has mixed into the fuel (typical false-color map is used, i.e., red corresponds to an increased signal).



U1450JR

Figure 132.146  
Photograph of a machined PAMS mandrel with  $\pm 10$ -mm-amplitude perturbation. The axis of symmetry is horizontal in this photograph.

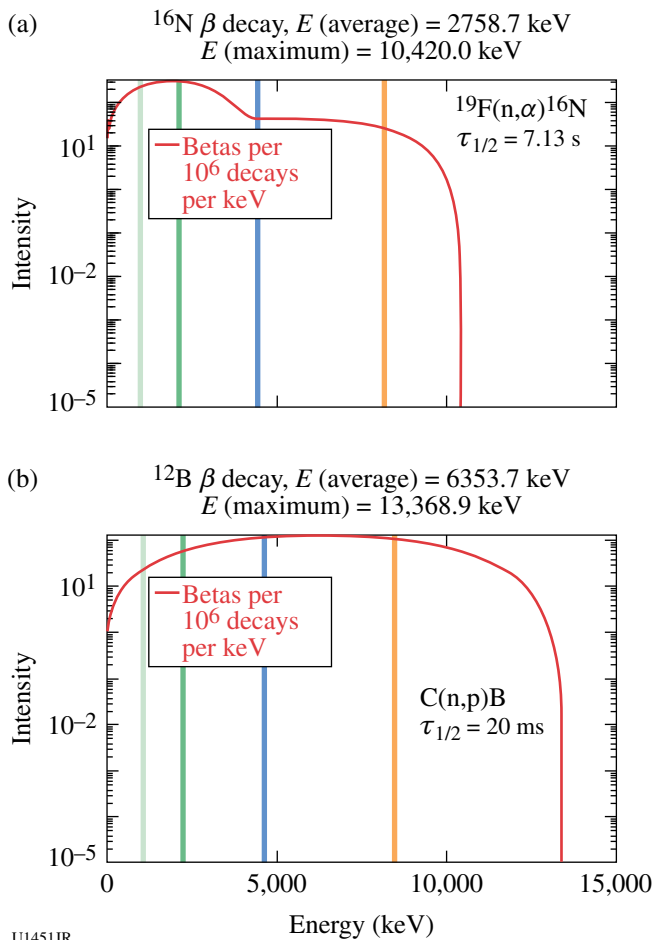
of the target design to address the longstanding absence of mix images in laser-driven implosions.

### RadChem

On 6 August 2012, the LANL Prompt Radchem Development team successfully tested new assay system designs on the OMEGA laser. Prompt radiochemical signatures generated in high-energy-density experiments provide insight into a variety of physical phenomena including late-time hydrodynamic performance of the implosion as well as particle stopping within the plasma. These signatures are created through charged- and neutral-particle nuclear interactions within the imploded capsule materials. Often the resulting radioactive products undergo beta decay with end-point kinetic energies approaching 14 MeV and half-lives as short as 20 ms. The short half-lives necessitate deploying an assay system within the target chamber that will withstand the harsh, prompt radiation environment but will readily assay the high end-point energy beta decays that immediately follow. Furthermore, the detector must have minimal sensitivity to the flux generated by background sources.

During the August campaign, the LANL-based team fielded a new four-element scintillator telescope to measure beta decay from various elements with different end-point energies ranging from 3 MeV up to 14 MeV and half-lives from 20 ms to several minutes. Figure 132.147 illustrates the strategy employed by the detector. The red curves represent the electron spectrum expected from decays of  $^{16}\text{N}$  and  $^{9,10}\text{B}$ . The colored vertical lines approximately represent the threshold sensitivity of the individual elements within the telescope detector, e.g., the first element will register hits from electrons above  $\sim 1$  MeV, the second above  $\sim 2$  MeV, etc. By requiring a coincidence between the elements of the telescope detector, not only is the background flux outside the solid angle of the detector acceptance reduced, but a threshold cut is placed on the electrons depositing energy within the telescope.

To test these concepts, the detector was fielded in the OMEGA target chamber during a set of high-yield implosions of DT-filled glass and plastic capsules. Activation targets, including a polytetrafluoroethylene (Teflon) puck, were located in front of the telescope yielding the data shown in Fig. 132.148. Figure 132.148(a) shows the coincidence rate of the first two scintillator elements shortly after a shot. A fit to the distribution clearly shows half-life contributions from  $^{16}\text{N}$  and  $^{19}\text{O}$  decays, as expected from  $^{19}\text{F}(n,\alpha)^{16}\text{N}$ , and  $^{19}\text{F}(n,p)^{19}\text{O}$  reactions. Figure 132.148(b) shows the coincidence rate using the first three elements, thereby requiring a  $\sim 5$ -MeV threshold. This higher threshold eliminates the  $^{19}\text{O}$  contribution and significantly



U1451JR

Figure 132.147  
 Beta-decay spectrum with approximate detector element thresholds. (a)  $^{16}\text{N}$  beta spectrum and (b)  $^{9,10}\text{B}$  beta spectrum.

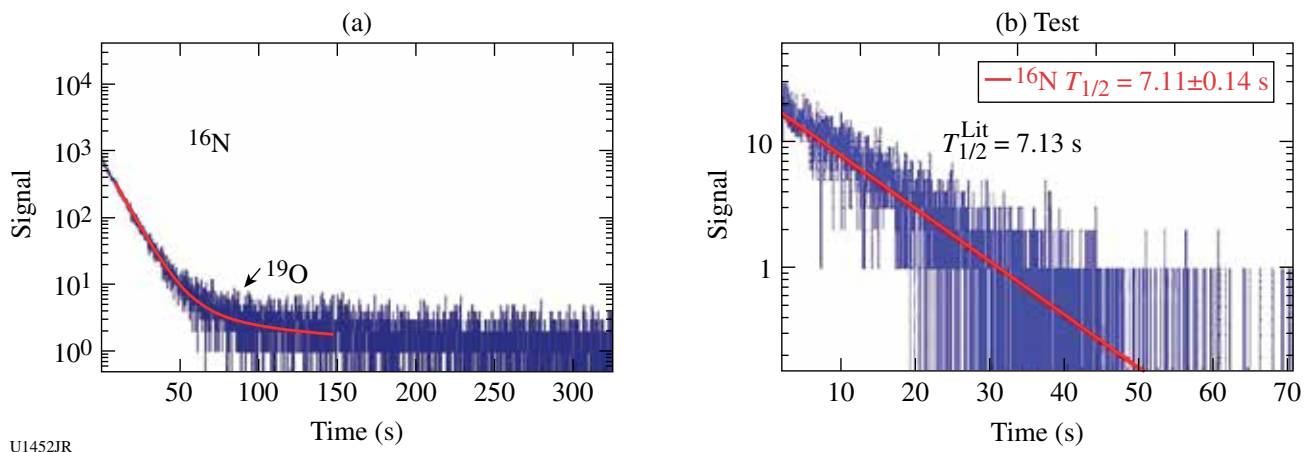
reduces the  $^{16}\text{N}$  to the lower-intensity, higher-energy decay. The fit shown in Fig. 132.148(b), using an exponential and no background, gives a half-life measurement of  $\tau_{1/2}(^{16}\text{N}) = 7.11 \pm 0.14$  s, in excellent agreement with the published value of 7.13 s.

In future experiments planned at the Omega Facility, the telescope will be moved closer to the imploding capsule to test the robustness of the detector to prompt radiation, as well as to provide the opportunity for other activation measurements.

**DPEOS**

The purpose of the DPEOS project is to measure the EOS of material in the warm dense matter regime. To accomplish this, we are developing an experimental platform to do this at the Omega Facility. Our experimental platform uses the OMEGA laser to drive a very strong shock into an aluminum or graphite sample. The shock is then released into a 0.2-g/cm<sup>3</sup> aerogel foam that is used as a pressure standard. A shock-breakout measurement is used to determine the shock velocity and pressure in the foam. We have also developed an imaging x-ray Thomson spectrometer to measure Compton-scattered x rays from the released sample. This information can be used to determine the temperature and density of the released material, providing the necessary measurements to determine the EOS.

Our experimental plan for FY12 was to test and measure the shock and release conditions produced in the aluminum sample, get our new imaging x-ray Thomson spectrometer (IXTS) approved, test its operation, and obtain the first x-ray scattering measurements of WDM aluminum and/or carbon.



U1452JR

Figure 132.148  
 Prompt decay data from a high-yield OMEGA implosion. (a) Two-element coincidence rate and (b) three-element coincidence rate.

We were successful in reaching these goals. We completed a total of 24 shots in two days on OMEGA. On the first day, we successfully fielded the IXTS for the first time and obtained scattering data. However, our signals were contaminated by background x-ray signals from our x-ray backlighter. Our shielding and target design were improved for the second shot day in August, and we obtained our first detailed x-ray scattering measurements from warm dense matter carbon. These measurements enabled us to determine the temperature of the shock and released carbon. In addition, we verified the shock conditions for both carbon and aluminum, which were consistent with our previous measurements. An example of the IXTS data we obtained is shown in Fig. 132.149. This figure contains the analyzed x-ray scattering signal along with a series of fits to the data. Two shot days are planned for FY13 in which we will perfect our target design to obtain better signal to noise for this data and in addition will carry out x-ray radiography measurements to pin down the density of the material. This will provide a complete EOS measurement for these warm dense matter conditions and be used to test EOS models in this regime.

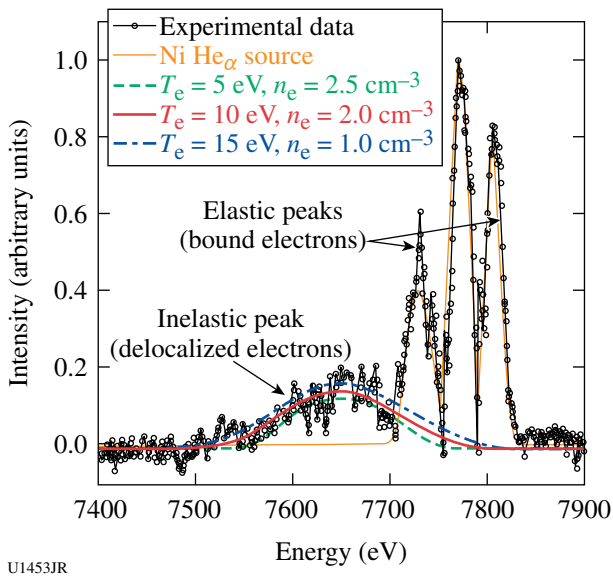


Figure 132.149 X-ray Thomson-scattering measurements from shock and a released warm dense matter graphite target. The elastic peaks correspond to scattering from bound electrons while the inelastic peak is due to scattering from free electrons. The measurements indicate a temperature of ~10 eV and density near 2 g/cm<sup>-3</sup>.

**NIF-5**

The purpose of the NIF-5 project is to test both diagnostics and physics ideas that are important for facilitating our

understanding of important radiation flow experiments being carried out on the NIF. In the past, this project has focused significantly on diagnostic development and testing and experimental platform development. This fiscal year we changed the focus of the project to address an important physics issue for these experiments, namely the EOS of the foams used in these experiments. Foams sometimes exhibit significantly different material behavior than normal materials, both in their response to shocks and in their relatively high specific heats at moderate energy density.

To address these concerns, we carried out two days of experiments and a total of 28 shots on OMEGA in FY12. These experiments built on the platform development of other shock physics experiments on OMEGA, including target geometries and diagnostics. This immediately enabled us to be relatively successful. Our specific purpose for these experiments was to measure the temperature of shocked aerogel foam in the few-Mbar range. The foam would have an initial density of 0.2 g/cm<sup>-3</sup>, which has the advantage that the principal Hugoniot for this foam is well known, requiring only a measurement of the shock velocity to determine the state. We were very successful obtaining both good shock-velocity measurements and streaked optical pyrometer (SOP) measurements for a wide range of pressures. A brief analysis of the shock velocity and SOP data is given in Fig. 132.150. We found that the temperature dependence on the shock velocity was weak for a wide range of shock velocities, indicating a very high specific heat and also indicating the

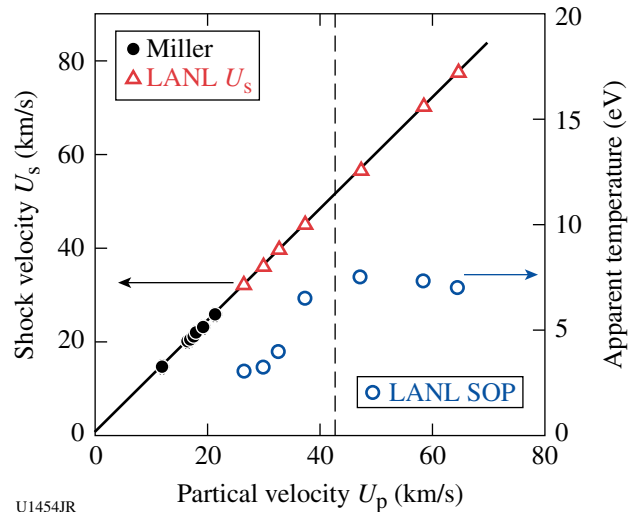


Figure 132.150 Temperature and shock-velocity measurements for 0.2-g/cm<sup>-3</sup> aerogel foam targets. The straight line fit is based on Hugoniot measurements for this foam and the vertical dashed line corresponds to a pressure of ~4.4 Mbar.

important energy density range where ionization and dissociation occur. We also see a saturation of the SOP temperature at higher shock pressures. We believe either a limitation of the diagnostic or more likely radiative heating at the shock front is confusing the measurement. Since the two shot days were quite close together, few modifications were made to the target design, so this effect could not really be further investigated. We expect to learn more about this effect through a series of double-shock experiments to be carried out in FY13.

**DTRat**

On 9 August 2012, LANL's ICF Gamma Ray Physics team conducted ongoing DT Ratio Campaign experiments on OMEGA. Y. Kim and H. Herrmann led the collaborative effort including participation from LLNL, AWE, MIT, Colorado School of Mines, Cornell, and LLE. The capsules consisted of D<sup>3</sup>He, <sup>3</sup>He<sup>3</sup>He, and DT fills for the primary purpose of characterizing the D<sup>3</sup>He  $\gamma$ -ray spectrum. D<sup>3</sup>He  $\gamma$ -ray measurements have been used by Kim *et al.*<sup>99</sup> as a cross-calibration for the recently published DT gamma-to-neutron branching ratio (BR) inference under the assumption that <sup>5</sup>He from DT and mirror nucleus <sup>5</sup>Li from D<sup>3</sup>He generate virtually identical  $\gamma$ -ray spectra. This shot day was intended to test this assumption.

Figure 132.151 shows preliminary data taken by the gas Cherenkov detector (GCD) during a Cherenkov threshold scan indicating that, as expected, the primary peak from D-<sup>3</sup>He fusion gammas decreases with an increasing energy threshold. More-quantitative analysis is awaiting the results of CR-39-

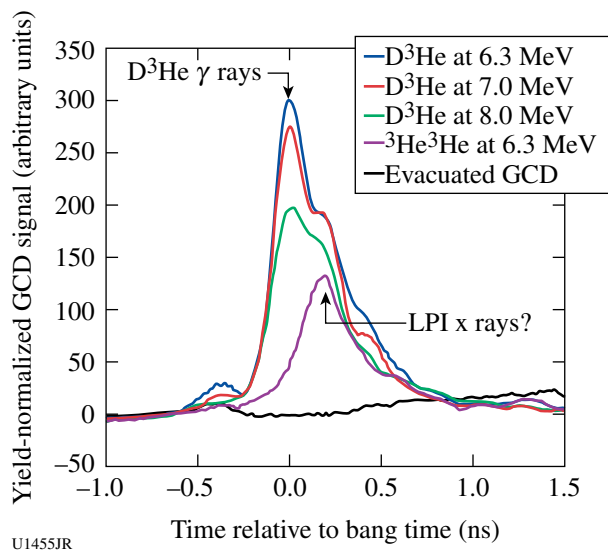


Figure 132.151  
Data from the GCD showing fusion gamma decreasing with an increasing energy threshold.

based proton-yield measurements. One interesting feature, however, is what appears to be a secondary peak (~0.2 ns) that is not reduced as readily by thresholding, implying that it is from photons of higher energy than the 16.6 MeV D-<sup>3</sup>He fusion gammas. The peak remains when the capsules contain no D (i.e., <sup>3</sup>He-<sup>3</sup>He implosions). Since there is no expectation of a fusion gamma from the unbound and therefore extremely short-lived <sup>6</sup>Be, the current speculation is that this peak is the result of extremely high energy laser-plasma instability (LPI) x rays (>20 MeV) coming from the two-plasmon instability. This mechanism is known to be amplified for thin-walled glass capsules in which fusion bang time occurs before the end of the laser pulse. Over the past two years we have observed that this secondary peak becomes more pronounced with capsule thinness. It is now clear that this secondary peak must be accounted for when measuring the D-<sup>3</sup>He gamma yield and cross-calibrating D-T  $\gamma$ /n BR to D-<sup>3</sup>He  $\gamma$ /p BR. Doing so will result in making the cross-calibrated BR value more consistent with the previously determined absolute BR value published in Y. H. Kim *et al.*<sup>100</sup> This discovery may also lead to greater insight into LPI mechanisms leading to ultrahot electrons having deleterious effects on ignition.

**DIME**

The DIME campaign had two shot days in 2012 on OMEGA. On the first of the shot day, we used symmetric 60-beam illumination with ~800- $\mu$ m-spot phase-plate smoothing for 1 ns to drive spherical implosions. The objective was to measure the mix depth of an embedded Ti layer (1% by atom) in the spherical capsule wall. The variable was the separation of the 2- $\mu$ m impurity layer from the inner wall of the 435- $\mu$ m-radius capsule for the ten targets. The embedded depth was 0.0, 1.4, 3.0, or 4.8  $\mu$ m. The 19- $\mu$ m wall thickness was sufficient to prevent burnthrough by the laser drive. Therefore, we collected data for the 4 $\pi$  mix. A first look at normalized data is shown in Fig. 132.152.

Neutron yield data were provided by V. Yu. Glebov (LLE). B. Yaakobi (LLE) facilitated the spectral analysis of the Ti K $\alpha$  absorption feature and Ti line emission from the x-ray spectrographic data. One calculates the  $\rho R$  of Ti from the transmission  $T$  of the continuum at 4.5 keV:  $\rho R = -\ln T/\sigma$ , where  $\sigma$  is the x-ray attenuation coefficient (cm<sup>2</sup>/gm) of cold Ti. The line emission of Ti, heated by mix with the hot deuterium fill gas, peaks at zero depth and damps quickly with burial depth, thereby corroborating this picture of mix. The curved lines are to "guide the eye." The anticorrelation between yield and the Ti spectral data, which indicates a mix depth of ~1.5  $\mu$ m, is consistent with expectations. A similar campaign, identical in

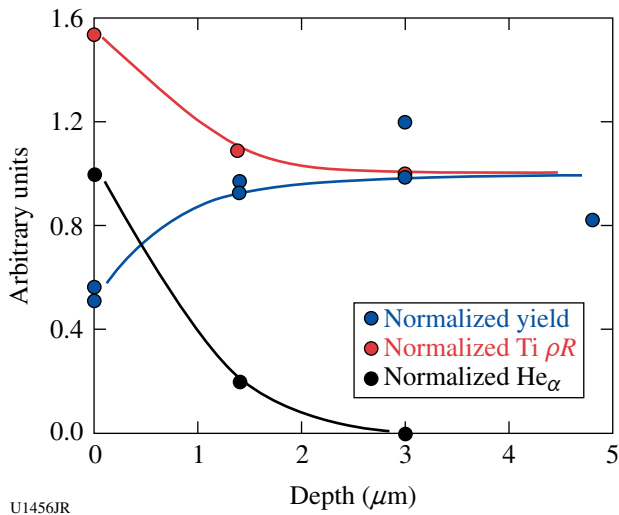


Figure 132.152  
Correlation of mix parameters for the 60-beam drive.

every respect for targets, was executed for polar direct drive (PDD) later in the year. The objective for this campaign was to assess how PDD altered the mix depth and the spatial variations inherent with PDD. Steps in the inner CH wall layer were smaller. Data analysis is pending.

**Colliding Shock**

The LANL Colliding Shock Campaign had nearly 30 shots on OMEGA in November 2011 and March and July 2012. Radiographs of the colliding shocks were obtained on two cameras looking on orthogonal axes and at 2-ns delays with respect to each other. Excellent quality images were obtained, and a series of three are shown in Fig. 132.153 from 6, 12, and 18 ns. The experimental target shown in the top of Fig. 132.153 consists of a Be tube filled with foam and a 20-μm Ti foil tracer on one side. The target is driven from both ends (with a slight delay to the beam opposed to the foil). At 6 ns the foil is just beginning to be driven into the foam; at 12 ns the foil has propagated into the foam and is just meeting the oncoming shock; and at 18 ns it has been recompressed and stalled by the counter-propagating shock passing through it. The Be tube and shocks are visible in the radiographs as faint outlines perturbed by the propagating shock at the walls and in the foam. At 18 ns the tube is almost completely unrecognizable. The information from the turbulent mixing of the Ti layer in the reshocked area is contained in the width of the Ti layer. This width can be compared to our BHR-2 mix model in hydrodynamic simulations to understand how turbulence can affect the mixing of materials at material boundaries.

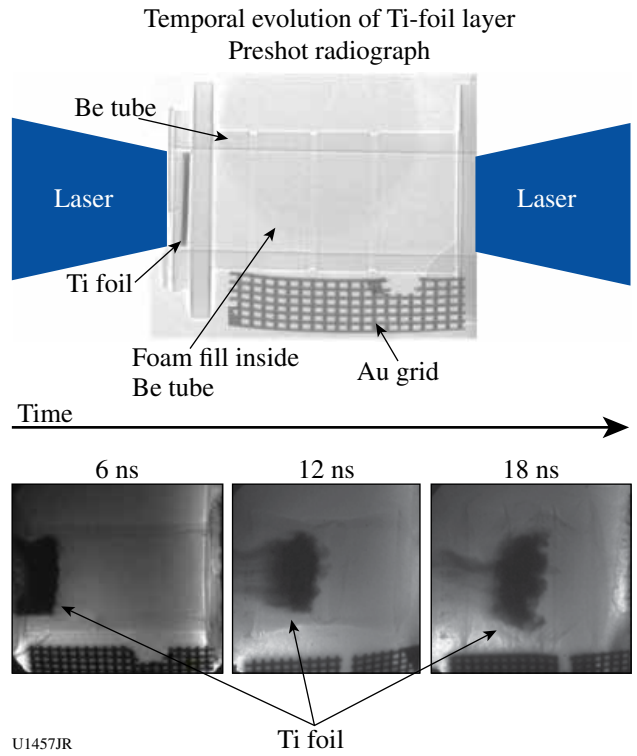


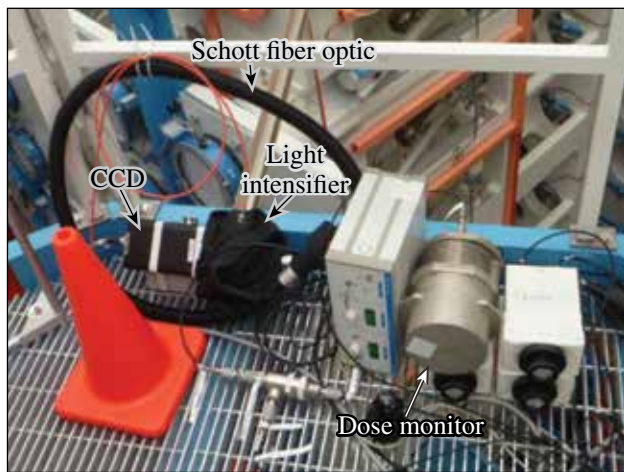
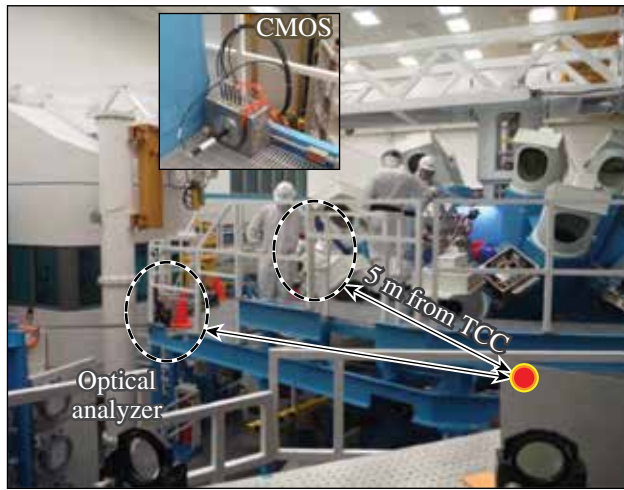
Figure 132.153  
The temporal evolution of a 20-μm Ti tracer foil inside a Be shock tube filled with foam. The laser pushes a shock into the tube from both ends, with a resultant recompression and stall of the shocked layer.

**FY12 CEA Experiments at the Omega Laser Facility**

**CEA Vulnerability Diagnostics on OMEGA**

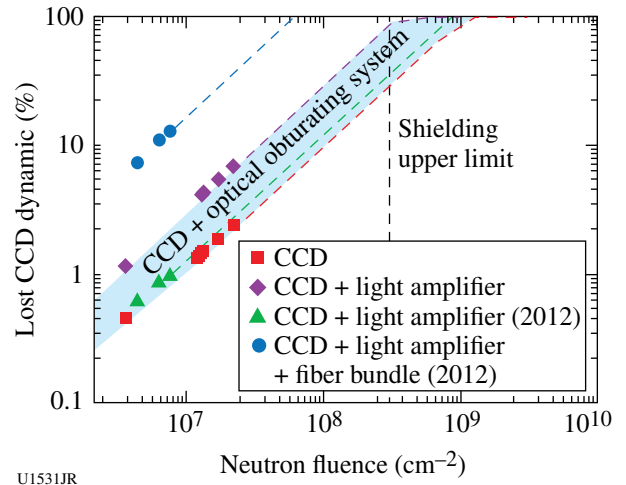
Vulnerability is a key point for plasma diagnostic design in megajoule-class lasers: hardened diagnostics must preserve their nominal performances for neutron yields up at least to 10<sup>17</sup>. Since the DT shots at the Omega Laser Facility reproduce the perturbing source expected during the first 100 ns on megajoule-class laser facilities like Laser Mégajoule (LMJ) or the National Ignition Facility (NIF), this facility can be used to study the survivability of diagnostic elements such as optical relays or optical analyzers.

A standard imaging system, consisting of a fiber bundle, a light amplifier, and a cooled charge-coupled-device (CCD) camera, has been exposed to high neutron yield shots 5 m from target chamber center (TCC) (see Fig. 132.154). The level of nuclear background generated at the Omega Laser Facility leads to visible effects on the recording device that can be quantified thanks to masks positioned between the various optical interfaces. As a result (Fig. 132.155), the increasing background level of the recording device has been clearly



U1530JR

Figure 132.154  
Experimental setup.

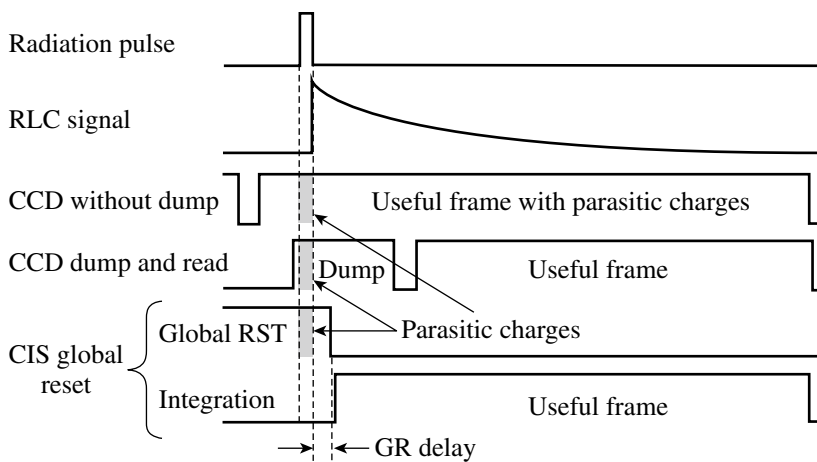


U1531JR

Figure 132.155  
Parasitic signal intensity converted into the CCD dynamic range reduction.

observed: the dynamic range reduction appears to be directly proportional to the neutron fluence. The extreme sensitivity of the fiber bundle has been checked and extrapolation to NIF or LMJ radiative constraints leads us to expect a complete failure of the diagnostic. As a conclusion, such an optical relay must be avoided in a hardened diagnostic architecture.

A new mitigation technique to improve the radiation tolerance of a CMOS image sensor used in plasma diagnostics has been tested. It consists of resetting the charges generated by the incoming particles and then shortly after start to record a second image of a decaying scintillator, free of neutron impacted pixels. Such a scheme, based on the use of a custom global reset (GR) functionality designed by the Institut Supérieur de l'Aéronautique et de l'Espace (ISAE), University of Toulouse is illustrated in the timing diagrams in Fig. 132.156.



U1532JR

Figure 132.156  
Timing diagrams illustrating the standard CCD readout operation, the dump and read technique, and the proposed CIS global reset technique.

A dedicated radiation-hardened test bench has been developed to simulate a plasma diagnostic and has been exposed to neutron yields produced by OMEGA DT shots.<sup>101</sup> The useful signal is generated by a pulsed UV light-emitting diode (LED) synchronized with bang time to excite a long decay-time scintillator. A test pattern has been placed after the radiation-to-light convertor (RLC) to validate that the sensor properly acquires the useful signal. As a first result, the GR reset mode significantly reduces the transient perturbation (parasitic white pixels) without degradation of the image quality (Fig. 132.157). Nevertheless, there is still a small number of remaining disturbed pixels in the image taken with the GR mode. Monte Carlo simulations show that some delayed high-energy particles impinge the sensor after the GR dump phase and create these perturbations during the image acquisition.

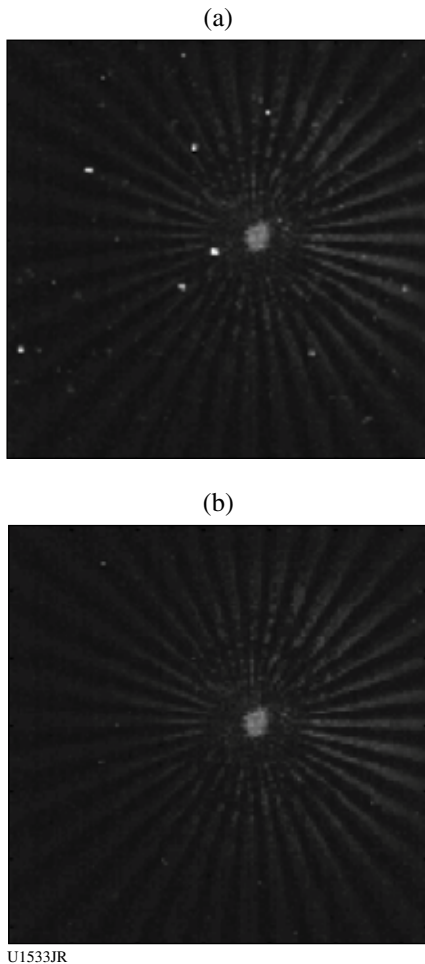


Figure 132.157  
RLC and test pattern image captured during a laser shot. (a) Image acquired with the standard timing diagram (no GR) and (b) image acquired with the GR fast dump phase.

### High-Resolution Imaging at LLE for CEA Shots

An extended high-resolution x-ray imager (EHRXI) was successfully implemented on OMEGA in May 2012 for the CEA “preheat” campaign. This diagnostic consists of an x-ray microscope and a charge-injection-device (CID) camera. The microscope is a two toroidal mirror pseudo-Wolter microscope. EHRXI is the extended version of an already existing diagnostic, the high-resolution x-ray imager (HRXI). We have replaced its mirrors with similar ones yet coated with a non-periodic multilayer coating that extends their reflectivity up to 12 keV at a grazing angle of  $0.6^\circ$ . The overall layout of the EHRXI is shown in Fig. 132.158.

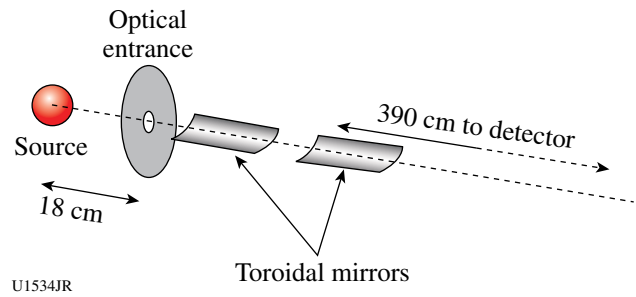
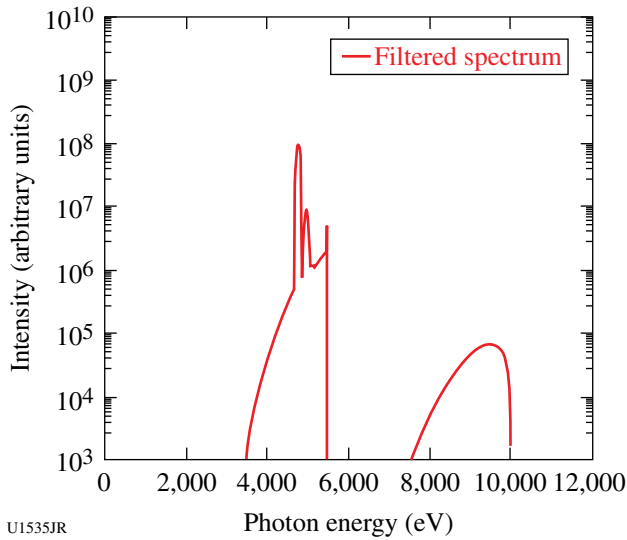


Figure 132.158  
Schematic showing the layout of the EHRXI diagnostic.

The design of the microscope allows it to obtain a resolution of  $4 \mu\text{m}$  in a 1-mm-diam field of view. This resolution was measured on a low-energy Riber x-ray generator at CEA.<sup>102</sup>

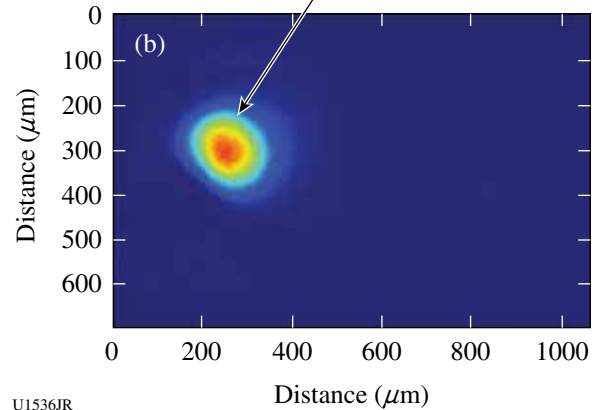
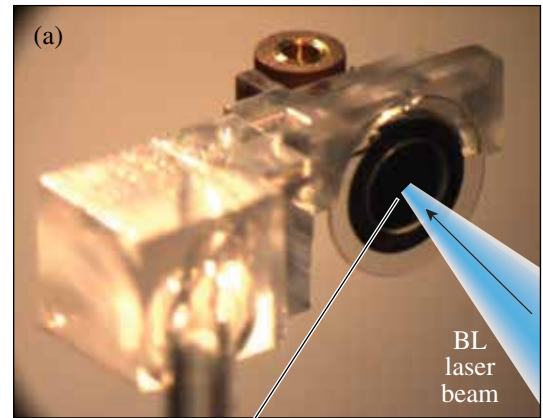
The goal of the experiment led at LLE was to observe the preheating of a metallic sample on a cavity laser entrance hole (LEH) using radiography while the cavity is being shot. The purpose of the EHRXI was to get a precise image of the Ti backlighting x-ray source. The EHRXI was aimed at the center of the backlighting source, with an angle of  $56^\circ$  regarding the back normal vector of that source. It was placed 30 cm from the backlighter. The microscope entrance was filtered with  $75 \mu\text{m}$  of vanadium to get the spectrum presented Fig. 132.159. The CID camera was placed in a dedicated holder at the back of a ten-inch manipulator (TIM-1) as shown Fig. 132.160.

The target used for the experiment is presented in Fig. 132.161(a). The radiography target is the black disk in the foreground. Figure 132.161(b) shows an image of a shot recorded by the EHRXI. The expected x-ray source size was  $200 \times 300 \mu\text{m}$  and the measured size is  $230 \times 300 \mu\text{m}$ . The results are, therefore, in good agreement with the expectations.



U1535JR

Figure 132.159  
Emission spectrum filtered with 75  $\mu\text{m}$  of vanadium.



U1536JR

Figure 132.161  
(a) Target photo taken on the EHRXI line-of-sight. (b) An EHRXI image of the backlighting source of the preheat campaign.



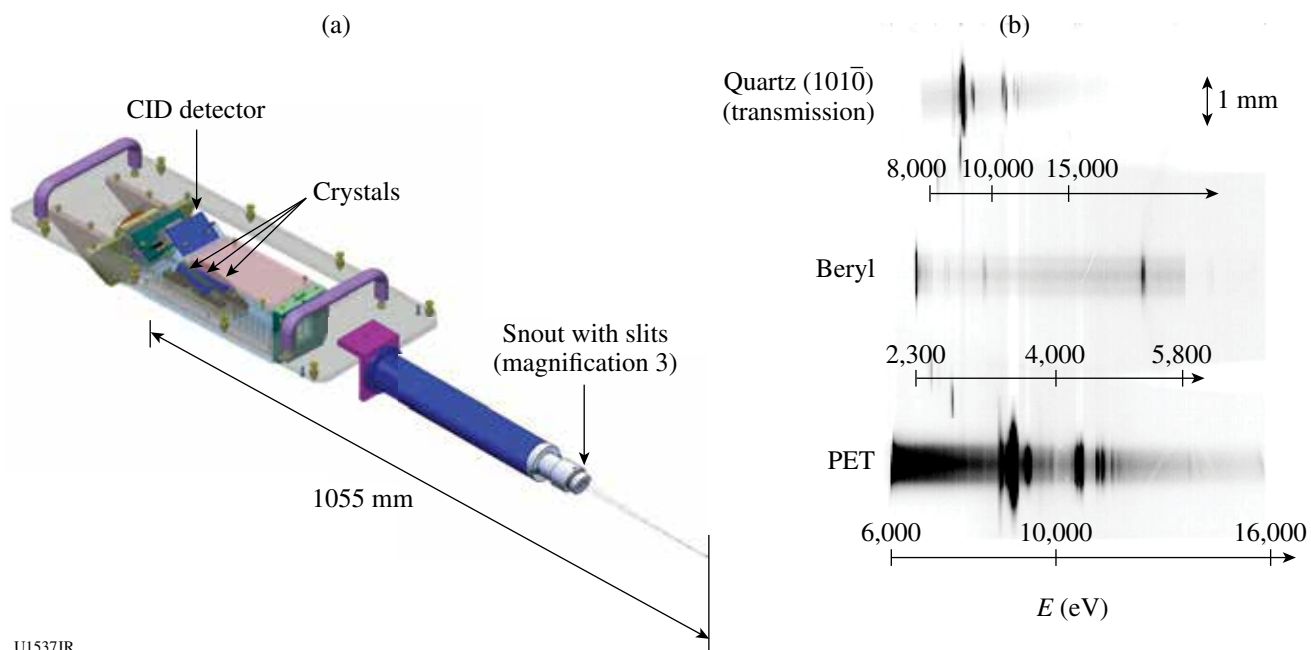
U1535aJR

Figure 132.160  
Photo of the EHRXI in TIM-1; the CID camera holder sits at the back of the TIM.

The image is post-treated to remove the charge injection device (CID) noise and the anamorphosis caused by the angle of the line of sight. In conclusion, the EHRXI implementation on OMEGA was a success and it proved to be a versatile, easy-to-use diagnostic.

### *X-Ray Crystal Spectrometers (XCCS)*

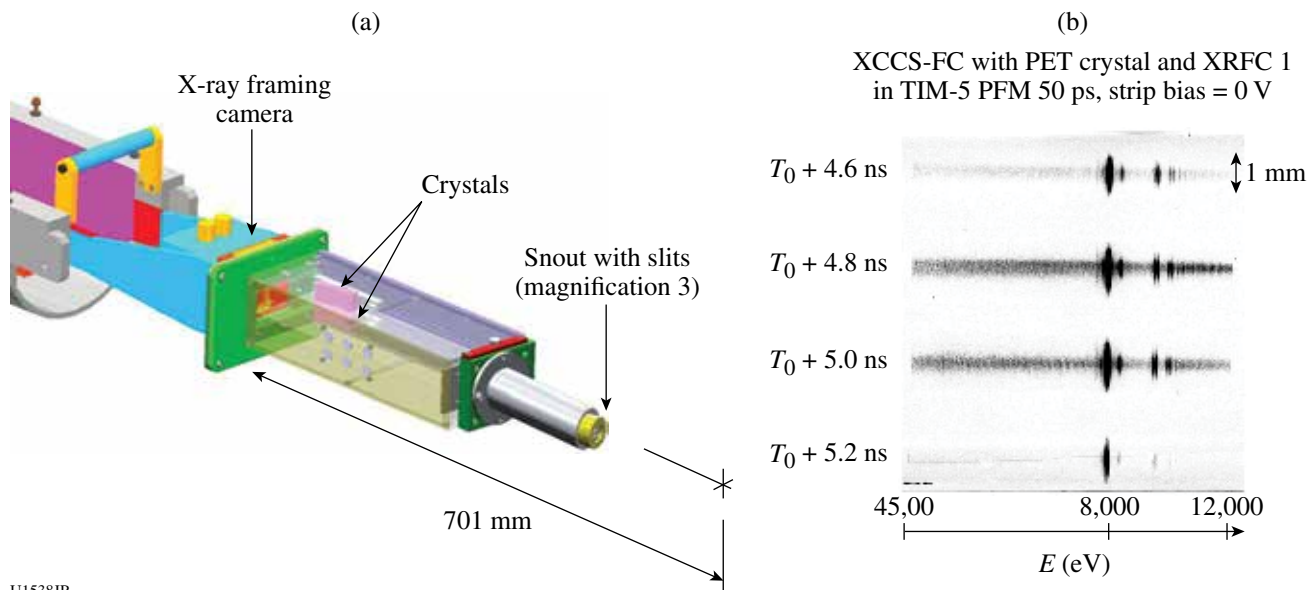
Two x-ray crystal spectrometers in the TIM have been built by CEA. The first one is the XCCS-CID (Fig. 132.162). It is time integrated. It features three channels with an imaging slit (magnification 3), a blast shield, filters, a cylindrical crystal, and detection is performed by a CID detector. The distance of the CID to target chamber center (TCC) is 1055 mm. The second one is XCCS-FC (Fig. 132.163). It features four channels with an imaging slit (magnification 3), filters, a cylindrical crystal, and detection is performed by a framing camera (FC). Two adjacent channels share the same 20-mm-width crystal. The distance of the framing camera to TCC is 701 mm. Both spectrometers can accommodate crystals on spacers and shims with a fixed angle ranging from 7.5° to 35° inside a large box.



U1537JR

Figure 132.162

(a) Schematic of the XCCS-CID; (b) Zn spectrum recorded on shot 62653.



U1538JR

Figure 132.163

(a) Schematic of the XCCS-FC; (b) Ni spectrum obtained on shot 67454.

With the available crystals, configurations covering 1.5 to 15 keV can be achieved.

**CEA Rugby Implosions and Convergent Ablation Experiments on OMEGA**

CEA is pursuing indirect-drive-implosion experiments on OMEGA using rugby-shaped hohlraums in preparation for early implosion on the Laser Mégajoule (LMJ). It has been previously demonstrated that an increased x-ray drive (+18% in flux) was achieved with a vacuum rugby-shaped hohlraum in comparison with a cylinder.<sup>103</sup> These results were confirmed and even enhanced in the case of gas-filled hohlraums. The question of the precise wall shape of the rugby hohlraum has been addressed recently<sup>104</sup> and it was demonstrated that elliptically shaped hohlraums [see Fig. 132.164(a)] are more efficient than spherically shaped hohlraums. There is less wall hydrodynamic motion and less absorption for the LMJ inner cone, providing a

better control of time-dependent symmetry swings. The goal of one experiment was, therefore, to characterize energetics and capsule implosion in elliptical hohlraums compared to rugby- and cylinder-shaped hohlraums during last year's shots.

The round core image acquired on an implosion performed in a gas-filled elliptical hohlraum confirms our capability to control the symmetry in this new hohlraum geometry [see Fig. 132.164(b)].

The increased x-ray drive in rugby measured with Dante was confirmed by enhanced nuclear performances and more ablated mass.<sup>103</sup> It is nevertheless important to perform convergent ablation measurements<sup>105</sup> to assess the implosion velocity—a key metric for ignition performance. ConA experiments with gas-filled rugby hohlraums were, therefore, shot for the first time. The schematic of the experimental configuration is shown in Fig. 132.165(a). A time-resolved 1-D streaked radiography is

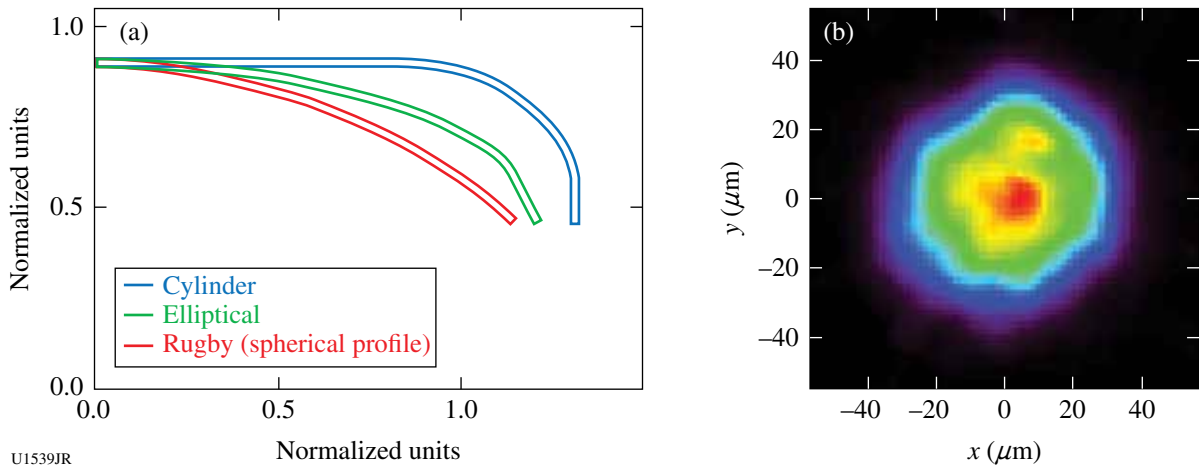


Figure 132.164 (a) Shaped-hohlraum profiles and (b) an x-ray core image for a D<sub>2</sub> implosion performed in an elliptically shaped hohlraum.

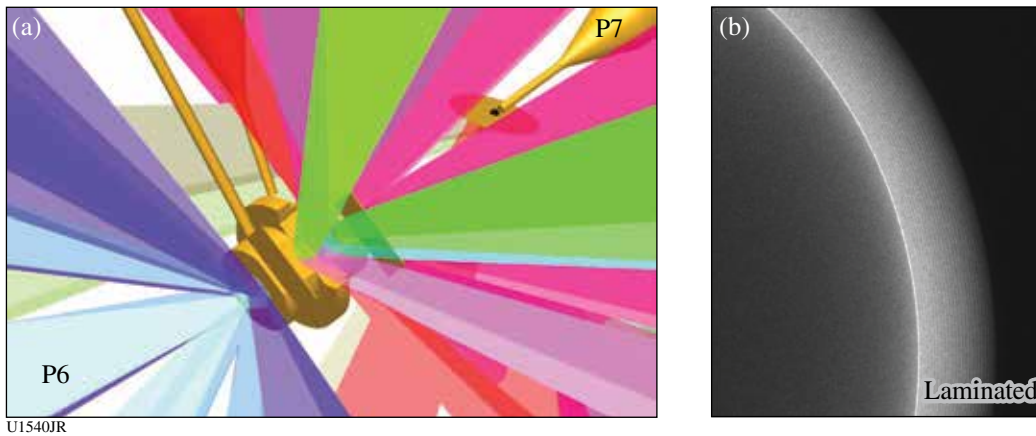
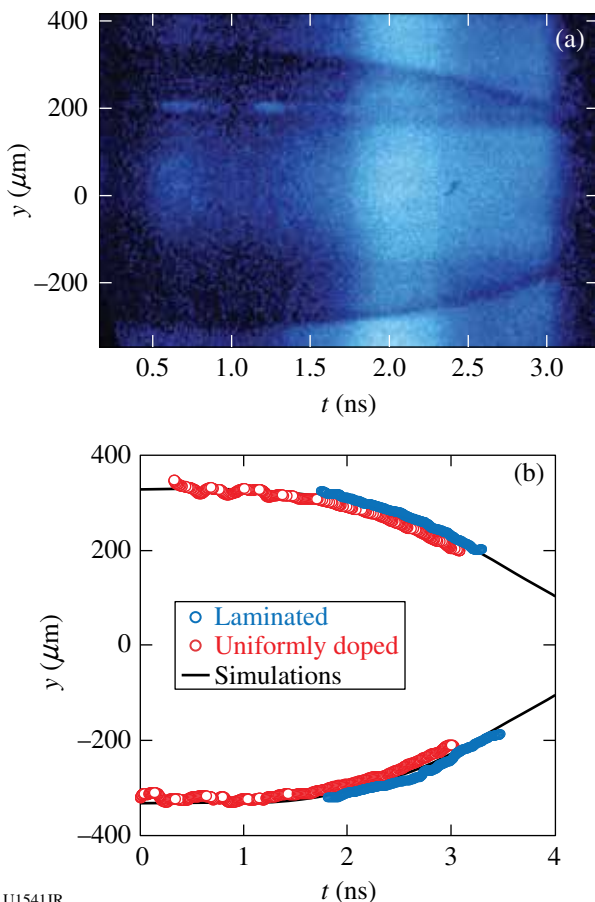


Figure 132.165 (a) Experimental configuration along P6/P7. The streaked implosion radiography is performed toward H14, perpendicular to the hohlraum axis. (b) A typical laminated capsule.

acquired with SSC A in the direction perpendicular to the hohlraum axis, whereas a 2-D time-resolved radiography is acquired at the same time along the hohlraum axis on an x-ray framing camera. These experiments were also aimed at comparing the implosion performance of a uniformly doped and laminated ablator.<sup>106</sup> A laminated ablator consists of thin alternate layers of undoped and germanium-doped CH. Figure 132.165(b) presents a pre-shot radiography of a laminated capsule, on which the thin layers of doped and undoped material are clearly visible. It has been experimentally demonstrated in planar geometry that laminated ablators could mitigate Rayleigh–Taylor growth at the ablation front.<sup>107</sup>

A typical backlight implosion is shown on Fig. 132.166(a). The limb of the shell is well defined and its position could be extracted from the radiography. Preliminary data comparing uniformly doped and laminated capsule trajectory do not indicate discrepancies for the implosion. This corroborates the trajectory measurements already acquired for planar samples.<sup>107</sup>



U1541JR  
 Figure 132.166  
 (a) Typical streaked radiography acquired on a gas-filled rugby implosion.  
 (b) Comparison of capsule trajectory for laminated and uniformly doped ablators.

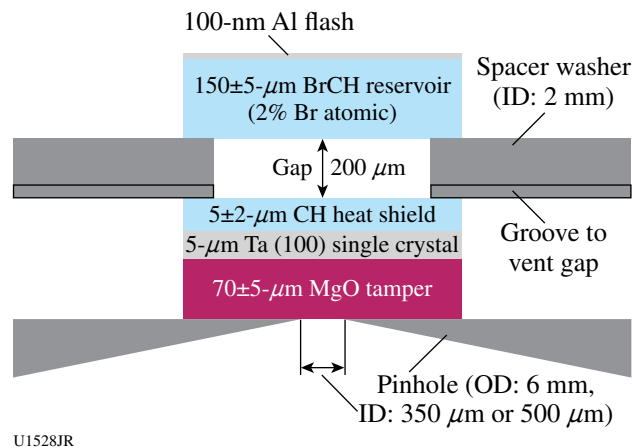
## FY12 AWE OMEGA EP and OMEGA Experimental Programs

### ShkLaue-12A

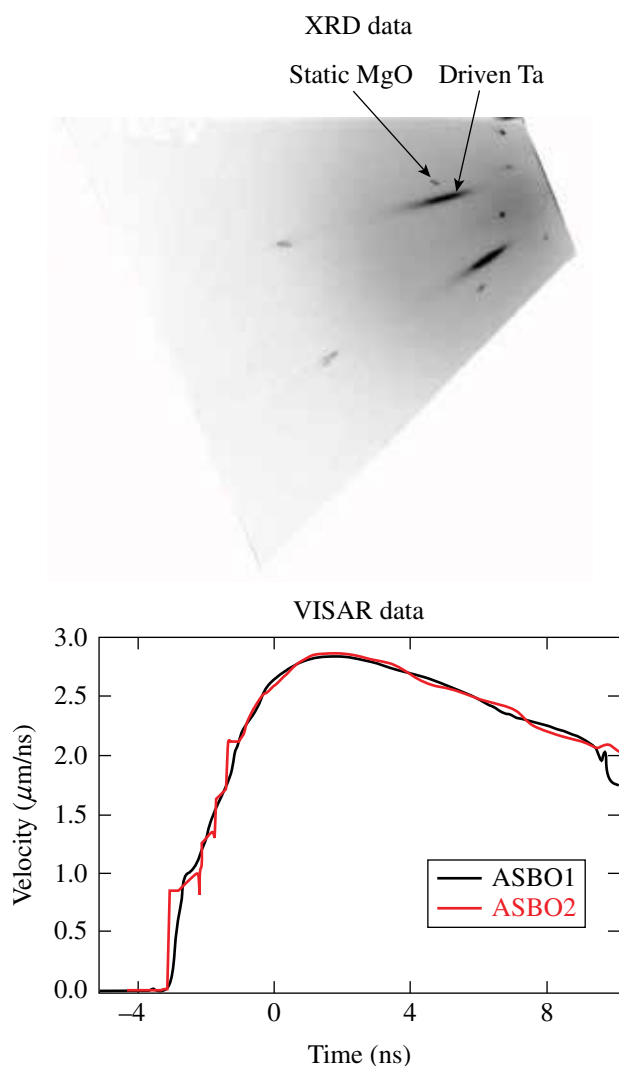
Principal Investigator: A. J. Comley (AWE)

In the ShkLaue-12A campaign, we made a first attempt to diagnose ramp-compressed, single-crystal tantalum [100] using our established broadband x-ray (“white light”) Laue diffraction platform. This platform utilizes an implosion capsule backlighter (980- $\mu\text{m}$  outer diameter, with a 10- $\mu\text{m}$ -thick CH wall) driven by 30 beams [each beam contained 500 J in a 1-ns square pulse and SG4 distributed phase plate (DPP)] to generate a smoothly varying and broadband spectrum of x rays from a “point” source. VISAR (velocity interferometer system for any reflector) is also employed simultaneously with the x-ray diffraction technique.

The target design is shown in Fig. 132.167. Three beams were employed (each  $\sim 200$  J in a 3.7-ns square pulse and SG8 DPP) to produce a shock in the BrCH reservoir. Upon shock breakout, the reservoir material crosses the gap and stagnates near the sample (which is protected from direct heating by a CH heat shield), such that a smoothly increasing ramp-compression drive is produced, with a peak pressure of  $\sim 100$  GPa. X-ray diffraction and VISAR data were obtained successfully (Fig. 132.168). Analysis of the diffraction patterns, in which we see a clear signature from the driven tantalum sample, is currently undergoing detailed analysis in conjunction with information obtained from VISAR.



U1528JR  
 Figure 132.167  
 ShkLaue-12A ramp-compression target design.



U1529JR

Figure 132.168

(a) The x-ray diffraction (XRD) pattern contains characteristic spots, each of which can be attributed to either the tantalum or MgO layers in the target package and to specific crystallographic lattice planes. (b) VISAR records the compression history of the sample.

## REFERENCES

1. T. S. Duffy, R. J. Hemley, and H. Mao, *Phys. Rev. Lett.* **74**, 1371 (1995).
2. A. R. Organov, M. J. Gillian, and G. D. Price, *J. Phys. Chem.* **118**, 10,174 (2003).
3. T. Nagayama, R. C. Mancini, R. Florido, R. Tommasini, J. A. Koch, J. A. Delettrez, S. P. Regan, and V. A. Smalyuk, *J. Appl. Phys.* **109**, 093303 (2011).
4. T. Nagayama, R. C. Mancini, R. Florido, D. Mayes, R. Tommasini, J. A. Koch, J. A. Delettrez, S. P. Regan, and V. A. Smalyuk, *Phys. Plasmas* **19**, 082705 (2012).
5. D. T. Casey, J. A. Frenje, M. Gatu Johnson, M. J.-E. Manuel, N. Sinenian, A. B. Zylstra, F. H. Séguin, C. K. Li, R. D. Petrasso, V. Yu. Glebov, P. B. Radha, D. D. Meyerhofer, T. C. Sangster, D. P. McNabb, P. A. Amendt, R. N. Boyd, S. P. Hatchett, S. Quaglioni, J. R. Rygg, I. J. Thompson, A. D. Bacher, H. W. Herrmann, and Y. H. Kim, *Phys. Rev. Lett.* **109**, 025003 (2012).
6. N. Sinenian, G. Fiksel, J. A. Frenje, C. G. Freeman, M. J.-E. Manuel, D. T. Casey, P. M. Nilson, C. Stoeckl, W. Theobald, D. D. Meyerhofer, and R. D. Petrasso, *Phys. Plasmas* **19**, 093118 (2012).
7. M. J.-E. Manuel, C. K. Li, F. H. Séguin, J. A. Frenje, D. T. Casey, R. D. Petrasso, S. X. Hu, R. Betti, J. D. Hager, D. D. Meyerhofer, and V. Smalyuk, *Phys. Plasmas* **19**, 082710 (2012).
8. N. Sinenian, A. B. Zylstra, M. J. E. Manuel, H. G. Rinderknecht, J. A. Frenje, F. H. Seguin, C. K. Li, R. D. Petrasso, V. Goncharov, J. Delettrez, I. V. Igumenshchev, D. H. Froula, C. Stoeckl, T. C. Sangster, D. D. Meyerhofer, J. A. Cobble, and D. G. Hicks, *Appl. Phys. Lett.* **101**, 114102 (2012).
9. M. J.-E. Manuel *et al.*, *Appl. Phys. Lett.* **100**, 203505 (2012).
10. M. J.-E. Manuel, C. K. Li, F. H. Séguin, J. Frenje, D. T. Casey, R. D. Petrasso, S. X. Hu, R. Betti, J. D. Hager, D. D. Meyerhofer, and V. A. Smalyuk, *Phys. Rev. Lett.* **108**, 255006 (2012).
11. D. T. Casey, J. A. Frenje, M. Gatu Johnson, M. J.-E. Manuel, H. G. Rinderknecht, N. Sinenian, F. H. Séguin, C. K. Li, R. D. Petrasso, P. B. Radha, J. A. Delettrez, V. Yu. Glebov, D. D. Meyerhofer, T. C. Sangster, D. P. McNabb, P. A. Amendt, R. N. Boyd, J. R. Rygg, H. W. Herrmann, Y. H. Kim, and A. D. Bacher, *Phys. Rev. Lett.* **108**, 075002 (2012).
12. C. K. Li, F. H. Séguin, J. A. Frenje, M. J. Rosenberg, H. G. Rinderknecht, A. B. Zylstra, R. D. Petrasso, P. A. Amendt, O. L. Landen, A. J. Mackinnon, R. P. J. Town, S. C. Wilks, R. Betti, D. D. Meyerhofer, J. M. Soares, J. Hund, J. D. Kilkenny, and A. Nikroo, *Phys. Rev. Lett.* **108**, 025001 (2012).
13. F. H. Séguin, C. K. Li, M. J.-E. Manuel, H. G. Rinderknecht, N. Sinenian, J. A. Frenje, J. R. Rygg, D. G. Hicks, R. D. Petrasso, J. Delettrez, R. Betti, F. J. Marshall, and V. A. Smalyuk, *Phys. Plasmas* **19**, 012701 (2012).
14. N. Sinenian *et al.*, "A Multithreaded Modular Software Toolkit for Control of Complex Experiments," to be published in *Computing in Science and Engineering*.
15. D. T. Casey, J. A. Frenje, M. Gatu Johnson, F. H. Séguin, C. K. Li, R. D. Petrasso, V. Yu. Glebov, J. Katz, J. P. Knauer, D. D. Meyerhofer, T. C. Sangster, R. M. Bionta, D. L. Bleuel, T. Döppner, S. Glenzer, E. Hartouni, S. P. Hatchett, S. Le Pape, T. Ma, A. MacKinnon, M. A. Mckernan, M. Moran, E. Moses, H.-S. Park, J. Ralph, B. A. Remington, V. Smalyuk, C. B. Yeamans, J. Kline, G. Kyrala, G. A. Chandler, R. J. Leeper, C. L. Ruiz, G. W. Cooper, A. J. Nelson, K. Fletcher, J. Kilkenny, M. Farrell, D. Jasion, and R. Paguio, *Rev. Sci. Instrum.* **83**, 10D912 (2010).
16. F. H. Séguin, N. Sinenian, M. Rosenberg, A. Zylstra, M. J. E. Manuel, H. Sio, C. Waugh, H. G. Rinderknecht, M. Gatu Johnson, J. Frenje, C. K. Li, R. Petrasso, T. C. Sangster, and S. Roberts, *Rev. Sci. Instrum.* **83**, 10D908 (2012).
17. M. J.-E. Manuel *et al.*, *Rev. Sci. Instrum.* **83**, 063506 (2012).

18. N. Sinenian *et al.*, *Rev. Sci. Instrum.* **83**, 043502 (2012).
19. A. Zylstra, C. K. Li, H. G. Rinderknecht, F. H. Séguin, R. D. Petrasso, C. Stoeckl, D. D. Meyerhofer, P. Nilson, T. C. Sangster, S. Le Pape, A. Mackinnon, and P. Patel, *Rev. Sci. Instrum.* **83**, 013511 (2012).
20. A. B. Zylstra *et al.*, *Nucl. Instrum. Methods Phys. Res. A* **681**, 84 (2012).
21. M. Hohenberger, P.-Y. Chang, G. Fiksel, J. P. Knauer, R. Betti, F. J. Marshall, D. D. Meyerhofer, F. H. Séguin, and R. D. Petrasso, *Phys. Plasmas* **19**, 056306 (2012).
22. N. Sinenian *et al.*, *Rev. Sci. Instrum.* **82**, 103303 (2011).
23. T. R. Boehly, D. L. Brown, R. S. Craxton, R. L. Keck, J. P. Knauer, J. H. Kelly, T. J. Kessler, S. A. Kumpan, S. J. Loucks, S. A. Letzring, F. J. Marshall, R. L. McCrory, S. F. B. Morse, W. Seka, J. M. Soures, and C. P. Verdon, *Opt. Commun.* **133**, 495 (1997).
24. L. J. Waxer, D. N. Maywar, J. H. Kelly, T. J. Kessler, B. E. Kruschwitz, S. J. Loucks, R. L. McCrory, D. D. Meyerhofer, S. F. B. Morse, C. Stoeckl, and J. D. Zuegel, *Opt. Photonics News* **16**, 30 (2005).
25. C. K. Li, F. H. Séguin, J. A. Frenje, J. R. Rygg, R. D. Petrasso, R. P. J. Town, P. A. Amendt, S. P. Hatchett, O. L. Landen, A. J. Mackinnon, P. K. Patel, V. Smalyuk, J. P. Knauer, T. C. Sangster, and C. Stoeckl, *Rev. Sci. Instrum.* **77**, 10E725 (2006).
26. N. L. Kugland, D. D. Ryutov, P. Y. Chang, R. P. Drake, G. Fiksel, D. H. Froula, S. H. Glenzer, G. Gregori, M. Grosskopf, M. Koenig, Y. Kuramitsu, C. Kuranz, M. C. Levy, E. Liang, J. Meinecke, F. Miniati, T. Morita, A. Pelka, C. Plechaty, R. Presura, A. Ravasio, B. A. Remington, B. Reville, J. S. Ross, Y. Sakawa, A. Spitkovsky, H. Takabe, and H. S. Park, *Nat. Phys.* **8**, 809 (2012).
27. J. S. Ross, S. H. Glenzer, P. Amendt, R. Berger, L. Divol, N. L. Kugland, O. L. Landen, C. Plechaty, B. Remington, D. Ryutov, W. Rozmus, D. H. Froula, G. Fiksel, C. Sorce, Y. Kuramitsu, T. Morita, Y. Sakawa, H. Takabe, R. P. Drake, M. Grosskopf, C. Kuranz, G. Gregori, J. Meinecke, C. D. Murphy, M. Koenig, A. Pelka, A. Ravasio, T. Vinci, E. Liang, R. Presura, A. Spitkovsky, F. Miniati, and H.-S. Park, *Phys. Plasmas* **19**, 056501 (2012).
28. H.-S. Park, D. D. Ryutov, J. S. Ross, N. L. Kugland, S. H. Glenzer, C. Plechaty, S. M. Pollaine, B. A. Remington, A. Spitkovsky, L. Gargate, G. Gregori, A. Bell, C. Murphy, Y. Sakawa, Y. Kuramitsu, T. Morita, H. Takabe, D. H. Froula, G. Fiksel, F. Miniati, M. Koenig, A. Ravasio, A. Pelka, E. Liang, N. Woolsey, C. C. Kuranz, R. P. Drake, and M. J. Grosskopf, *High Energy Density Phys.* **8**, 38 (2012).
29. A. Spitkovsky, presented at the Colloquium at Northwestern University, Evanston, IL, February 2012.
30. A. Spitkovsky, presented at the 9th International Conference on High Energy Density Laboratory Astrophysics, Tallahassee, FL, 30 April–4 May 2012.
31. A. Spitkovsky, presented at the Twenty-Second International Conference on Numerical Simulations of Plasmas (ICNSP 2011), Long Branch, NJ, 7–9 September 2011.
32. A. Spitkovsky, presented at the Center for Magnetic Self-Organization (CMSO) General Meeting, Durham, NH, 17–20 October 2011.
33. J. Ross, *Bull. Am. Phys. Soc.* **56**, 282 (2011).
34. M. Grosskopf *et al.*, presented at High Energy Density Laboratory Astrophysics, Tallahassee, FL, 30 April–4 May 2012.
35. L. Willingale, P. M. Nilson, A. G. R. Thomas, J. Cobble, R. S. Craxton, A. Maksimchuk, P. A. Norreys, T. C. Sangster, R. H. H. Scott, C. Stoeckl, C. Züllick, and K. Krushelnick, *Phys. Rev. Lett.* **106**, 105002 (2011).
36. S. P. D. Mangles *et al.*, *Phys. Rev. Lett.* **94**, 245001 (2005).
37. N. Naseri, S. G. Bochkarev, and W. Rozmus, *Phys. Plasmas* **17**, 033107 (2010).
38. S. Fritzler *et al.*, *Phys. Rev. Lett.* **89**, 165004 (2002).
39. G. H. Miller and T. J. Ahrens, *Rev. Mod. Phys.* **63**, 919 (1991), Eq. (127).
40. H. Chen, S. C. Wilks, D. D. Meyerhofer, J. Bonlie, C. D. Chen, S. N. Chen, C. Courtois, L. Elbersson, G. Gregori, W. Kruer, O. Landoas, J. Mithen, J. Myatt, C. D. Murphy, P. Nilson, D. Price, M. Schneider, R. Shepherd, C. Stoeckl, M. Tabak, R. Tommasini, and P. Beiersdorfer, *Phys. Rev. Lett.* **105**, 015003 (2010).
41. H. Chen, D. D. Meyerhofer, S. C. Wilks, R. Cauble, F. Dollar, K. Falk, G. Gregori, A. Hazi, E. I. Moses, C. D. Murphy, J. Myatt, J. Park, J. Seely, R. Shepherd, A. Spitkovsky, C. Stoeckl, C. I. Szabo, R. Tommasini, C. Züllick, and P. Beiersdorfer, *High Energy Density Phys.* **7**, 225 (2011).
42. O. A. Hurricane, *High Energy Density Phys.* **4**, 97 (2008).
43. E. C. Harding *et al.*, *Phys. Rev. Lett.* **103**, 045005 (2009).
44. O. A. Hurricane *et al.*, *Phys. Plasmas* **16**, 056305 (2009).
45. V. A. Smalyuk *et al.*, *Phys. Plasmas* **19**, 092702 (2012).
46. K. S. Raman *et al.*, *Phys. Plasmas* **19**, 092112 (2012).
47. O. A. Hurricane *et al.*, *Phys. Rev. Lett.* **109**, 155004 (2012).
48. Z. Y. Bao *et al.*, *At. Data Nucl. Data Tables* **76**, 70 (2000).
49. N. Cue, J.-C. Poizat, and J. Remillieux, *Europhys. Lett.* **8**, 19 (1989).
50. A. Pálffy *et al.*, *Phys. Lett. B* **661**, 330 (2008).
51. A. Pálffy, W. Scheid, and Z. Harman, *Phys. Rev. A* **73**, 012715 (2006).
52. M. R. Harston and J. F. Chemin, *Phys. Rev. C* **59**, 2462 (1999).
53. M. Morita and K. Otozai, *Hyperfine Interact.* **2**, 418 (1976).
54. S. Kishimoto *et al.*, *Nucl. Phys. A* **748**, 3 (2005).
55. M. R. Harston and J. J. Carroll, *Laser Phys.* **14**, 1452 (2004).
56. N. L. Kugland, presented at the 9th International Conference on High Energy Density Laboratory Astrophysics, Tallahassee, FL, 30 April–4 May 2012.

57. H.-S. Park, N. L. Kugland, J. S. Ross, B. A. Remington, C. Plechaty, D. D. Ryutov, A. Spitkovsky, G. Gregori, A. Bell, J. Meinecke, C. Murphy, Y. Sakawa, Y. Kuramitsu, H. Takabe, D. H. Froula, G. Fiksel, F. Miniati, M. Koenig, A. Ravasio, E. Liang, N. Woolsey, R. P. Drake, C. Kuranz, M. Grosskopf, and R. Presura, presented at the 9th International Conference on High Energy Density Laboratory Astrophysics, Tallahassee, FL, 30 April–4 May 2012.
58. D. D. Ryutov *et al.*, presented at the 9th International Conference on High Energy Density Laboratory Astrophysics, Tallahassee, FL, 30 April–4 May 2012.
59. J. S. Ross *et al.*, *Rev. Sci. Instrum.* **83**, 10E323 (2012).
60. N. L. Kugland *et al.*, *Rev. Sci. Instrum.* **83**, 101301 (2012).
61. D. D. Ryutov *et al.*, *Plasma Phys. Control. Fusion* **54**, 105021 (2012).
62. D. D. Ryutov *et al.*, *Phys. Plasmas* **19**, 074501 (2012).
63. D. D. Ryutov *et al.*, *Phys. Plasmas* **18**, 104504 (2011).
64. N. L. Kugland *et al.*, “Visualizing Electromagnetic Fields in Laser-Produced Counter-Streaming Plasma Experiments for Collisionless Shock Laboratory Astrophysics,” to be submitted to *Physics of Plasmas*.
65. M. J. Grosskopf, R. P. Drake, C. C. Kuranz, E. M. Rutter, J. S. Ross, N. L. Kugland, S. Pollaine, B. A. Remington, D. D. Ryutov, A. Spitkovsky, L. Gargate, G. Gregori, A. Bell, C. D. Murphy, J. Meinecke, B. Reville, Y. Sakawa, Y. Kuramitsu, H. Takabe, D. H. Froula, G. Fiksel, F. Miniati, M. Koenig, A. Ravasio, E. Liang, N. Woolsey, and H.-S. Park, “Simulation of Laser-Driven, Ablated Flows in Collisionless Shock Experiments on OMEGA and the NIF,” submitted to *High Energy Density Physics*.
66. S. P. Regan, K. Falk, G. Gregori, P. B. Radha, S. X. Hu, T. R. Boehly, B. J. B. Crowley, S. H. Glenzer, O. L. Landen, D. O. Gericke, T. Doeppner, D. D. Meyerhofer, C. D. Murphy, T. C. Sangster, and J. Vorberger, “Inelastic X-Ray Scattering from Shocked Liquid Deuterium,” to be published in *Physical Review Letters*; *LLE Review Quarterly Report* **131**, 143, Laboratory for Laser Energetics, University of Rochester, Rochester, NY, LLE Document No. DOE/NA/28302-1064 (2012); *LLE Review Quarterly Report* **130**, 72, Laboratory for Laser Energetics, University of Rochester, Rochester, NY, LLE Document No. DOE/NA/28302-1058 (2012).
67. G. Gregori *et al.*, *High Energy Density Phys.* **3**, 99 (2007).
68. E. García Saiz *et al.*, *Nat. Phys.* **4**, 940 (2008).
69. G. Kresse and J. Furthmüller, *Phys. Rev. B* **54**, 11169 (1996).
70. J. Vorberger *et al.*, *Phys. Rev. B* **75**, 024206 (2007).
71. W. Theobald, A. A. Solodov, C. Stoeckl, K. S. Anderson, R. Betti, T. R. Boehly, R. S. Craxton, J. A. Delettrez, C. Dorrer, J. A. Frenje, V. Yu. Glebov, H. Habara, K. A. Tanaka, J. P. Knauer, R. Lauck, F. J. Marshall, K. L. Marshall, D. D. Meyerhofer, P. M. Nilson, P. K. Patel, H. Chen, T. C. Sangster, W. Seka, N. Sinenian, T. Ma, F. N. Beg, E. Giraldez, and R. B. Stephens, *Phys. Plasmas* **18**, 056305 (2011).
72. P. B. Radha, T. J. B. Collins, J. A. Delettrez, Y. Elbaz, R. Epstein, V. Yu. Glebov, V. N. Goncharov, R. L. Keck, J. P. Knauer, J. A. Marozas, F. J. Marshall, R. L. McCrory, P. W. McKenty, D. D. Meyerhofer, S. P. Regan, T. C. Sangster, W. Seka, D. Shvarts, S. Skupsky, Y. Srebro, and C. Stoeckl, *Phys. Plasmas* **12**, 056307 (2005).
73. J. A. King, K. Akli, B. Zhang, R. R. Freeman, M. H. Key, C. D. Chen, S. P. Hatchett, J. A. Koch, A. J. MacKinnon, P. K. Patel, R. Snively, R. P. J. Town, M. Borghesi, L. Romagnani, M. Zepf, T. Cowan, H. Habara, R. Kodama, Y. Toyama, S. Karsch, K. Lancaster, C. Murphy, P. Norreys, R. Stephens, and C. Stoeckl, *Appl. Phys. Lett.* **86**, 191501 (2005).
74. C. Stoeckl, J. A. Delettrez, R. Epstein, G. Fiksel, D. Guy, M. Hohenberger, R. K. Jungquist, C. Mileham, P. M. Nilson, T. C. Sangster, M. J. Shoup III, and W. Theobald, *Rev. Sci. Instrum.* **83**, 10E501 (2012).
75. H.-S. Park *et al.*, *Phys. Rev. Lett.* **104**, 135504 (2010).
76. J. F. Barnes *et al.*, *J. Appl. Phys.* **45**, 727 (1974).
77. H.-S. Park *et al.*, *Phys. Plasmas* **17**, 056314 (2010).
78. H.-S. Park *et al.*, *AIP Conf. Proc.* **1426**, 1371 (2012).
79. N. R. Barton *et al.*, *J. Appl. Phys.* **109**, 073501 (2011).
80. B. Remington *et al.*, *AIP Conf. Proc.* **1426**, 1375 (2012).
81. J. L. Belof *et al.*, *AIP Conf. Proc.* **1426**, 1521 (2012).
82. J. Edwards *et al.*, *Phys. Rev. Lett.* **92**, 075002 (2004).
83. H.-S. Park, D. M. Chambers, H.-K. Chung, R. J. Clarke, R. Eagleton, E. Giraldez, T. Goldsack, R. Heathcote, N. Izumi, M. H. Key, J. A. King, J. A. Koch, O. L. Landen, A. Nikroo, P. K. Patel, D. F. Price, B. A. Remington, H. F. Robey, R. A. Snively, D. A. Steinman, R. B. Stephens, C. Stoeckl, M. Storm, M. Tabak, W. Theobald, R. P. J. Town, J. E. Wickersham, and B. B. Zhang, *Phys. Plasmas* **13**, 056309 (2006).
84. L. Burakovsky *et al.*, *Phys. Rev. Lett.* **104**, 255702 (2010).
85. A. Dewaele, P. Loubeyre, and M. Mezouar, *Phys. Rev. B* **70**, 094112 (2004).
86. D. G. Hicks, T. R. Boehly, P. M. Celliers, J. H. Eggert, S. J. Moon, D. D. Meyerhofer, and G. W. Collins, *Phys. Rev. B* **79**, 014112 (2009); M. D. Knudson *et al.*, *Phys. Rev. B* **69**, 144209 (2004).
87. S. Root *et al.*, *Phys. Rev. Lett.* **105**, 085501 (2010).
88. C. E. Ragan III *et al.*, Los Alamos National Laboratory, Los Alamos, NM, LA-UR-83-2081 (1983).
89. Y. Ping, D. G. Hicks, B. Yaakobi, F. Coppari, D. E. Fratanduono, S. Hamel, J. H. Eggert, J. R. Rygg, R. F. Smith, T. R. Boehly, and G. W. Collins, “EXAFS Study of Iron Ramp-Compressed up to 560 GPa,” submitted to *Physical Review Letters*.
90. A. Salamat *et al.*, *Phys. Rev. B* **84**, 140104 (2011).
91. R. Briggs *et al.*, *J. Phys.: Conf. Ser.* **377**, 012035 (2012).
92. B. Schwager *et al.*, *J. Chem. Phys.* **133**, 084501 (2010); S. T. Weir *et al.*, *J. Appl. Phys.* **111**, 123529 (2012).
93. S. Desgreniers, Y. K. Vohra, and A. L. Ruoff, *Phys. Rev. B* **39**, 10359 (1989).

94. F. Pérez *et al.*, Phys. Plasmas **19**, 083101 (2012).
95. K. B. Fournier *et al.*, Phys. Rev. Lett. **92**, 165005 (2004).
96. C. Constantin *et al.*, Phys. Plasmas **12**, 063104 (2005).
97. M. Tanabe *et al.*, High Energy Density Phys. **6**, 89 (2010).
98. J. R. Patterson *et al.*, Rev. Sci. Instrum. **83**, 10D725 (2012).
99. Y. Kim, J. M. Mack, H. W. Herrmann, C. S. Young, G. M. Hale, S. Caldwell, N. M. Hoffman, S. C. Evans, T. J. Sedillo, A. McEvoy, J. Langenbrunner, H. H. Hsu, M. A. Huff, S. Batha, C. J. Horsfield, M. S. Rubery, W. J. Garbett, W. Stoeffl, E. Grafil, L. Bernstein, J. A. Church, D. B. Sayre, M. J. Rosenberg, C. Waugh, H. G. Rinderknecht, M. Gatu Johnson, A. B. Zylstra, J. A. Frenje, D. T. Casey, R. D. Petrasso, E. K. Miller, V. Yu Glebov, C. Stoeckl, and T. C. Sangster, Phys. Plasmas **19**, 056313 (2012).
100. Y. Kim, J. M. Mack, H. W. Herrmann, C. S. Young, G. M. Hale, S. Caldwell, N. M. Hoffman, S. C. Evans, T. J. Sedillo, A. McEvoy, J. Langenbrunner, H. H. Hsu, M. A. Huff, S. Batha, C. J. Horsfield, M. S. Rubery, W. J. Garbett, W. Stoeffl, E. Grafil, L. Bernstein, J. A. Church, D. B. Sayre, M. J. Rosenberg, C. Waugh, H. G. Rinderknecht, M. Gatu Johnson, A. B. Zylstra, J. A. Frenje, D. T. Casey, R. D. Petrasso, E. K. Miller, V. Yu Glebov, C. Stoeckl, and T. C. Sangster, Phys. Rev. C **85**, 061601 (2012).
101. V. Goiffon *et al.*, Electron. Lett. **48**, 1338 (2012).
102. D. Dennetiere, P. Audebert, R. Bahr, S. Bole, J. L. Bourgade, B. Brannon, F. Girard, G. Pien, and Ph. Troussel, in *Target Diagnostics Physics and Engineering for Inertial Confinement Fusion*, edited by P. Bell and P. Grim (SPIE, Bellingham, WA, 2012), Vol. 8505, p. 85050G.
103. F. Philippe, A. Casner, T. Caillaud, O. Landoas, M. C. Monteil, S. Liberatore, H. S. Park, P. Amendt, H. Robey, C. Sorce, C. K. Li, F. Seguin, M. Rosenberg, R. Petrasso, V. Glebov, and C. Stoeckl, Phys. Rev. Lett. **104**, 035004 (2010).
104. S. Laffite and P. Loiseau, Phys. Plasmas **17**, 102704 (2010).
105. D. G. Hicks, B. K. Spears, D. G. Braun, R. E. Olson, C. M. Sorce, P. M. Celliers, G. W. Collins, and O. L. Landen, Phys. Plasmas **17**, 102703 (2010).
106. L. Masse, Phys. Rev. Lett. **98**, 245001 (2007).
107. L. Masse *et al.*, Phys. Rev. E **83**, 055401(R) (2011).